

The near-infrared multi-object spectrograph  
for the Subaru Telescope  
and its application to the observations of distant galaxies

Chihiro Tokoku

March 7, 2006

### Abstract

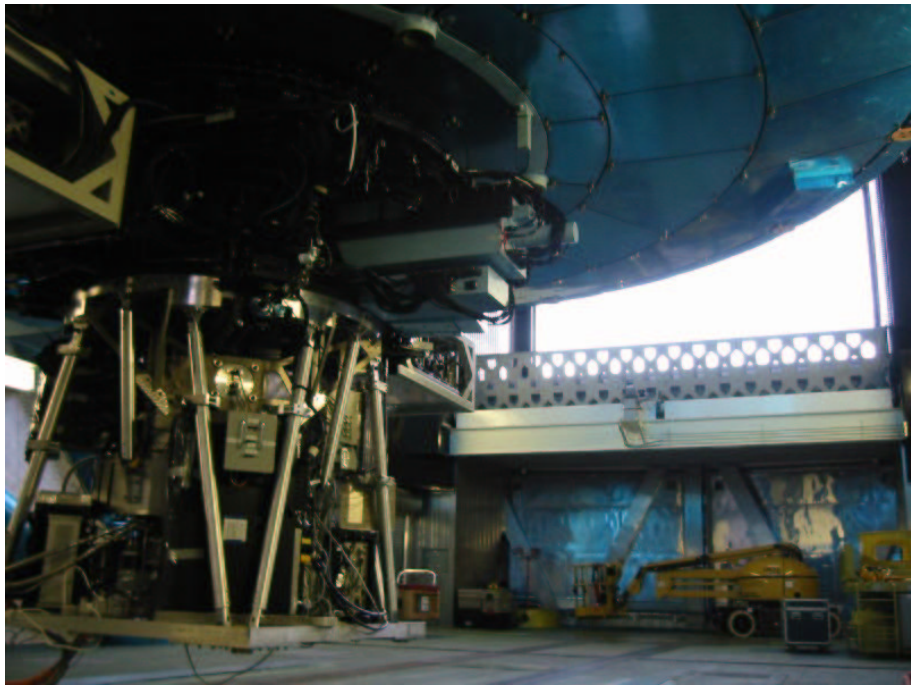
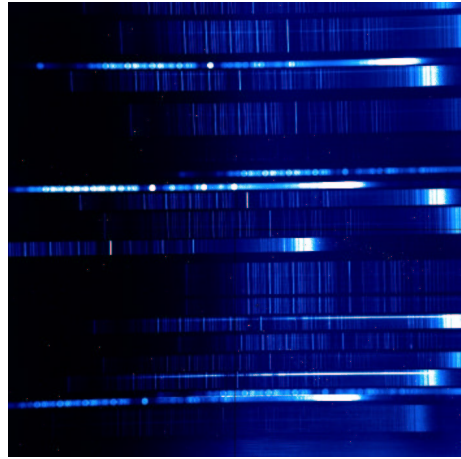
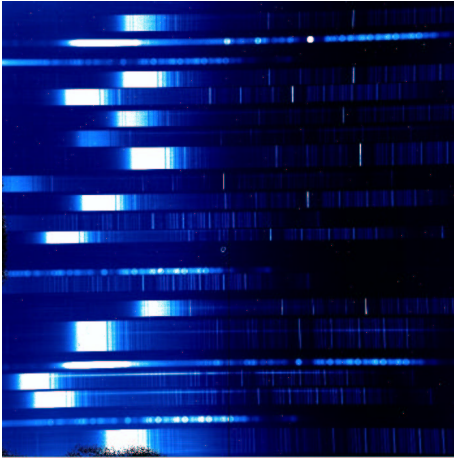
Spectroscopic observation in the near-infrared(NIR) wavelength is crucial to reveal the nature of high-redshift  $z \sim 1-4$  galaxies. The object-frame optical emission lines, such as [SII] $\lambda 6718, 6731$ , H $\alpha$ (6563Å), [NII] $\lambda 6548, 6583$ , [OI] $\lambda 6300$ , [OIII] $\lambda 5007, 4959$ , H $\beta$ (4861Å), [OII] $\lambda 3727$ , are important to examine the source of the ionizing photons, star-formation rate, inter-stellar matter metallicity, extinction of galaxies. Most of these emission lines fall in the NIR wavelength for the objects at redshift  $z > 1$ . In addition, for objects at redshift  $z \sim 1.3-3.0$ , all of the above emission lines and Ly $\alpha$ (1216Å), which are strong emission lines from typical star forming galaxies, escape from the observed-frame optical wavelength, thus it is difficult to determine redshifts of objects in the redshift range (“redshift desert”). In order to identify galaxies in the redshifts without any bias, the NIR spectroscopy for the object-frame optical emission lines is quite important.

Although already large amount of times of 8-10m class telescopes is consumed, the number of the obtained spectra is quite limited, a few 10s. This is because all of the above studies are conducted with the long-slit observation, i.e. one target at a time. In addition, compared with the optical observations, the sky background is brighter in the NIR, thus longer integration time ( $\sim 10$  hours) is required to detect a galaxy at the same redshift. Therefore, in order to examine natures of large numbers of  $z = 1 - 4$  galaxies statistically with less bias, multi-object slit observations in the NIR with long integration time on 8-10m class telescopes are crucial. But due to the technical difficulties with infrared instrumentation, currently the NIR multi-object spectrograph (MOS) instruments are only regularly available on 4-m class telescopes. Because of the small telescope apertures, studies with these spectrographs are limited to bright objects.

The MOIRCS, Multi-Object InfraRed Camera and Spectrograph is the first NIR MOS instrument for the 8-10m class telescopes in the world, which is optimized for observations of the distant galaxies.

We designed the MOIRCS cryostat systems and the cryogenic MOS system. The challenge in designing the MOIRCS cryostat system is the large size of the optical trains which consists of large optical elements to cover the wide field of view. The major challenges in developing a cryogenic MOS, which is available to  $K$  band, are how to provide a new mask securely during the observation in cryogenic environment, how to replace the stored masks without a thermal cycling of the main dewar, how to control the slit positions of the cooled masks, and how to acquire the faint target objects with a multi-slit mask. There are a variety of other unconventional challenges which are peculiar to the wide field NIR MOS spectroscopy. e.g. flat fielding, atmospheric effects, and thermal contraction effects of the multi-slit masks.

We successfully conducted multi-object slit spectroscopy of the faint distant galaxies with MOIRCS. The results of the first MOS test observations indicate that the MOIRCS is capable to detect not only the emission lines but also the continuum for the objects as faint as  $K=19$  mag, which are at  $z > 1$ , with integration times of a few hours.



# Contents

<b>1</b>	<b>Introduction</b>	<b>5</b>
1.1	Importance of NIR Spectroscopic Observations for Distant Galaxies . . . . .	5
1.2	Difficulties of a NIR MOS Instrument . . . . .	8
1.3	Multi-Object InfraRed Camera and Spectrograph (MOIRCS) . . . . .	9
<b>2</b>	<b>Cryostat</b>	<b>12</b>
2.1	Cryostat Structure . . . . .	12
2.1.1	Overview . . . . .	12
2.1.2	Cryostat Structure Analysis . . . . .	13
2.1.3	Main Dewar . . . . .	18
2.1.4	MOS Mask Dewar . . . . .	20
2.1.5	Housekeeping . . . . .	20
2.2	Cooling System . . . . .	22
2.2.1	The Design . . . . .	22
2.2.2	Multilayer Insulation . . . . .	24
2.2.3	Pre-cooling System . . . . .	24
2.2.4	Cooling-down Procedure . . . . .	25
2.2.5	Warming-up Procedures . . . . .	26
<b>3</b>	<b>Cryogenic MOS System</b>	<b>30</b>
3.1	Mask Exchange System . . . . .	30
3.1.1	Slit Mask Exchanger . . . . .	30
3.1.2	Position Sensing . . . . .	33
3.1.3	Mask Exchange Procedure . . . . .	35
3.1.4	Interlock . . . . .	37
3.2	Slit Mask . . . . .	40
3.2.1	The Selection of the Mask Material . . . . .	40
3.2.2	Thermal Contraction of the Masks . . . . .	42
3.2.3	Slit Design . . . . .	45
3.2.4	Slit Cutting . . . . .	46
3.2.5	Mask Installation . . . . .	48
<b>4</b>	<b>MOS Observation</b>	<b>50</b>
4.1	MOS Pointing . . . . .	50
4.1.1	Pointing Sequence . . . . .	50
4.1.2	Pointing Results . . . . .	53
4.1.3	Random Residual . . . . .	55
4.2	Spectroscopic Capability . . . . .	57



4.2.1	Resolution . . . . .	57
4.2.2	Efficiency . . . . .	61
4.2.3	Flat field images . . . . .	61
4.2.4	Flexure of the Instrument and Effect on Long Integration . . . . .	67
4.2.5	Atmospheric Effect . . . . .	67
<b>5</b>	<b>Spectroscopic Observations of Distant Galaxies</b>	<b>70</b>
5.1	Target selection and mask design . . . . .	70
5.2	Observation . . . . .	74
5.3	Data Reduction . . . . .	74
5.3.1	Spectra Cut-out . . . . .	74
5.3.2	Sky subtraction . . . . .	74
5.3.3	Wavelength Calibration . . . . .	74
5.3.4	Flat-fielding . . . . .	77
5.3.5	Rationing Star . . . . .	77
5.3.6	Results . . . . .	78
5.4	Conclusion . . . . .	80
<b>A</b>	<b>MLI Fabrication</b>	<b>84</b>
A.1	Materials . . . . .	84
<b>B</b>	<b>Liquid Nitrogen</b>	<b>86</b>
B.1	Properties of LN <sub>2</sub> . . . . .	86

# Chapter 1

## Introduction

### 1.1 Importance of NIR Spectroscopic Observations for Distant Galaxies

Spectroscopic observation in the near-infrared (NIR) wavelength is crucial to reveal natures of high-redshift galaxies, such as Lyman Break Galaxies (LBGs),  $K$ -selected luminous galaxies, and sub-mm selected galaxies. The object-frame optical emission lines, such as [SII]  $\lambda 6718, 6731$ ,  $H\alpha(6563\text{\AA})$ , [NII]  $\lambda 6548, 6583$ , [OI]  $\lambda 6300$ , [OIII]  $\lambda 5007, 4959$ ,  $H\beta(4861\text{\AA})$ , [OII]  $\lambda 3727$ , are important to examine the source of the ionizing photons (starburst or AGN ?), star-formation rates, inter-stellar matter metallicity, extinction (Balmer decrement) of galaxies (e.g. Osterbrock (1989)). As shown in Figure 1.1, some of these emission lines fall in the NIR wavelength for objects at redshifts  $z > 1$ . In addition, for objects at redshift  $z \sim 1.3 - 3.0$ , all of the above emission lines and  $Ly\alpha(1216\text{\AA})$ , which are strong emission lines from typical star forming galaxies, escape from the observed-frame optical wavelength, thus it is difficult to determine redshifts of objects in the redshift range (“redshift desert”). Though, Steidel et al. (2004) developed a new method to select star-forming galaxies in the redshift desert, the selection is biased to UV-luminous galaxies in the redshift range. In order to identify galaxies in the redshifts without such bias, the NIR spectroscopy for the object-frame optical emission lines is quite important.

In 1990’s, NIR spectroscopic observations of distant galaxies started for a few LBGs with 4-m class telescopes (e.g. Pettini et al. (2001)). These observations are limited in the signal-to-noise ratio because of the small aperture of the telescopes. In the next 10 years, the quality of data was improved with the NIR spectroscopic observation with the instruments attached to the 8-10m class telescopes, such as the OH-suppression Spectrograph (OHS) on the Subaru telescope, the Near Infra-Red SPECTrograph (NIRSPEC) on the Keck telescope, and the Infrared Spectrograph And Array Camera (ISAAC) on the VLT telescope. Pettini et al. (2001) observed 20 LBGs at  $z \sim 2.7-3.4$  with NIRSPEC/Keck and ISAAC/VLT with spectral resolution of  $R \sim 1500$  in the  $K$ -band (Figure 1.2). They examined the star formation rate in the LBGs with  $H\beta$  luminosity, and metallicity of the ISM with  $[OII]+[OIII]/H\beta$  ratio. Steidel et al. (2004), Erb et al. (2003,2004) report the observations of  $H\alpha$  emission line, which provides the most secure estimate on the SFR among the optical emission lines, for objects at  $z = 2 - 2.5$ . Sharply et al. (2004) obtained spectra of nine the starforming galaxies at  $z \sim 2$ . They have red optical to NIR colors ( $R - K > 4$ ), thus bright in the  $K$ -band ( $K < 20$ ).

Although already large amount of times of 8-10m class telescopes is consumed, the number of the obtained spectra is quite limited, a few 10s. This is because all of the above studies are conducted with the long-slit observation, i.e. one target at a time. In addition, compared with the optical observations, the sky background is brighter in the NIR, thus longer integration time ( $\sim 10\text{hr}$ ) is required to detect a galaxy at the same redshift. Therefore, in order to examine natures of large numbers of  $z = 1 - 4$  galaxies

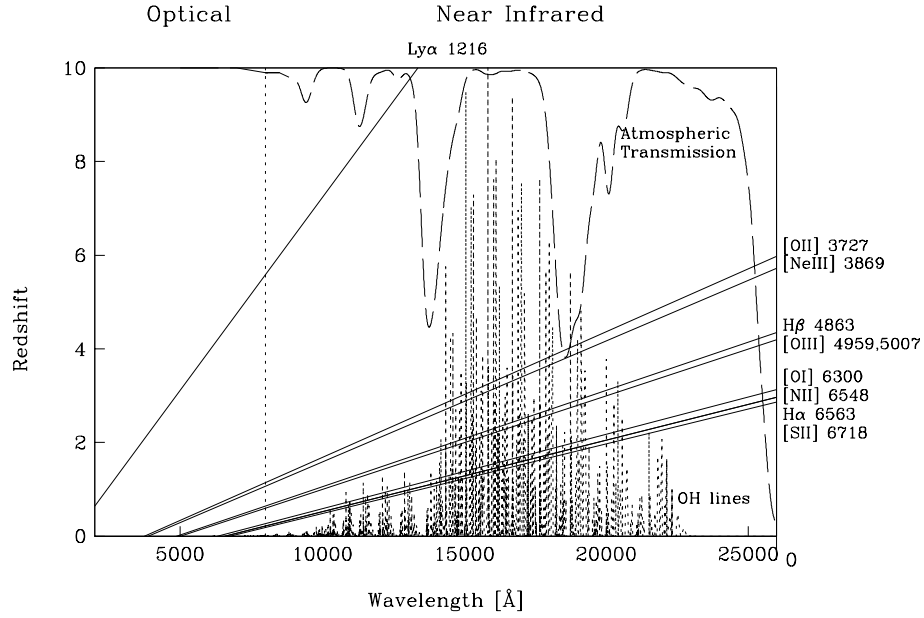


Figure 1.1: The wavelengths of strong emission lines as a function of redshifts. The atmospheric transmission is shown in long dashed line. It is 100% at the top and 0% at the bottom. A typical spectrum of OH lines is shown with dotted line, in order to show the strength of the night sky emission lines in the NIR in comparison with those in the optical wavelength.

statistically with less bias, multi-object slit (MOS) observations in the NIR with long integration time on 8-10m class telescopes are crucial.

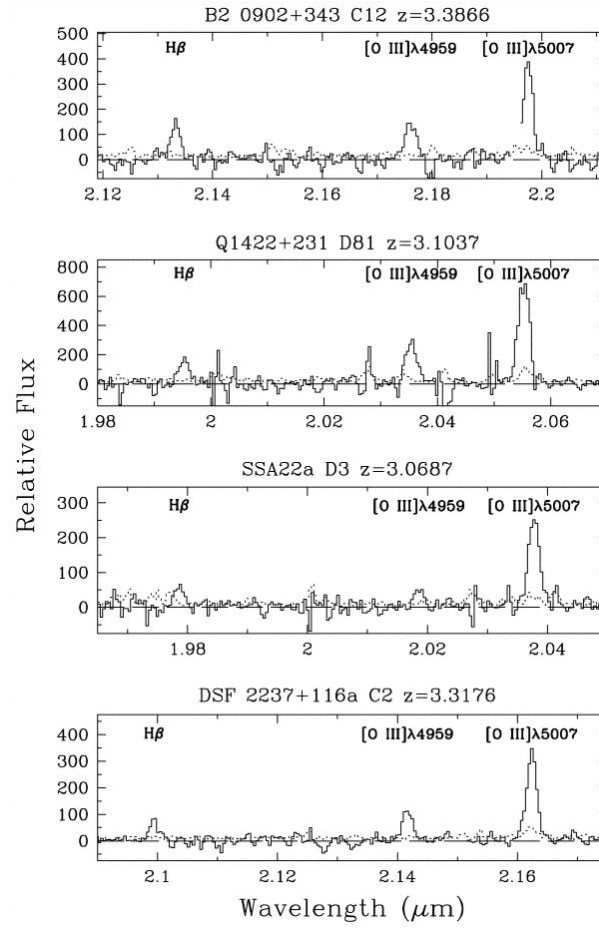


Figure 1.2: The examples of NIRSPEC K-band spectra of Lyman break galaxies on the Keck telescopes by Pettini et al. (2001). The exposure times are 6.0 hr, 1.8 hr, 2 hr, 2.0 hr for each object from upper to lower. The resolving power is  $R \sim 1500\text{--}1750$ . In each panel, the dotted line shows the  $1\sigma$  error spectrum.

## 1.2 Difficulties of a NIR MOS Instrument

Although it is crucial to conduct NIR MOS observations for distant galaxies, currently NIR MOS instruments are only regularly available on 4m class telescopes, InfraRed Imager & Spectrograph 2 (IRIS2) on Anglo-Australian Telescope, FLoridA Multi-object Imaging Near-IR Grism Observational Spectrometer (FLAMINGOS) on Mayall 4.0m telescope in Kitt Peak National Observatory (KPNO), and Long-slit Intermediate Resolution Infrared Spectrograph (LIRIS) on William Herschel Telescope, see Table 1.2. Because of the small telescope apertures, studies with these spectrographs are limited to bright objects in our Galaxy.

Why the number of operating NIR MOS instruments are limited ? What are the difficulties of such instruments ? Firstly, in order to reduce the thermal background from MOS masks, the masks need to be as cold as 100K. The masks must be cooled down uniformly to escape from the distortion to the mask, therefore the mask material should have a good thermal conductivity. Metals have a good thermal conductivity, but it is difficult to make small slits with  $\sim 100 \mu\text{m}$  widths on such materials with sufficient precision, 1/10 of the slit width. Thus making MOS mask itself is difficult. In addition, the mask exchange mechanism for such instrument needs to work under cryogenic environment. With low-temperature and low-pressure, reliable movement is quite restricted. Thus, the mask exchange mechanism is another difficulty in a cryogenic MOS instrument.

Secondly, developments of large format infrared arrays are delayed in comparison with optical detectors. Recently  $2048 \times 2048$  pixels (“2k $\times$ 2k”) detector is available, but still a few such detectors are required to cover large field of view (F.O.V.  $\sim$  several arcmins) with sufficient spatial sampling ( $\sim 0.''1$ ). For example, two 2k $\times$ 2k detectors are required to cover the Cassegrain focus of the Subaru telescope.

Thirdly, operation of such instrument has another difficulty. In order to replace MOS masks, thermal cycle of the cryostat is required. The exchange procedure needs to be done in a reasonable time scale, a few days. But, typically thermal cycle of a cryogenic instrument takes about a few weeks.

Table 1.1: Operating and planned infrared multi-object spectrographs using cryogenic multi-slit masks. (\*)Telescopes are still under construction.

Instrument	Telescope	F.O.V	Feature	First Light
<b>MOIRCS</b>	Subaru (8.2 m)	$6' \times 4'$	Cooled mask	2005
FLAMINGOS	KPNO (4.0 m)	$10' \times 10'$	Cooled mask	2001
LIRIS	WHT (4.2 m)	$4.'2 \times 4.'2$	Cooled mask	2002
IRIS 2	AAT (3.9 m)	$8' \times 8'$	Cooled mask	2002
EMIR	GTC (10.4 m)	$6' \times 4'$	Cooled mask	2006 *
MOSFIRE	Keck II (10 m)	$11' \times 4'$	Cooled mask	2009
FLAMINGOS 2	Gemini-S (8.2 m)	$6.'2 \times 2'$	w/MCAO,Cooled mask	2007
LUCIFER	LBT (8.2 m)	$\phi 4'$	Cooled mask, IFU, AO	2007 *
MMIRS	MMT (6.2 m)	$6.'8 \times 6.'8$	Cooled mask	2006

### 1.3 Multi-Object InfraRed Camera and Spectrograph (MOIRCS)

Table 1.2: Overview of the MOIRCS concepts.

Observation Modes	Imaging and Multi-Object Spectroscopy (MOS)
Field of View (F.O.V.)	$4' \times 7'$ for Imaging $4' \times 6'$ for MOS
Wavelength Coverage	0.85-2.5 $\mu\text{m}$ ( $z, J, H, K$ -band)
Detector	two $2048 \times 2048$ pixel HgCdTe (HAWAII-2) arrays
Pixel Scale	$0.''117 \text{ pixel}^{-1}$

In order to realize a NIR MOS instrument, it is required to overcome the above difficulties. The Multi-Object InfraRed Camera and Spectrograph (MOIRCS) is the first NIR MOS instrument for the 8-10 m class telescopes in the world, which is designed to realize the long integration NIR MOS observation for observations of the distant galaxies. We designed the cryogenic MOS system with unique solutions for the above difficulties. The cryostat system and cryogenic MOS systems are described in chapters 2 and 3, respectively. There are other NIR MOS instruments planned for other telescopes (see Table 1.2). Most of the instruments are still in construction or design phase and MOIRCS is a few years ahead.

MOIRCS has imaging capabilities in the wavelength range from 0.85  $\mu\text{m}$  to 2.5  $\mu\text{m}$  with  $4' \times 7'$  F.O.V. The focal plane of the Cassegrain focus of the Subaru Telescope is imaged onto two  $2048 \times 2048$  pixel HAWAII-2 HgCdTe arrays (Rockwell Scientific) with a pixel scale of  $0.''117 \text{ pixel}^{-1}$  (Table 1.3). The optical design is optimized to maximize the performance in the  $K$ -band.

All the components of MOIRCS inside the cryostat are cooled under 100 K. The optical system is designed to work at the temperature with consideration of a refractive index change of lens materials at 77 K and thermal contraction of the lenses. The details of the optical design are given in Suzuki (2006).

Figure 1.3 shows the optical layout. MOIRCS consists of two sets of identical optics. A gold-coated roof mirror placed just below the focal plane splits the light from the telescope. The divided light enters two identical optical trains after reflected by two gold-coated folding mirrors. Each optical train has four-lens collimator and six-lens camera systems. The collimator with a focal length of 620 mm generates a parallel beam and a pupil image of 50 mm diameter. The camera with a focal ratio of  $f/3.9$  makes an object image onto the detector with a pixel scale of  $0.''117 \text{ pixel}^{-1}$ , which adequately samples a point-source image under the best seeing condition ( $\sim 0.''3$ ) at the summit of the Mauna Kea. The lenses are made of  $\text{CaF}_2$ ,  $\text{BaF}_2$ , Fused Silica, and  $\text{ZnSe}$  that have an excellent transmission in the near-infrared wavelength. All these lenses except for the large  $\text{CaF}_2$  window are coated with anti-reflection coating. Its reflectivity ranges from 1.5 % to 2.5 % per surface depending on the materials and wavelength.

Figure 1.4 shows expected spot diagram of the imaging mode. Spots for the center and edge of the F.O.V. at 1.03  $\mu\text{m}$ , 1.25  $\mu\text{m}$ , 1.63  $\mu\text{m}$ , and 2.20  $\mu\text{m}$  are shown. The squares represent 2 pixel boxes. Because there is not significant chromatic aberration we do not need refocusing for the different wavelength.

The imaging performance analysis of the collimator shows that any point at the edge of the telescope secondary mirror is imaged within 0.3 mm square box on the cold-stop in the 2.5  $\mu\text{m}$  wavelength, while the pupil diameter is 50 mm. Thermal background radiation contaminating the secondary mirror image at the cold stop due to the aberration of the collimator system is estimated to be less than 3 % of the radiation from the sky. This is especially important for spectroscopic observation with wide wavelength coverage.

The imaging mode achieved its first light on September 2004 (Figure 1.6), and we confirmed the limiting magnitude of MOIRCS  $J \sim 23.5$  mag and  $Ks \sim 21.8$  mag for the total exposure times of 1800

s and 900 s respectively. Longer exposures and the limiting magnitude in  $H$ -band are still being tested. Total throughputs of the imaging mode were measured to be  $\sim 30\%$  in the  $H$  and  $K$ -band,  $\sim 17\%$  in the  $J$ -band.

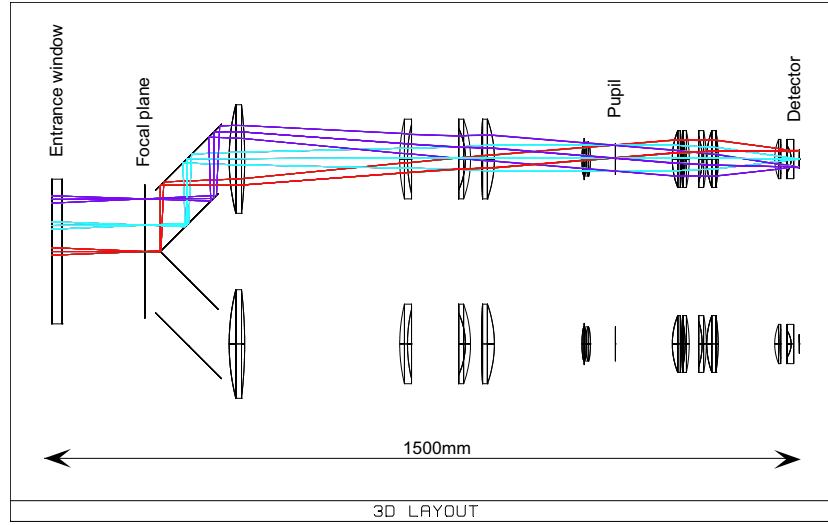


Figure 1.3: The layout of the optics. Plate in the left hand side is the camera window, and the planes at the right hand side represent the detectors. The optical rays are drawn only for one channel.

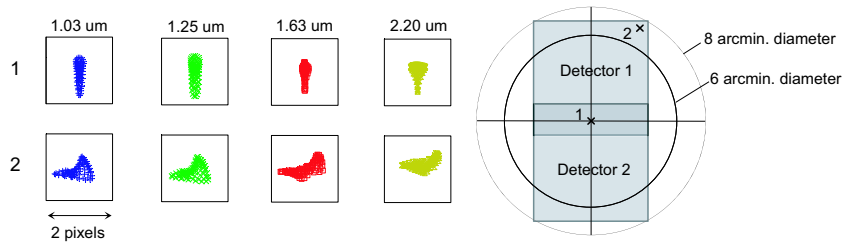


Figure 1.4: Spot diagrams of the optics and F.O.V. of the MOIRCS. Two squares in right figure represent scaled detectors at Cassegrain focal plane, while two circles correspond to  $6'$  and  $8'$  diameter respectively. The upper column and lower column in the left figure represent the field positions shown in the right figure. Each box has two pixel size.

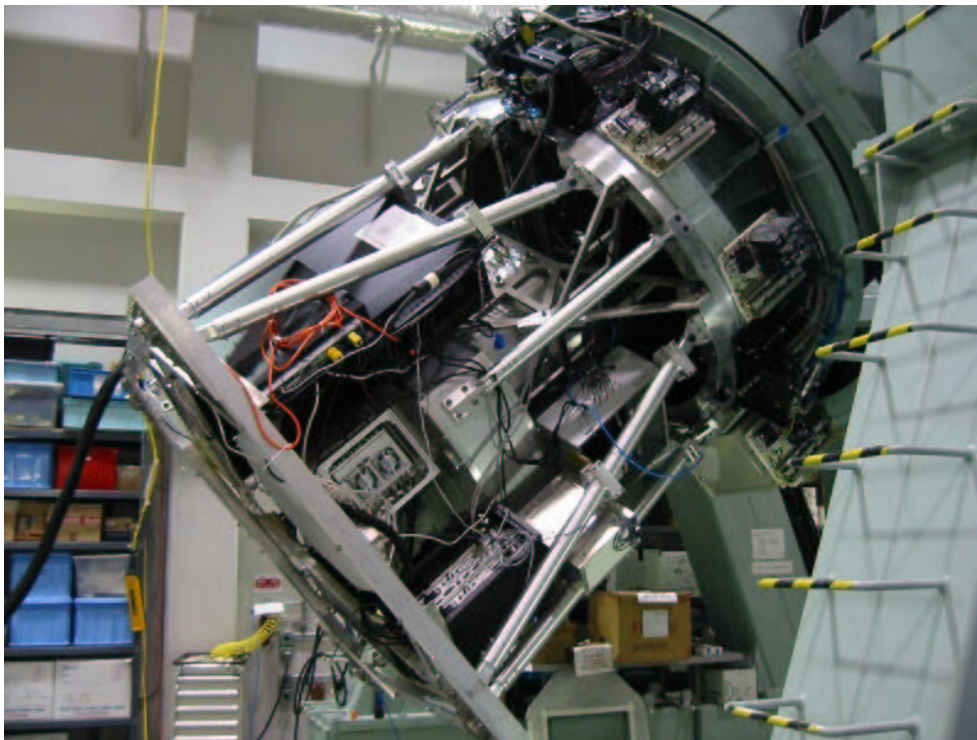


Figure 1.5: MOIRCS on the Cassegrain simulator in Hilo under flexure testing.



Figure 1.6: The first light image of M42 Orion region. Analyzed by Ichi Tanaka.



## Chapter 2

# Cryostat

The cryostat is a vacuum vessel consisting of two sections: a main dewar and a MOS mask dewar. Each section is made of machined aluminum alloy. Since the heat mass of the cold structure is huge, liquid Nitrogen ( $\text{LN}_2$ ) pre-cooling system is necessary together with cryocooler. A multi-layer insulation (MLI) is used to insulate from thermal radiation. To avoid thermal stress to the detectors and optical components, both warm-up and cool-down procedures need to be manually controlled.

## 2.1 Cryostat Structure

### 2.1.1 Overview

We designed the MOIRCS cryostat systems and conducted finite element analysis (FEA) of the whole structure. The challenge in designing the MOIRCS cryostat system is the large size of the optical trains which consists of large optical elements to cover the wide field of view.

MOIRCS has two cryostat systems; a main dewar enclosing the optical trains and a MOS mask dewar holding the mask storage system. Figures 2.1 and 2.2 show the sectional and outside views of MOIRCS, respectively. There are two sets of the identical optical trains. Both of the optical trains and detectors are mounted on the both sides of the “optical bench”, which is 20 mm thick aluminum alloy. The bench is suspended from the inner surface of the main dewar with G10 epoxy glass-fiber bracket straps (“G-10 straps”), which have low thermal conduction, low-thermal contraction, and stiffness in the cryogenic temperature. Filter, grism, and cold stop wheels are placed in the collimated section of the each optical train. Cryogenic motors drive these wheels, which are also attached to the optical bench.

The cryostats and electronic devices are held in  $2\text{m} \times 2\text{m} \times 2\text{m}$  envelop and attached to the Cassegrain flange of the Subaru telescope. A large ring structure above the instrument is the Cassegrain flange mounting unit (“top ring”). The dewars are fasten to the top ring with four “delta wing” support structures and four “support” arms. The total weight, including the top ring, electronics, and other housekeeping components, is about 2000kg.

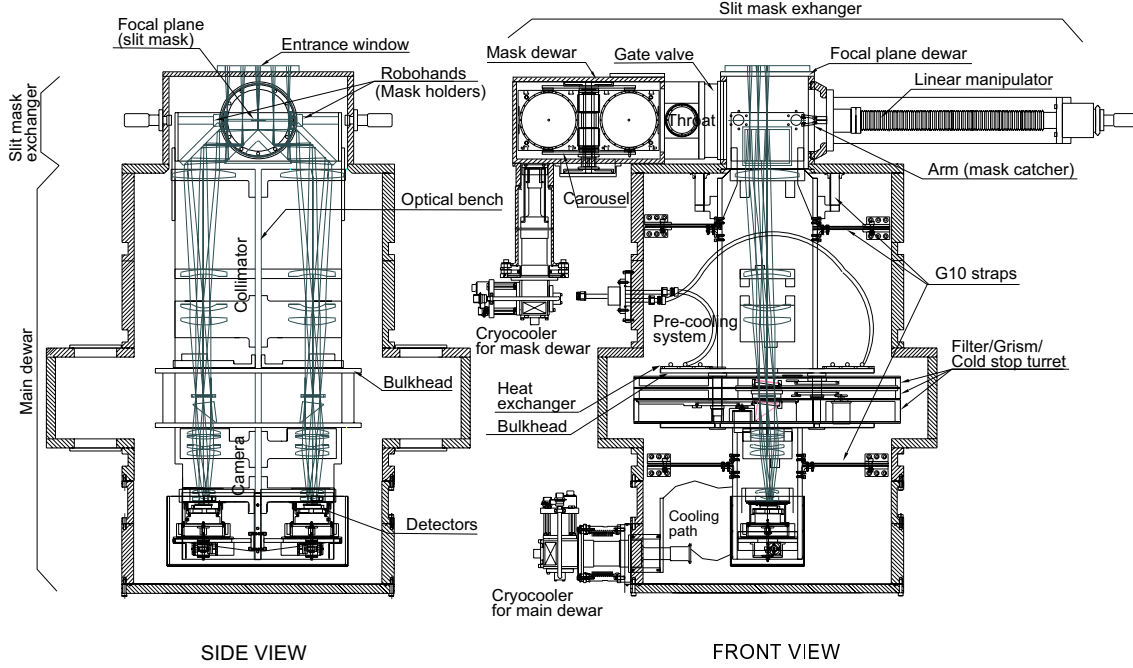


Figure 2.1: The internal structure of the MOIRCS cryostat; front view (left) and side view (right). Some parts are shown only in the side view for clarity.

### 2.1.2 Cryostat Structure Analysis

We performed finite element analysis (FEA) for the cryostat structures to determine the thickness of the cryostat wall, and number of supports. There are two requirements. 1) The flexure of the structure must be well below the yield strength of the aluminum. The maximum internal stress should not exceed the yield strength of 120 MPa, 300 MPa, and 120 MPa for Al6061, Al6061-T651, and stainless steel respectively at a room temperature. 2) The displacement of the structure against the Cassegrain flange needs to be smaller than  $200\text{ }\mu\text{m}$ , which is a requirement from the optical analysis.

The analysis was done for an extreme case with the telescope elevation of  $0^\circ$ , i.e. horizontal configuration. It should be noted that the elevation does not go below  $30^\circ$  during typical observations, and the telescope has low elevation limit of  $15^\circ$ . The FEMLEEG software package (Hoct System) was used for the FEA analysis.

At the sea level, the maximum deflection of the wall is calculated to be about 0.3mm at the center of the aluminum wall with 20mm thickness. The maximum stress is estimated to be 24.3 MPa, which is well below the yield strength. The aluminum plate with 20mm thickness is sufficient to support the cryostat structure even under the sea level condition. At the summit of Mauna Kea, the vacuum dewar is exposed to less pressure ( $< 64\text{ kPa}$ ) than at the sea level (101 kPa)

The FEA model configurations of the cryostat structure and the optical bench are shown in Figures 2.4 and 2.5. The directions of the gravity are set to be  $-z$  (telescope at vertical),  $x$  (telescope at horizontal, gravity parallel to the long side of the field of view), and  $y$  (telescope at horizontal, gravity perpendicular to the long side). The results are summarized in Tables 2.1 and 2.2. The calculated displacements are smaller than the specification. The stress distribution of the delta wings are shown in Figures 2.7. The calculated stress is much smaller than the yield strength of aluminum and the structure is stiff enough to support the whole structure.

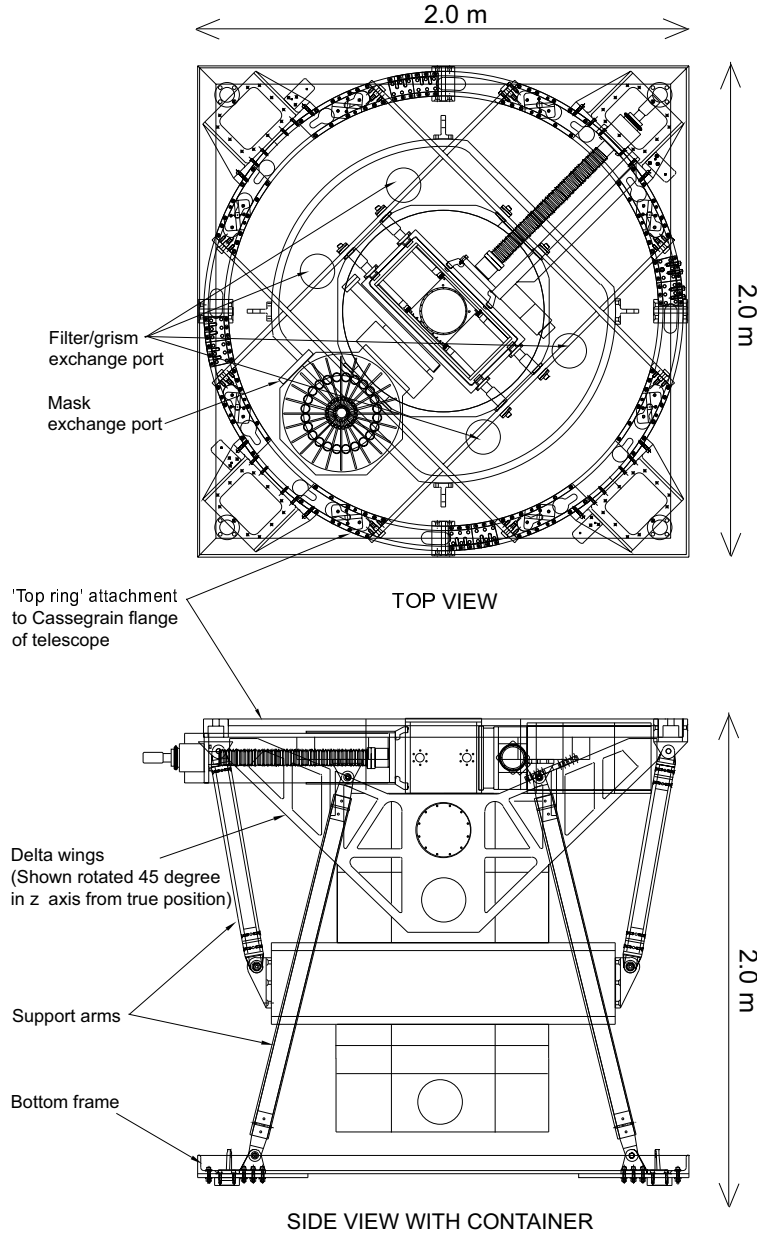


Figure 2.2: The outer structure of the MOIRCS; Top view (upper) and side view (lower). Delta wings are shown rotated by  $45^\circ$  from their original positions for clarity.

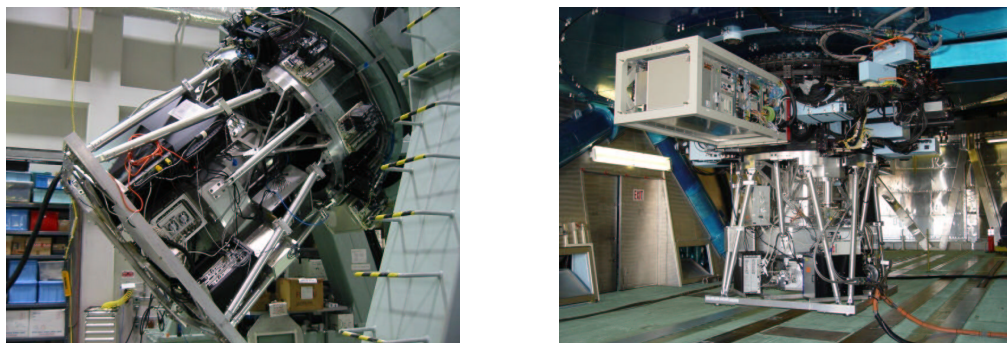


Figure 2.3: (Left) MOIRCS mounted on the Cassegrain simulator in Hilo. (Right) MOIRCS mounted on the Cassegrain flange of the Subaru Telescope.

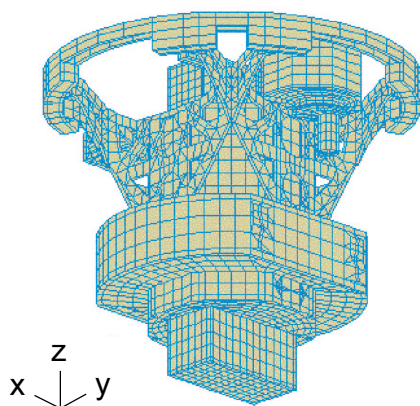


Figure 2.4: A model layout for FEA. The support arms are not shown for clarity.

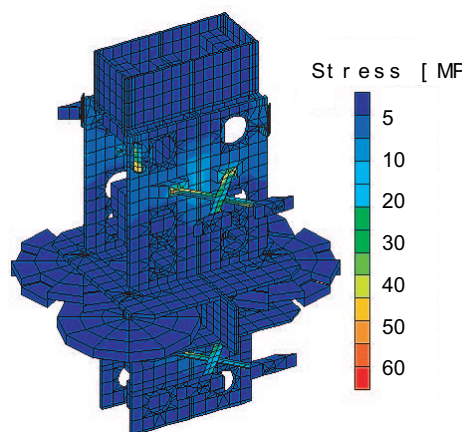


Figure 2.5: The stress distribution of the optical bench. The maximum stress is about 60 MPa at the joint of G10 straps.

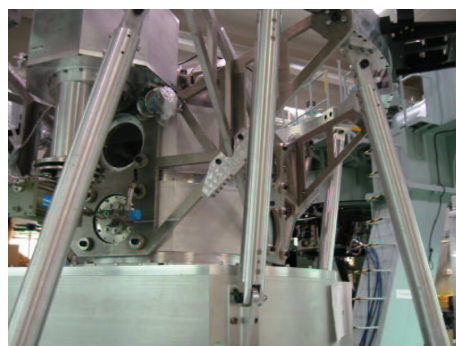


Figure 2.6: The delta wings and support arms without the main dewar (Left) and with the main dewar (Right).

Table 2.1: FEA results of the maximum displacement and the maximum stress for the dewar.

Gravity direction	MAX displacement [ $\mu\text{m}$ ]	MAX stress [Mpa]
$g = -z$	70 At corner of the mask dewar	4.9 At upper vertical G10 strap
$g = x$	170 At upper side wall	4.7 At lower horizontal G10 strap
$g = y$	122 At last lens of Camera	4.7 At upper horizontal G10 strap

Table 2.2: FEA results of the maximum displacement and the maximum stress for the detectors.

Gravity direction	MAX displacement [ $\mu\text{m}$ ]	MAX stress [Mpa]
$g = -z$	57	3.7
$g = x$	163	3.1
$g = y$	122	0.5

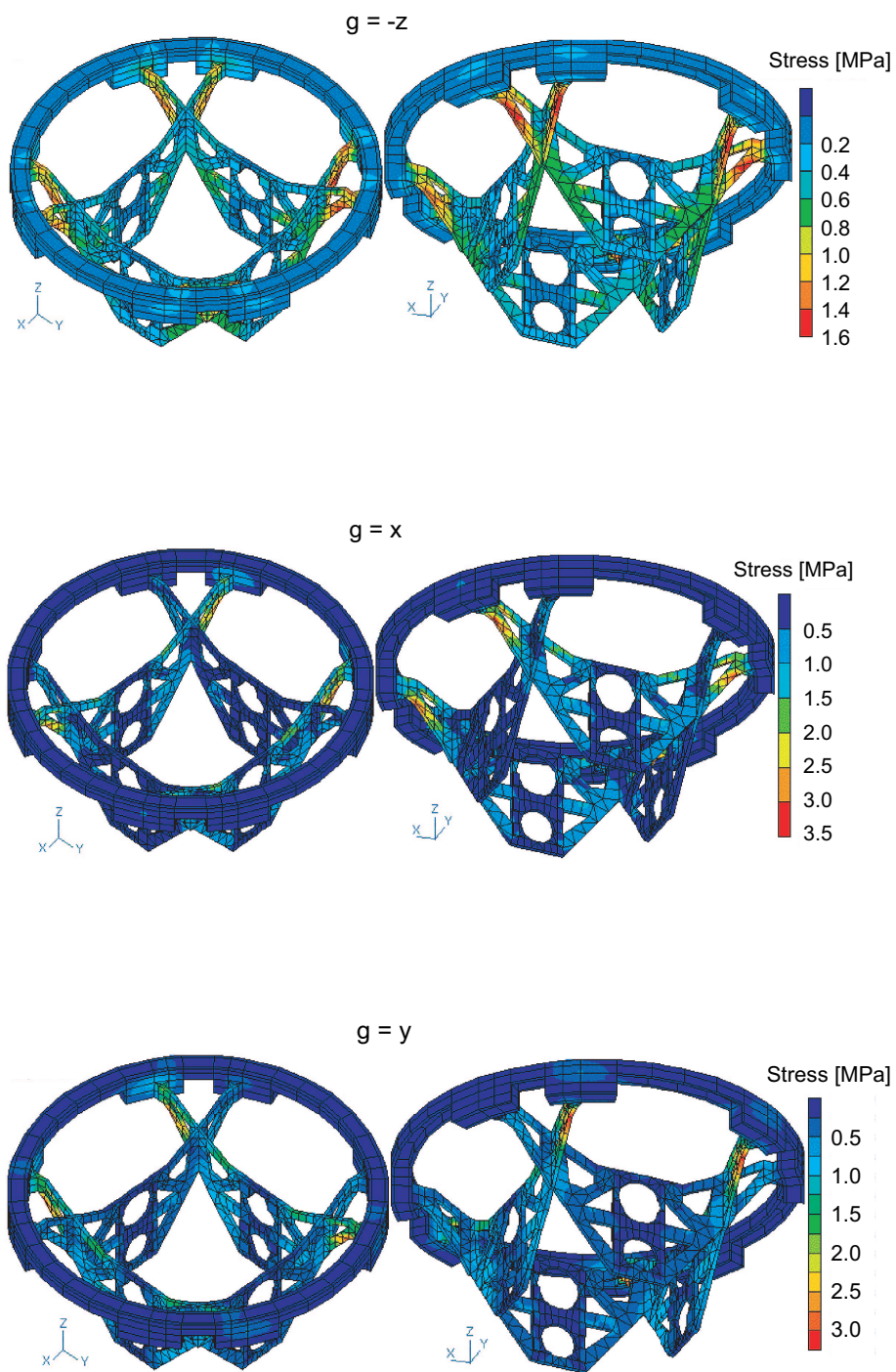


Figure 2.7: The stress distribution for gravitation direction  $g = -z, x, y$ . Only delta wings and top ring are shown.



### 2.1.3 Main Dewar

The main dewar provides a vacuum and cryogenic environment for the detectors and all the optical components inside the dewar. The main dewar is not one piece vessel but consists of four octagonal, one square and one elliptic shaped vacuum vessels (Figure 2.8). Following the FEA analysis, all of the out side structures are fabricated from forged Al6061 aluminum tubes. Between each joint of the vessels, large custom-made O-rings with equivalent diameters of 1310 mm and 838 mm are used.

A Gifford McMahon cryocooler SRDK-408S manufactured by Sumitomo Heavy Industries (SHI) is mounted on the bottom of the dewar and it cools the detectors and optical components down to 77 K. The optical bench is supported but thermally insulated from the wall of the main dewar in a room temperature with 12 brackets of G10 epoxy glass-fibre straps. In an addition, multi-layer insulation (MLI) blankets insulate all of the components from the thermal radiation from the wall.

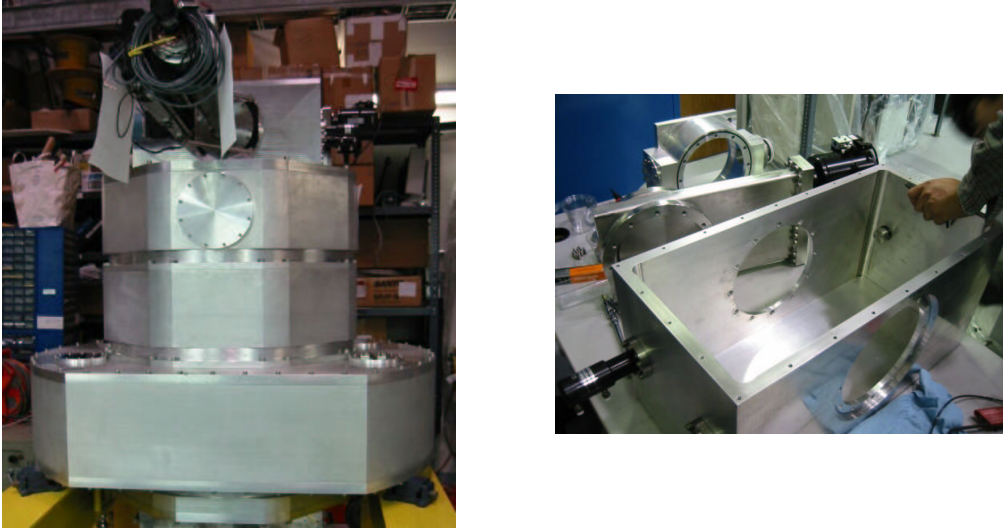


Figure 2.8: (Left) The upper part of the main dewar. The sections are bolted each other with custom-made large O-rings between them.

(Right) The focal plane dewar, which will be attached to the top of the main dewar, the gate valve, and the throat.

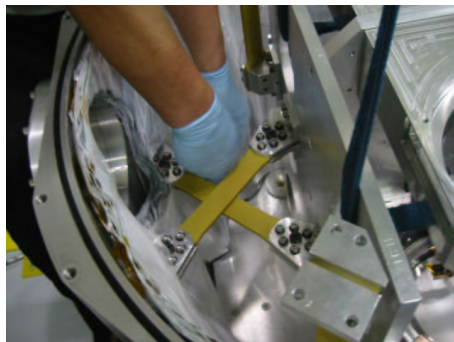


Figure 2.9: (Left) The optical bench installed in the largest section of the main dewar. (Right) G10 straps supporting the optical bench.

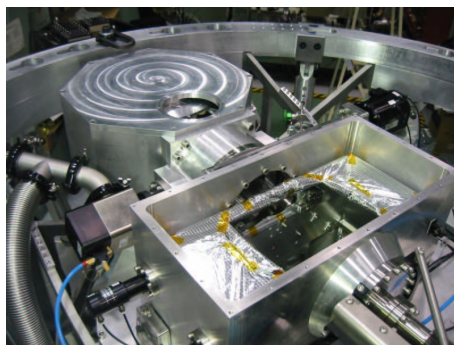
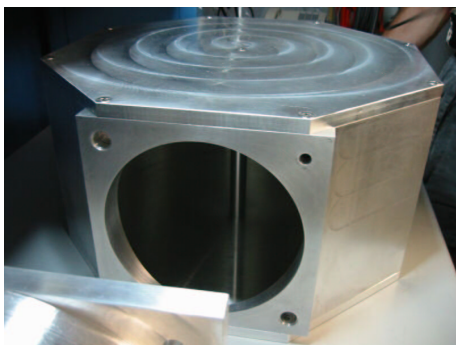


Figure 2.10: (Left) The mask dewar.(Right) Top view of the main dewar.



### 2.1.4 MOS Mask Dewar

The mask storage (“carousel”) is enclosed in the MOS mask dewar, which can be thermally detached from the main dewar by the “Gate valve” during the MOS mask installation. The mask dewar is an octagonal shaped vessel and attached next to the top vessel of the main dewar near the focal plane of the telescope (Figure 2.1, 2.10).

In order to minimize a time required to replace the masks, the time for the cooling down and warming up of the mask dewar should be as short as possible. Ideally mask replacement should be done in a daytime so that MOS observation can be continuously carried out. Therefore, efficient cooling and warming of the masks are crucial functions for the dewar. Therefore one SHI cryocooler is mounted bottom of the dewar to cool the stored slit-masks down to 100 K. The total heat-mass of the dewar and the masks is not so heavy thus one cryocooler is sufficient to cool down the masks. Efficient thermal coupling between the cold head and the masks themselves is another important factor. The details of the coupling are described in Section 3.

### 2.1.5 Housekeeping

In order to monitor the vacuum condition in the main and mask dewars, four vacuum gauges are attached. A turbomolecular pump (VARIAN Turbo-V 3000 HT) is attached only to the carousel side, because the main dewar should not be pumped while the mask dewar is open. The configuration of the vacuum system is shown in Figure 2.11.

Molecular sieves are used as a cryo-absorption pump. Molecular sieves have a much higher equilibrium capacity for water vapor under lower temperature and lower pressure conditions and very effective in reducing the water vapor content of gases. Some sieve canisters (Figure 2.12) are placed near a coldhead and bulkhead (pre-cooling point).

Temperatures of several crucial places inside the dewars; e.g., bulkhead (pre-cooling point), collimator (optical bench), heatpath (coldhead of cryocooler), robohand (mask temperature during MOS observation), detectors for the main dewar, coldhead of cryocooler and slitmask for the mask dewar, are monitored with the platinum sensors. These status informations are filed to the internal database of the MOIRCS control software system and can be checked through a website.

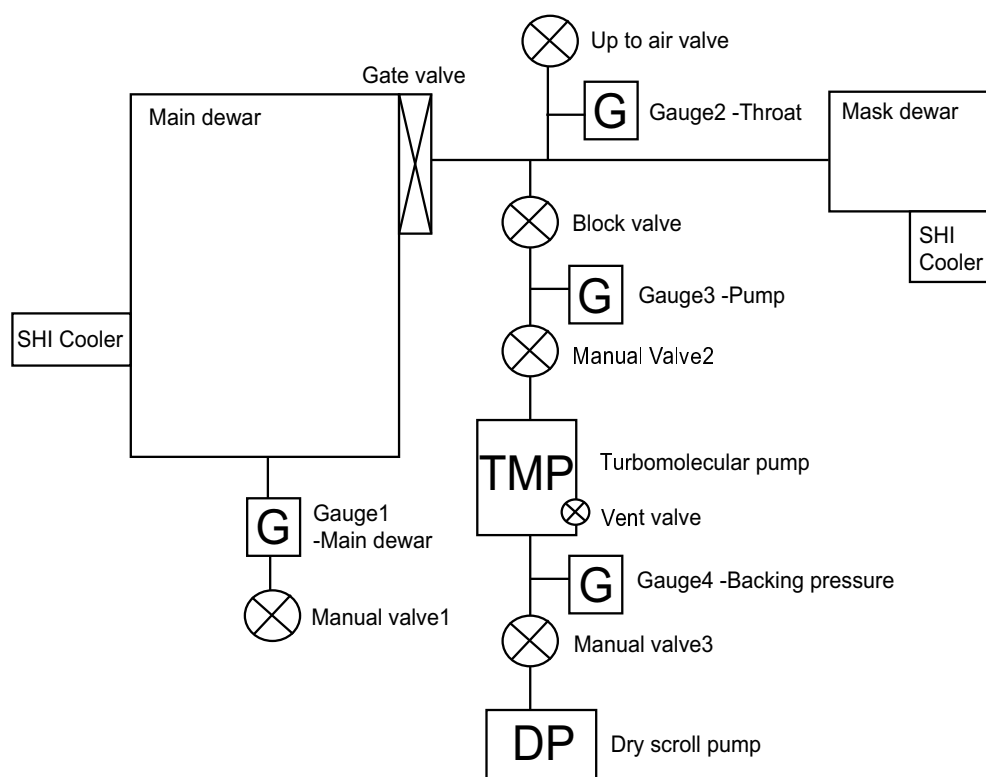


Figure 2.11: Vacuum configuration of the cryostat.

Table 2.3: Rough estimate of the mass in the main dewar.

	weight [kg]
Optics (Collimator)	90
Optics (Camera)	40
Optical bench	110
Filter/Grism Turrets	130
Detectors and electronics	10
Pre-cooling system	15
MOS articles (robohands, rails...)	2
Housekeeping (heaters, heatpath, molecular sieves...)	10
Total	407

## 2.2 Cooling System

### 2.2.1 The Design

In order to keep the thermal background radiation from the optical trains well below the background level from the sky (or the telescope), the optical trains should be wrapped with a structure cooled down to 100K. Total weight of cold components in the main dewar is roughly 400 kg. An itemized list is shown in Table 2.3. The heat mass is dominated by the structural parts made of aluminum alloy. Since the specific heat of aluminum alloy Al6061 is about 900 J/kg/K at 300 K, the total heat mass of the cold components from 273 K (typical temperature at the summit of Mauna Kea) to 100 K is estimated to be about  $6.2 \times 10^7$  J. In addition, the surface area of the main dewar and MLI are larger than 6 m<sup>2</sup>, thus thermal radiation from the surfaces is not negligible. Because the heat mass and the thermal transfer are large, pre-cooling system with liquid nitrogen (LN<sub>2</sub>) is required during the cooling down procedure.

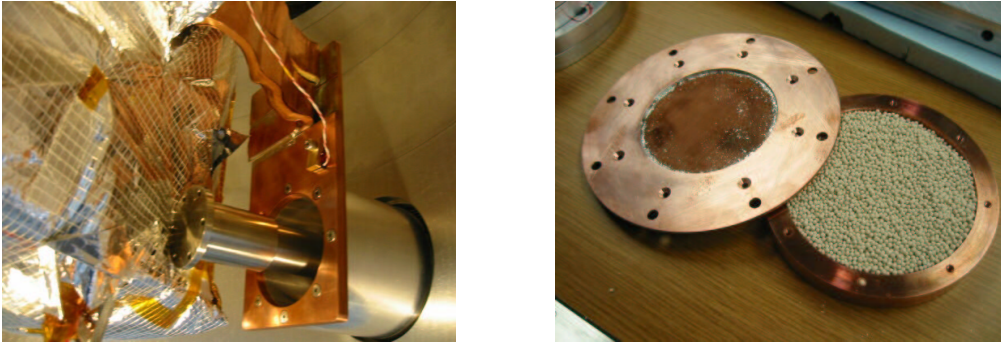


Figure 2.12: (Left) The cooling path made of OFHC straps and Tellurium copper plate. (Right) The molecular sieve canister made of copper and copper mesh for good conduction.

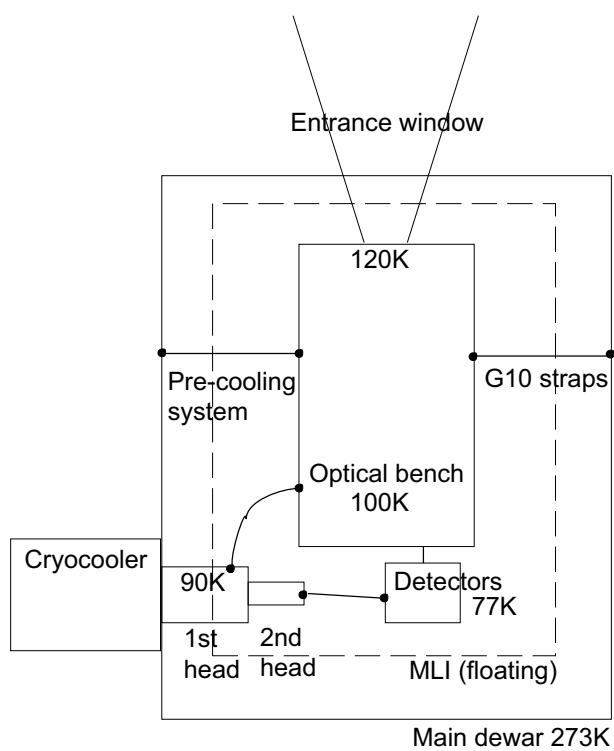


Figure 2.13: The schematic of the thermal environments.

### 2.2.2 Multilayer Insulation

Because the space inside the main dewar is limited, a multilayer insulation system (MLI), instead of radiation shield made of aluminum plate, is used to intercept the thermal radiation from the wall of the main dewar. The system consists of low-emittance (highly reflecting) radiation shields (polyester/polyimide film with pure thin aluminum coatings) with spacer netting. MLI is placed perpendicular to the heat flow to enable the layer to reflect large fraction of the radiation from the wall of the dewar at room temperature.

The thermal cut efficiency depends on vacuum conditions in the interstice spaces of the MLI, since the gas between the layers transfer the heat efficiency. Sufficient efficiency can be achieved under condition with  $10^{-5}$  to  $10^{-7}$  torr pressure. To vent the air inside of the cryostat efficiently, each layer has a lot of small air holes.

The number of MLI layer is determined based on a theoretical analysis. For highly vacuumed MLI, heat is transferred primary by radiation and solid conduction. The radiative thermal conductivity between the internal surface of the dewar and the external surface of the shields under can be obtained from

$$Q_{ds} = \frac{\sigma A_d (T_d^4 - T_s^4)}{\frac{1}{\epsilon_s} + \frac{1}{\epsilon_d} - 1 + \left( \frac{2}{\epsilon_s} - 1 \right) n}$$

where  $\sigma$  is the Stefan - Boltzmann constant,  $A_d$  an area of the dewar and shields,  $T_d$  and  $T_s$  temperature of surface of the dewar and outside of MLI shields,  $\epsilon_s$  and  $\epsilon_d$  emissivity of the MLI and the dewar,  $n$  number of the layers. The radiative thermal conductivity between the internal surface of the shields and the surface of the optical bench can be obtained from

$$Q_{sb} = \frac{\sigma A_s (T_s^4 - T_b^4)}{\frac{1}{\epsilon_s} + \frac{A_s}{A_b} \left( \frac{1}{\epsilon_b} - 1 \right)}$$

where  $A_s$  and  $A_b$  are an area of the shield and the optical bench,  $T_b$  temperature of the optical bench,  $\epsilon_b$  the emissivity of the optical bench. It is difficult to estimate the conduction due to the direct touching of the thin MLI layers to the optical bench. Thus, we assumed that the conduction will increase  $0.5 \text{ Wm}^{-2}$  by increasing the number of layer.

The heat flow from the surface of the dewar to the optical bench is derived as shown in Figure 2.14. The heat transfer will be minimized with ten layers of MLI. We ascertained that the ten layers of MLI works well enough as a radiation shield in the main dewar.

We fabricated MLI as shown in Figure 2.15. The 10 sets of thin ( $t \sim 9 \text{ } \mu\text{m}$ ) polyester cloth with aluminization to both sides and polyester netting ( $t \sim 200 \text{ } \mu\text{m}$ ), are sandwiched with mylar aluminized one side and reinforced with 100 denier for both outside of MLI. They are sewn together slackly on minimum points with cotton thread (Figure 2.15). The MLI should be baked out to minimize outgas (most of them is moisture) in a vacuum vessel with heaters before installing the main dewar. The detail of materials for MLI are described in Appendix A.

### 2.2.3 Pre-cooling System

The pre-cooling with liquid nitrogen ( $\text{LN}_2$ ) is used to accelerate the cooling-down process of the whole cryostat system, though it can be cooled by the first stage of a Sumitomo cryocooler basically. The  $\text{LN}_2$  heat exchanger is shown in Figure 2.17. Heavy-walled seamless copper tubings are silver-soldered onto Tellurium copper plates. Tellurium copper is selected, because it has high thermal conductivity and good temper to cut and grind. Such a machinability is important for tight metal-to-metal surface contact which is the key to good thermal performance of the exchanger system. This heat exchanger is mounted tightly on the "bulkhead" as shown in Figure 2.17. The bulkhead is connected to the optical bench with

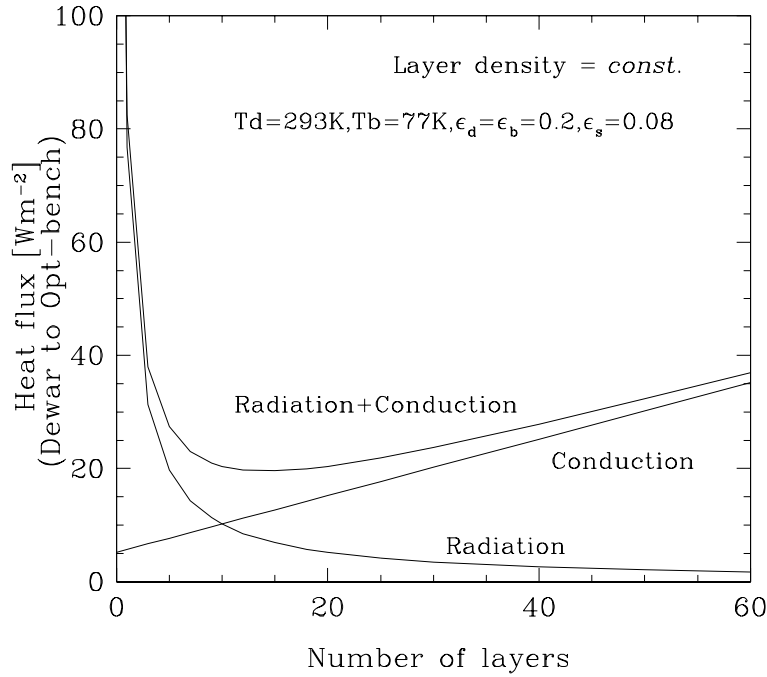


Figure 2.14: Heat Flux as a function of number of layers (Layer density is constant)

a limited thermal path, in order to escape from thermal shock to the optical bench system during the pre-cooling procedure. The pressure test of the exchange system was conducted upto 100 psi. Helium leak test was also performed.

The exchanger design needs to avoid turning the pre-cooling system into a heat source during operations. The stainless steel flexible hoses is long enough to insulate a heatflow through the heat exchanger from the surface of the main dewar.

Inside the pathway of LN<sub>2</sub>, especially at the part of copper pipe, is at low temperature during operation, therefore inside the pathway must be pumped out anytime except pre-cooling. If remaining LN<sub>2</sub> evaporates inside the heat exchanger, an internal pressure becomes expand and damages on the spots of silver-soldering.

The mass of the aluminum cold structure is more than 400 kg. Since the latent heat of 1 liter LN<sub>2</sub> is sufficient to cool 1 kg of aluminum from room temperature to 77 K (see Appendix B), it is expected that 400 liters of LN<sub>2</sub> will be required to cool the system. In reality 700 liters of LN<sub>2</sub> is required for pre-cooling of the system at the summit of Mauna Kea.

#### 2.2.4 Cooling-down Procedure

The typical transitions of temperatures and pressures during the cooling down procedure are shown in Figure 2.18. The cooling down of the optical components and detectors must be slower than 3~5 K/hour to avoid over-stressing of these components. The flow rate of LN<sub>2</sub> must be controlled manually during the pre-cooling procedure. The cooling down takes about a week at the summit for LN<sub>2</sub> cooling with 10 hours per day.

Both warm-up and cool down must be managed so that material that is out-gassed and/or trapped in getters does not end up preferentially on optical surfaces or detectors. During warming-up and cooling-

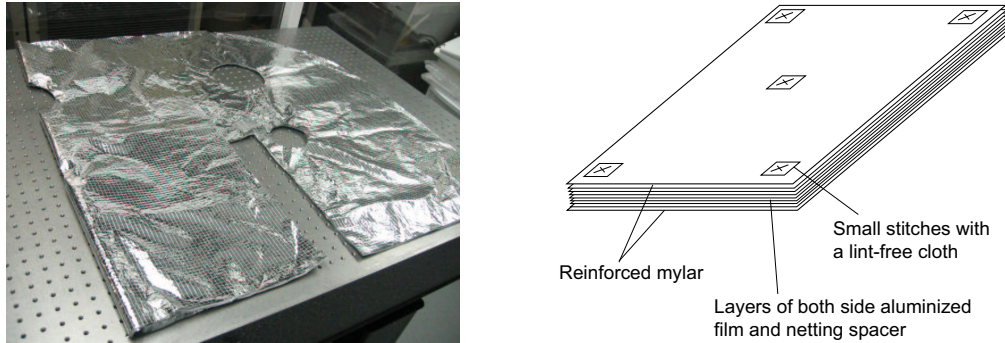


Figure 2.15: (Left) A sample of MLI blanket for the turret part.  
(Right) The schematic of MLI, which is 10 layers of MLI are sandwiched by reinforced aluminized film.

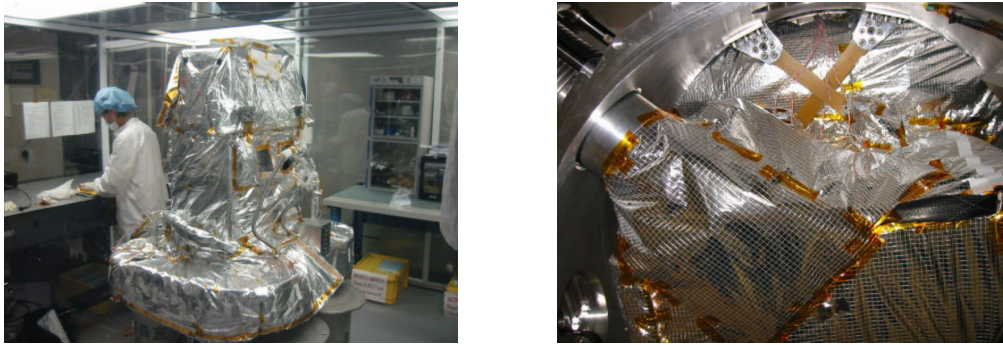


Figure 2.16: (Left) Dressing the optical bench in the clean room with MLI blanket. Upper optical bench is shown.  
(Right) Bottom of the optical bench. The coldhead is shown at left. G10 straps connect the optical bench and the internal surface of the main dewar penetrating the MLI.

down, the cryocooler for MOS must be running as a cryo-pump getter.

Typical temperatures during operations are shown in Figure 2.13, 2.18. The detector temperature is kept as 77K and the optical bench is cooled down to 100K. Temperature variations arise from several reasons potentially. These include (a) variations in ambient temperature (b) variations in cryocooler performance, whether due to orientation, aging, contamination, or other causes, and (c) variation of heat inputs from internal mechanisms, heater resistors, etc.

### 2.2.5 Warming-up Procedures

Same as for the cooling down procedure, the system must reach ambient temperature at the rate of 3 ~ 5 K/hour to avoid thermal shock to the components inside. Warming up is done using two 300 W internal heating resistors. The typical transitions of temperatures and pressures during warming up procedure are shown in Figure 2.19. Approaching room temperature the dewar is back filled via a secure inlet valve with temperature controlled, heated dry  $N_2$  to equalize the internal temperatures.

During warming-up, the cryocooler at the mask dewar need to be kept running to absorb out-gas from components inside the main dewar, and the pressures need to be monitored. A very small amount of  $H_2O$  on the surface inside dewar may evaporate to the air through sublimation, i.e. changes from ice or snow to water vapor directly, skipping the liquid phase, and re-absorbed by a colder surface (usually

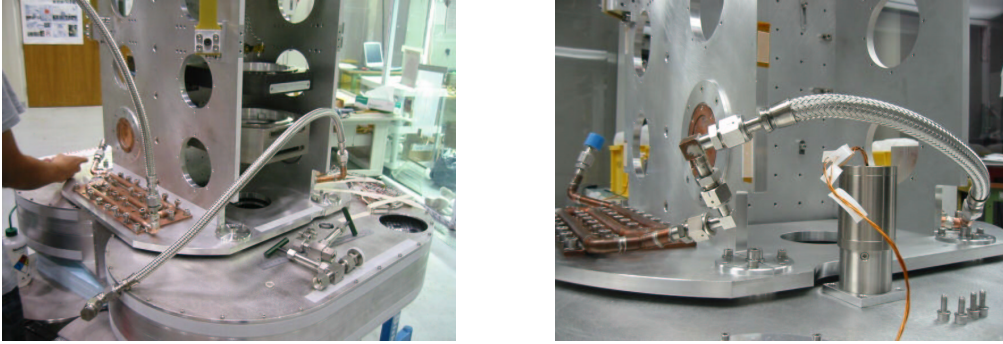


Figure 2.17:  $\text{LN}_2$  heat exchanger on the bulkhead. Two exchanger are on both side of the bulkhead and connected by the stainless flexible hose with using VCR copper gaskets.

optical elements and detectors thermally far from the heater). In order to avoid the re-absorption, the pressure inside the dewar should be kept lower than the sublimation curve of the ice. The temperature - pressure curve with sublimation curve of ice is compared with the typical transition of temperatures and pressures during the warming-up procedure in Figure 2.19. The temperatures and pressures are successfully controlled to escape from the sublimation curve.



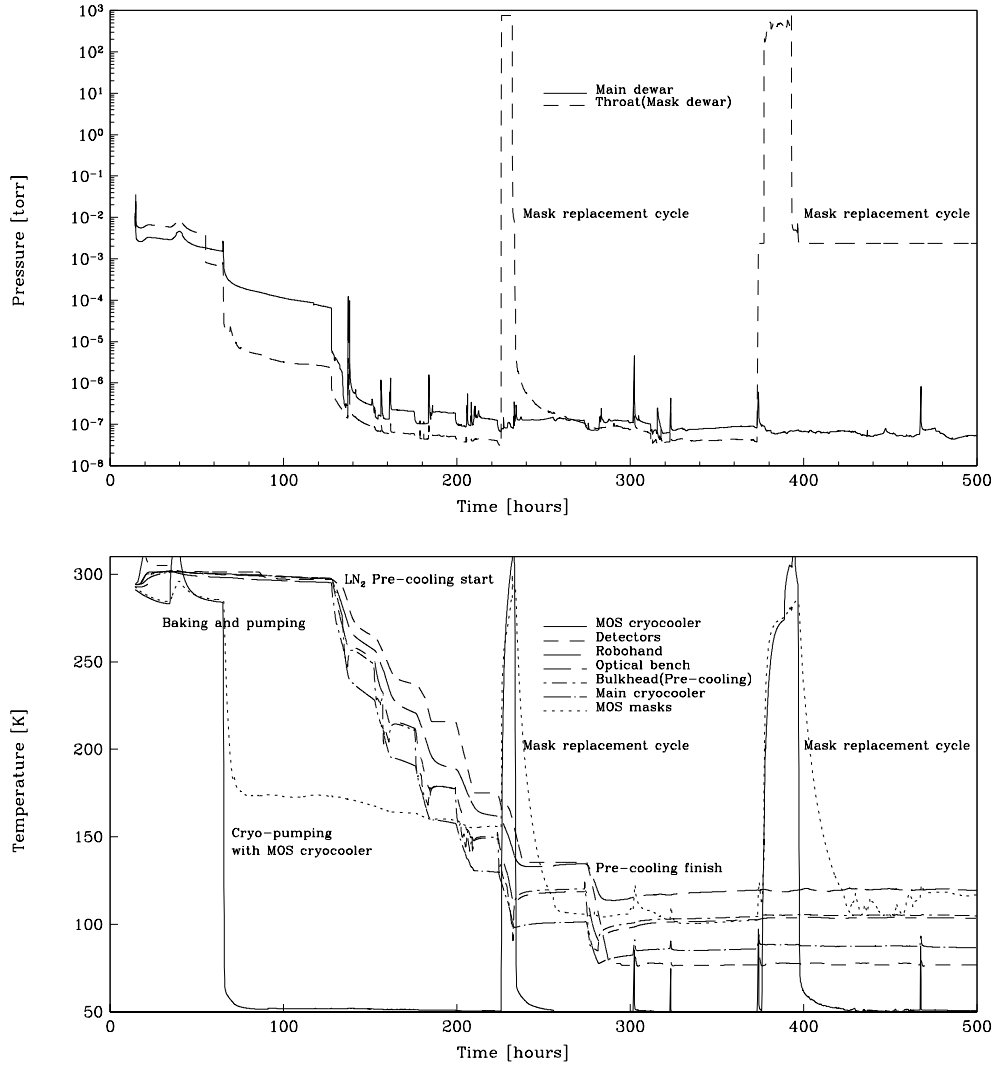


Figure 2.18: An example of temperatures and pressure tradition during cooling down procedure for normal operation. The data were taken between Nov. 23, 2005 and Dec. 15, 2005.

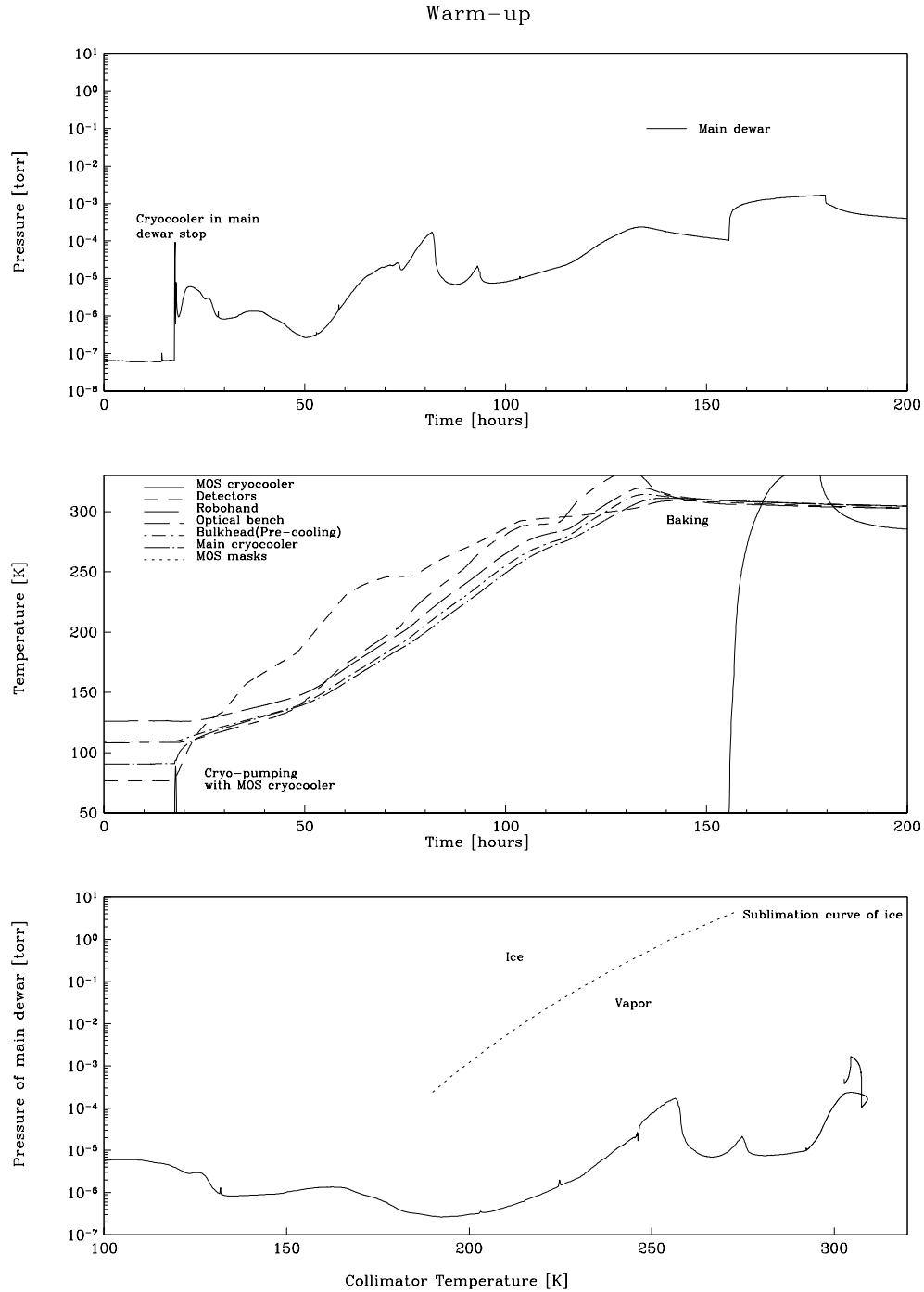


Figure 2.19: An example of temperatures and pressure tradition during warming-up procedure. The data were taken between Oct. 19, 2005 and Oct. 30, 2005 at the summit. The bottom panel shows temperature-pressure curve during warm-up. Dashed line shows sublimation line of ice.

## Chapter 3

# Cryogenic MOS System

The major challenges in developing a cryogenic multi-slit spectrograph are how to provide a new mask during the observation in a cryogenic environment and how to replace the stored masks without a thermal cycling the main dewar. We solved both these problems with the slit mask exchanger design described in this chapter. The slit masks themselves are described in the following section.

### 3.1 Mask Exchange System

#### 3.1.1 Slit Mask Exchanger

The 3-D schematic view of the mask exchanger is shown in Figure 3.1. The mask exchanger consists of a carousel, an arm with a mask catcher, and four robohands. The masks are held by the carousel. 19 masks are stored at once. The mask is gripped by the mask catcher and brought from the carousel to the focal plane of the telescope by the arm. At the focal plane, the mask is gripped with the four robohands.

In order to reduce the thermal radiation from the mask surface itself, the masks need to be cooled to 150K or below. The masks stored in the mask dewar are stucked to the carousel with magnets in order to keep strong coupling to the carousel for the cooling and not to slide out during observations. By rotating the carousel, one of the slots in the carousel is selected by the arm to pick up the mask. The carousel rotates by  $\pm 180^\circ$ . The mask dewar has its own vacuum pump and a Sumitomo cryocooler. The cryocooler cools the masks via the carousel and a heatpath. Since the heatpath is connected to the cold head, which is fixed to the mask dewar, and to the carousel, which rotate by  $\pm 180^\circ$  inside the dewar, the heatpath should be flexible. Oxygen-free high-conductivity (OFHC) copper straps are used for the heatpath, because OFHC material has high flexibility even under cryogenic environment. OFHC strap ( $W=38\text{ mm} \times L=300\text{ mm} \times t=0.15\text{ mm}$ ) with 30 layers is used. The number of the layers is determined to maximize the thermal conductivity without losing the flexibility for the  $\pm 180^\circ$  rotation.

On the contrary, the thermal transfer between the mask dewar and the carousel should be minimized. The carousel is supported by the spoke-wheels made of stainless steel in the dewar (Figure 3.2, 3.3). Because the wheels are very thin and stainless steel has a small thermal conductivity, the thermal transfer is reduced.

A mask in the carousel is selected by rotating the carousel. The carousel sits on bearings (KAYDON, Realslim Bearing KC050XPO) and is driven by a stepping motor, which is attached outside of the mask dewar, with a geneva gear mechanism. The geneva gear mechanism is shown in Figure 3.2. The geneva drive pin pushes the spoke-wheel to rotate the carousel. The angle of the carousel rotation and the home position are read by two limit switches attached below the carousel (Figure3.6).

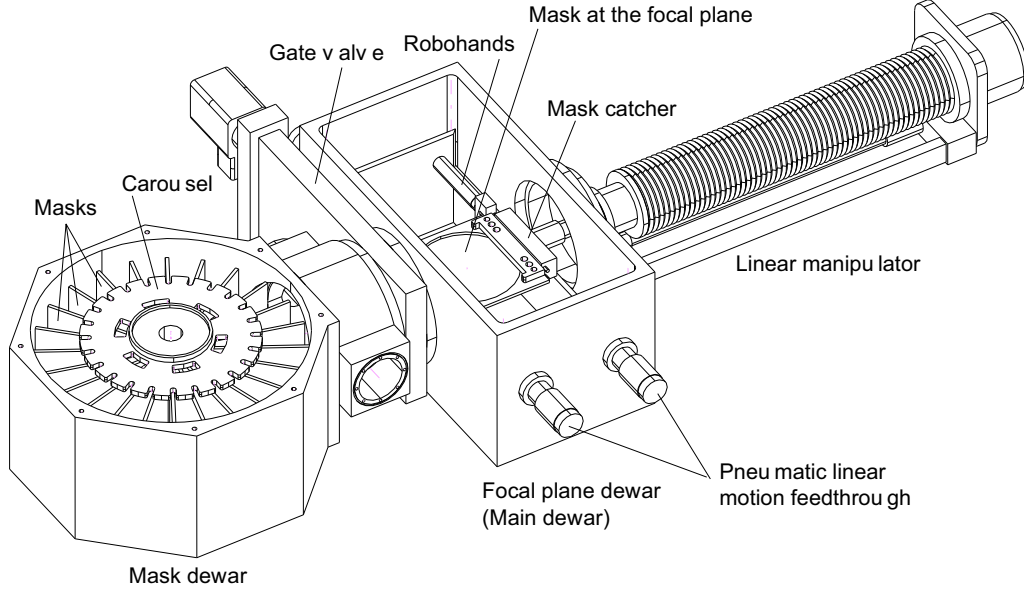


Figure 3.1: 3-D schematic view of the slit mask exchange system. The octagonal dewar at left is the mask dewar. The rectangular dewar at center is the focal plane dewar. The bellows at the right is the linear manipulator. A slit mask is held at the focal plane as in the figure.

The arm driven by a linear manipulator (Thermonics Vacuum Products, EMTX-1.87-20 / B8 / MD-Z) moves the mask between the main dewar and the mask dewar under a vacuum environment. The linear manipulator achieves the linear motion with high-precision under ultra-high vacuum environment. The combination of a stepping motor and sensors controls the arm motion. The mask is held by the mask catcher attached at the tip of the arm. A feedthrough (MDC, ALM-275-1) attached to the linear manipulator closes and opens the mask catcher. These feedthrough are driven pneumatically.

The mask is held at the focal plane by 4 robohands during observations. They are precision 2 jaw parallel grippers with low friction and excellent part-position repeatability. In order to operate the robohands at cryogenic condition, we de-grease the gears and bearings, because conventional lubricant such as oil or grease applied originally can not be used in the cryogenic condition. The grease was wiped away with acetone and the ultrasonic cleaner. In order to prevent the mask from dropping on to the optics below the focal plane, the mask holder has iron plates screwed on the edges, which stick to the magnets in the robohands and mask catcher.

We use a gate valve (MDC, LGV-8000V-P) between the two dewars to isolate the mask dewar from the main dewar during the mask replacement. The gate valve (MDC, LGV-8000V-P) has 203mm diameter aperture and is operated electro-pneumatically. This valve allows us to break the vacuum in the mask dewar without affecting that in the main dewar.

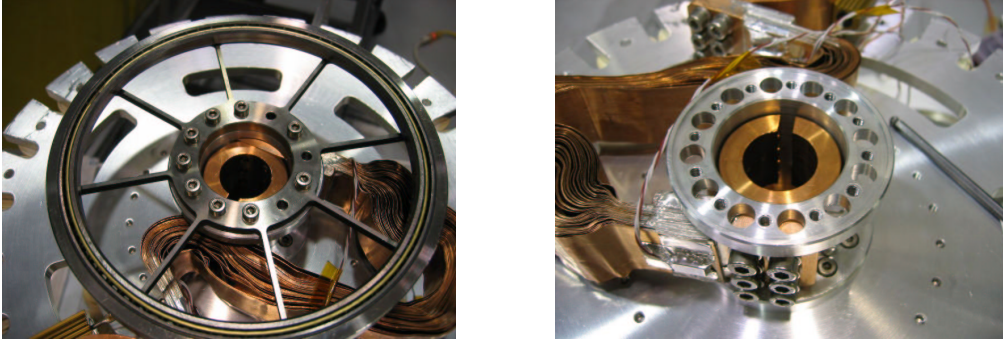


Figure 3.2: (Left) The spokewheel and bearing, the heatpath is shown under the spokewheel. The spokewheel is downward in the mask dewar. The geneva gear is seen in the bottom. (Right) The heatpath of copper straps. The copper shaft is also shown inside the carousel shaft.

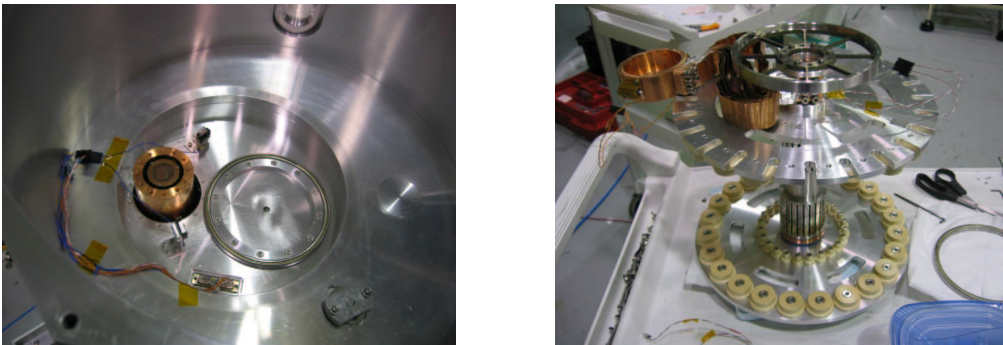


Figure 3.3: (Left) The bottom of the mask dewar. The coldhead, two limit sensors for carousel position control, geneva drive pin (lower left) are shown. (Right) Carousel shown upside-down. The spokewheel are attached to both ends of the shaft.

Table 3.1: The list of Sensors.

Place	#	Sense	Type
Gate valve	2	close/open	micro switch
Arm rotate	2	vertical/horizontal	photo micro sensor
Arm status	1	open/close	conductive switch
Robohand	4	close/open	proximity sensor
Arm position	4	exist/non-exist	proximity sensor
Mask position	2	vertical/horizontal	photo micro sensor
Carousel position	2	clockwise limit/counter-clockwise limit	micro switch
Air pressure	1	numerical	flow meter

### 3.1.2 Position Sensing

Eight sensors of different types monitor the mask exchange process in the system (Figure 3.4, 3.5, Table 3.1.2). An sample of the sensor is shown in Figure 3.6. The sensor consists of a round thin stainless steel strap, which works as a trigger, and the micro switch attached to the mask dewar. The sensor system monitors the rotation angle of the carousel. The most important point for the sensor system is to monitor the rotation in the both direction. It is achieved with the flexible round shape trigger.

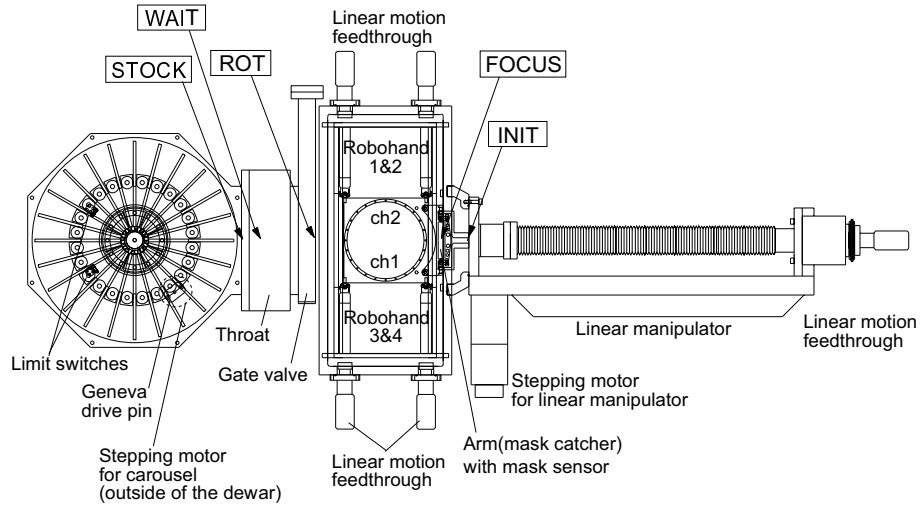


Figure 3.4: A top view of the mask exchanger. The positions monitored by the control software are indicated with frames. The locations of the position sensors are also shown.

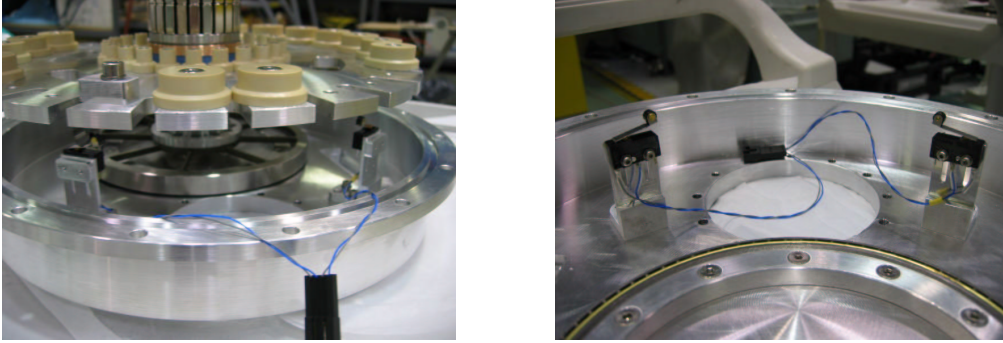


Figure 3.5: The bottom of the mask dewar. In the mask dewar, two micro switches limits rotation of the carousel. The carousel is not shown in the right picture for clarity.

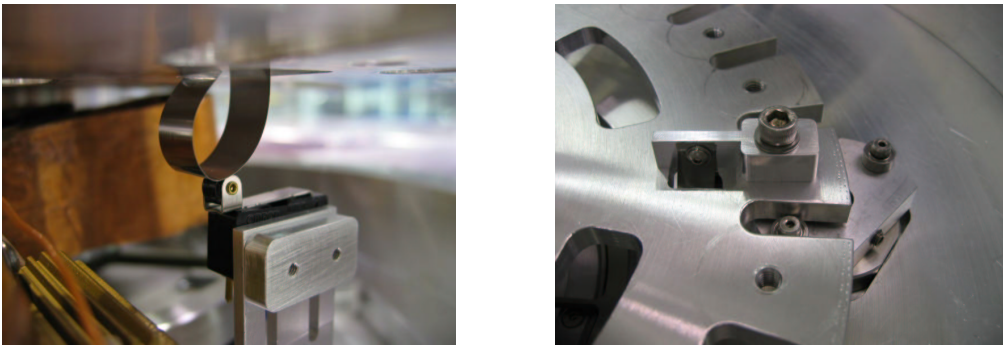


Figure 3.6: The micro switches and their actuator. The actuator (left) is made of thin stainless steel strap. Since it works as spring, the two-way actuation is available. This allows overrun of carousel in safety. The carousel rotation is mechanically limited by the heatpath length.

### 3.1.3 Mask Exchange Procedure

All the required movements during the mask exchange procedure are fulfilled by five fundamental sequences of actions: 1) The arm without a mask moves to the mask dewar from the initialized position (START). 2) The arm picks a mask from the carousel and fix it to the focal plane (LOAD). 3) The arm returns the mask from the focal plane back to the mask dewar (STORE). 4) The arm moves the mask out of the focal plane for a temporal imaging (FCHECK). 5) The arm goes back to the initial position. All motions for mask exchange are the combination of a few sequences of 1) to 5). The detailed breakdown of each sequence is as follows;

START (Go to the mask dewar to take a mask.)

- (1) Check if arm horizontal
- (2) Arm open
- (3) Robohands close
- (4) Arm goes to FOCAL position
- (5) Arm close
- (6) Robohands open
- (7) Arm goes to ROT position
- (8) Arm rotates to Vertical
- (9) Arm open
- (10) Arm reaches to the mask dewar (WAIT position)

LOAD (Load a mask onto the focal plane)

- (1) Arm rotate to vertical
- (2) Arm open
- (3) Arm moves to STOCK position
- (4) Arm close
- (5) Arm goes back to ROT position (Throat)
- (6) Arm rotates to Horizontal
- (7) Arm goes back to FOCUS position
- (8) Robohands close
- (9) Arm open
- (10) Arm goes to INIT position (Initialized)
- (11) Arm counter reset

STORE (Put a mask back to the mask dewar)

- (1) Check if arm horizontal
- (2) Arm open
- (3) Robohands close
- (4) Arm goes to FOCUS position
- (5) Arm close
- (6) Robohands open
- (7) Arm goes to ROT position
- (8) Arm rotates to Vertical
- (9) Arm goes to WAIT position
- (10) Arm open
- (11) Arm goes back to WAIT position



FCHECK (Step aside for field check during long time spectroscopy)

- (1) Check if arm horizontal
- (2) Arm open
- (3) Robohands close
- (4) Arm goes to FOCUS position
- (5) Arm close
- (6) Robohands open
- (7) Arm goes to ROT positon

FIN (Put a mask back to the mask dewar and finish spectroscopy)

- (1) Arm goes to ROT positon
- (2) Arm CLOSE
- (3) Arm rotates to horizontal
- (4) Arm goes back to INIT position
- (5) Robohands close
- (6) Arm counter reset

### 3.1.4 Interlock

Exchanging masks securely is important, especially under the cryogenic condition. For that purpose, macro commands, which conducts the above sequences with proper confirmations of interlock conditions are crucial. We developed the macro commands (Konishi et al. in preparation). Before conducting each step of the mask exchange procedures, the interlock software checks all of the status from the sensors relevant to the step. The interlock conditions for the each step of the sequences are summarized in Table 3.2. The conditions are taken into account in the macro commands which describes the sequences.

Thanks to the macro commands, the sequences can be conducted without human interruption. The mask exchange can be done within 4 minutes. The breakdown of the exchange time is shown in Table 3.3.

Table 3.2: Interlock macro sequences. '!OPEN' means 'not open'.

<b>START</b> Prepare grab mask	GV	Arm H-V	Arm O-C	Robohand	Arm position	Mask sensor	Carousel position	Air pressure
1, Arm ROTATE to horizontal	OPEN	-	-	-	INIT	-	OK	OK
2, Arm OPEN	OPEN	H	-	-	INIT	-	OK	OK
3, Robohand CLOSE	OPEN	H	OPEN	-	INIT	-	OK	OK
4, Arm move to FOCUS	OPEN	H	OPEN	!OPEN	INIT	-	OK	OK
5, Arm CLOSE	OPEN	H	OPEN	!OPEN	FOCUS	-	OK	OK
6, Robohand OPEN	OPEN	H	CLOSE	!OPEN	FOCUS	OFF	OK	OK
7, Arm MOVE to ROT	OPEN	H	CLOSE	OPEN	FOCUS	-	OK	OK
8, Arm ROTATE to vertical	OPEN	H	CLOSE	OPEN	ROT	-	OK	OK
9, Arm OPEN	OPEN	V	CLOSE	OPEN	ROT	-	OK	OK
10, Arm MOVE to WAIT	OPEN	V	OPEN	OPEN	ROT	-	OK	OK

<b>LOAD</b> Load mask onto FOCUS	GV	Arm H-V	Arm O-C	Robohand	Arm position	Mask sensor	Carousel position	Air pressure
1, Arm ROTATE to vertical	OPEN	-	-	-	WAIT	-	OK	OK
2, Arm OPEN	OPEN	V	-	-	WAIT	-	OK	OK
3, Robohand CLOSE	OPEN	V	OPEN	-	WAIT	-	OK	OK
4, Arm move to FOCUS	OPEN	V	OPEN	-	STOCK	ON	OK	OK
5, Arm CLOSE	OPEN	V	CLOSE	-	STOCK	-	OK	OK
6, Robohand OPEN	OPEN	V	CLOSE	-	ROT	-	OK	OK
7, Arm MOVE to ROT	OPEN	H	CLOSE	OPEN	ROT	-	OK	OK
8, Arm ROTATE to vertical	OPEN	H	CLOSE	OPEN	FOCUS	-	OK	OK
9, Arm OPEN	OPEN	H	CLOSE	!OPEN	FOCUS	ON	OK	OK
10, Arm MOVE to WAIT	OPEN	H	OPEN	!OPEN	FOCUS	-	OK	OK
11, Arm counter reset	-	-	-	-	INIT	-	-	-

<b>STORE</b> Store mask into carousel	GV	Arm H-V	Arm O-C	Robohand	Arm position	Mask sensor	Carousel position	Air pressure
1, Arm ROTATE to horizontal	OPEN	-	-	-	WAIT	-	OK	OK
2, Arm OPEN	OPEN	H	-	-	WAIT	-	OK	OK
3, Robohand CLOSE	OPEN	H	OPEN	-	WAIT	-	OK	OK
4, Arm move to FOCUS	OPEN	H	OPEN	!OPEN	STOCK	ON	OK	OK
5, Arm CLOSE	OPEN	H	OPEN	!OPEN	STOCK	-	OK	OK
6, Robohand OPEN	OPEN	H	CLOSE	!OPEN	ROT	-	OK	OK
7, Arm MOVE to ROT	OPEN	H	CLOSE	OPEN	ROT	-	OK	OK
8, Arm ROTATE to vertical	OPEN	H	CLOSE	OPEN	FOCUS	-	OK	OK
9, Arm move to STOCK	OPEN	V	CLOSE	OPEN	FOCUS	ON	OK	OK
10, Arm OPEN	OPEN	V	CLOSE	OPEN	FOCUS	-	OK	OK
11, Arm move to WAIT	-	V	OPEN	OPEN	INIT	-	-	-

<b>FCHECK</b> Unload mask temporarily	GV	Arm H-V	Arm O-C	Robohand	Arm position	Mask sensor	Carousel position	Air pressure
1, Arm ROTATE to horizontal	OPEN	-	-	!OPEN	INIT	-	OK	OK
2, Arm OPEN	OPEN	H	-	!OPEN	INIT	-	OK	OK
3, Robohand CLOSE	OPEN	H	OPEN	!OPEN	INIT	-	OK	OK
4, Arm move to FOCUS	OPEN	H	OPEN	!OPEN	INIT	-	OK	OK
5, Arm CLOSE	OPEN	H	OPEN	!OPEN	FOCUS	-	OK	OK
6, Robohand OPEN	OPEN	H	CLOSE	!OPEN	FOCUS	ON	OK	OK
7, Arm MOVE to ROT	OPEN	H	CLOSE	OPEN	FOCUS	-	OK	OK

<b>FIN</b> Finish Spectroscopy mode	GV	Arm H-V	Arm O-C	Robohand	Arm position	Mask sensor	Carousel position	Air pressure
1, Arm move to ROT	OPEN	-	-	!OPEN	INIT	-	OK	OK
2, Arm CLOSE	OPEN	H	-	!OPEN	INIT	-	OK	OK
3, Arm ROTATE to horizontal	OPEN	H	OPEN	!OPEN	INIT	-	OK	OK
4, Arm move to INIT	OPEN	H	OPEN	!OPEN	INIT	-	OK	OK
5, Robohand CLOSE	OPEN	H	OPEN	!OPEN	FOCUS	-	OK	OK
6, Arm counter reset	OPEN	H	CLOSE	!OPEN	FOCUS	ON	OK	OK

Table 3.3: The time required for each exchange macro command as of Dec. 2005.

For first mask install	3m 45s
go to take a mask	1m 45s
set a mask	2m 00s
Mask exchange	4m 00s
put back a mask	1m 58s
set a mask	2m 00s
Step aside for field check	2m 15s
step aside	1m 06s
back to focal plane	1m 08s
Finish	3m 35s
put back a mask	1m 58s
go back initialize positon	1m 35s

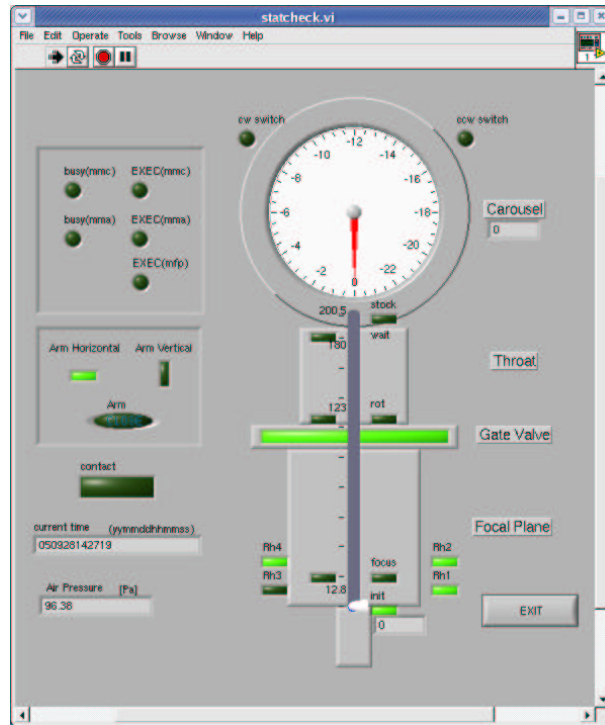


Figure 3.7: LabVIEW VI (virtual instrument) display for MOS control (Konishi et al. in preparation). Sensor buttons turn red if abnormal situation is detected.

## 3.2 Slit Mask

### 3.2.1 The Selection of the Mask Material

In order to keep the thermal radiation from the mask surface well below the background radiation from the sky, it is required to cool masks below 150K. For fast replacement of the mask set, the masks should be cooled as soon as possible. In addition, the mask material is required to have a good thermal conductivity for uniform temperature distribution.

To examine the cooling down properties, We performed cooling tests for three candidates materials of slit masks, aluminum, invar, and carbon sheets. The materials are chosen because aluminum has good thermal conductivity and good machinability, invar has small coefficient of thermal expansion, and carbon sheet is used for the masks of the Faint Object Camera And Spectrograph (FOCAS). The cooling tests are conducted using the mask dewar, the carousel system and the cryocooler. The results are shown in Table 3.5. Only aluminum can be cooled down below 150K within 3 hours. Based on the results, we choose aluminum foil for a mask material.

A sample of a mask set in the mask frame and the mask catcher is shown in the left picture of Figure 3.8. In the right picture shows an enlarged view of a slit. The mask is made from hard-temper aluminum foil of 180mm diameter with  $75\mu\text{m}$  (0.03 inches) thickness.

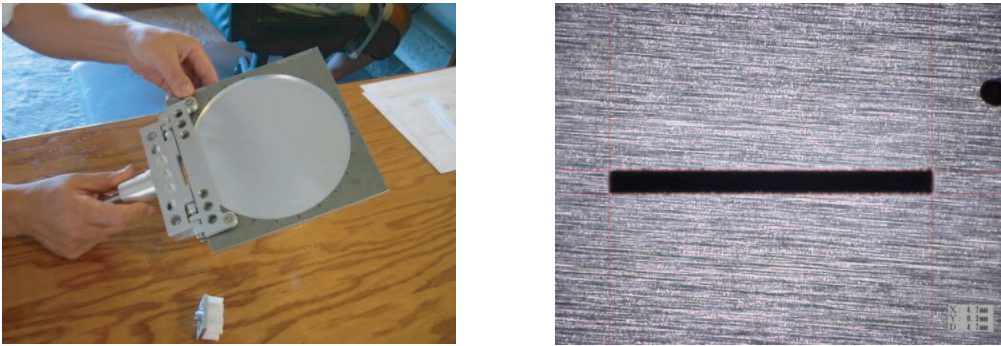


Figure 3.8: (Left) A mask with the maskframe and arm(mask catcher). (Right) The enlarged view of slit cut ( $300\mu\text{m} \times 4.7\text{ mm}$  slits), which corresponds to  $0.6''$  slit at the Subaru focus.

Table 3.4: Properties of the candidates for mask materials.

material	Density [kg/m <sup>3</sup> ]	Conductivity [W/m/K]	CTE [1/K]	Specific Heat [J/kg/J]
Aluminum	$2.8 \times 10^3$	90	15.9	600
Invar	$8.05 \times 10^3$	13.8	0.1	502
Carbon sheet (FOCAS mask)	$1.76 \times 10^3$	-	0.9 (0°) - (90°)	-

Table 3.5: The results of cooling tests for different materials. The mask was attached direct to the coldhead. The temperatures were measured at the center of each masks. The diameter of each masks is 180 mm.

material	0 hour	1 hour	2 hour	3 hour
Aluminum ( $t=75\mu\text{m}$ )	291.8	143.9	69.9	70.4
Invar ( $t=50\mu$ )	293.4	261.7	248.4	247.6
Carbon sheet ( $t=100\mu\text{m}$ )	291.6	278.0	278.2	277.8
Coldhead	-	-	-	<50.0

### 3.2.2 Thermal Contraction of the Masks

In order to make MOS masks for the MOIRCS, it is fundamental to know the plate scale of the Cassegrain focus and the thermal contraction factor of the mask when it is cooled down to 150K. It is known that the distortion of the focal plane at the Cassegrain focus is negligible in  $\phi 6'$  field (Kashikawa et al. (2002)). In order to set the slits with  $0''.1$  accuracy in the  $6'$  field of view, the plate scale and the thermal contraction factor should be determined within 0.02% accuracy. The plate scale at the Cassegrain focus has been already accurately measured to be  $2.06218 \text{ arcsec mm}^{-1}$ . We examine the thermal contraction factor of the mask. ( In addition, if the targets are selected from a pre-imaging data taken with MOIRCS, the distribution of the data should be corrected. The details of designing of the masks with the pre-imaging data are discussed in the following section.)

Using pinhole masks and sky imaging data obtained with MOIRCS, we examined the thermal contraction factor. The important points are whether the thermal contraction is uniform or not, and whether the thermal contraction factor is constant among different masks and different cooling down run. The procedure is summarized in Figure 3.9. First, we prepare a distortion corrected and mosaiced sky image of several fields. We use fields which contain many stars, like globular cluster M15. Pinholes are put at the position of stars in the images. Only plate scale at the Cassegrain focus is considered, and no contraction factor is applied for the experiment. The pinhole masks are cooled in the mask dewar, installed to the focal plane, and imaged with the MOIRCS without dispersing elements. The images are obtained after 90 hours of cooling in the mask dewar. The images are corrected for distortion- and mosaiced in the same way for the sky images. Finally the positions of the pinhole images are compared with the positions of stars in the sky images. The thermal contraction factor can be directly calculated by the comparison.

The results are summarized in Table 3.6. The data were obtained on Aug.11 (sky images) and on Sep. 26, 2005 (mask images). The thermal contraction factor distributes around the average value of 1.0061 with peak-to-peak difference of  $\pm 0.0002$ , which is within the required specification (0.02%). The contraction is uniform and there is no significant residual after correcting the thermal contraction factor.

The time variation of the thermal contraction factor after the mask installation is also measured. The results are shown in Figure 3.10. After about 100 hours of cooling, the contraction of the mask stops. For most of the masks, at least 60 hours of cooling is required to reach the contraction factor of  $1.0061 \pm 0.0002$ .

It is observed that the thermal contraction factor also changes at the focal plane. When the mask is at the focal plane, it is warmed by the thermal radiation through the MOIRCS window. The changes are shown in Figure 3.11. The variation is large in the first 30min, but slow down later. The MOS acquisition procedure itself takes about 30min currently. Therefore the initial contraction is settled during MOS acquisition sequence.

Table 3.6: The measured contraction factors for the data on Aug. 11, 2005 for the sky image, and on Sep. 26, 2005 for mask image after 90 hours of cooling.

Mask	Contraction factor
M15	1.006116
M42	1.005874
M31(1)	1.006212
M31(2)	1.006238
SSA22(1)	1.006044
SSA22(2)	1.005934
Average	1.006070

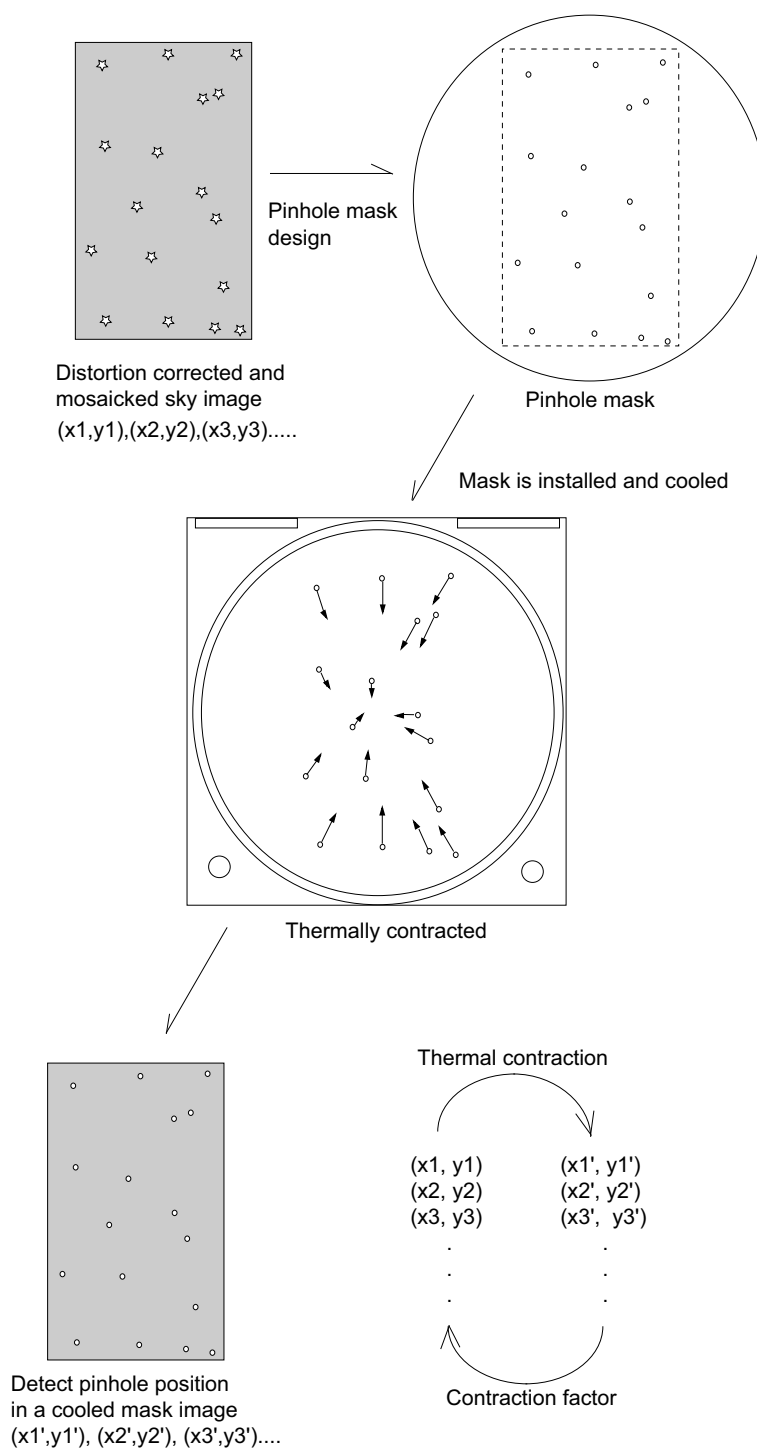


Figure 3.9: The method of the thermal contraction factor.



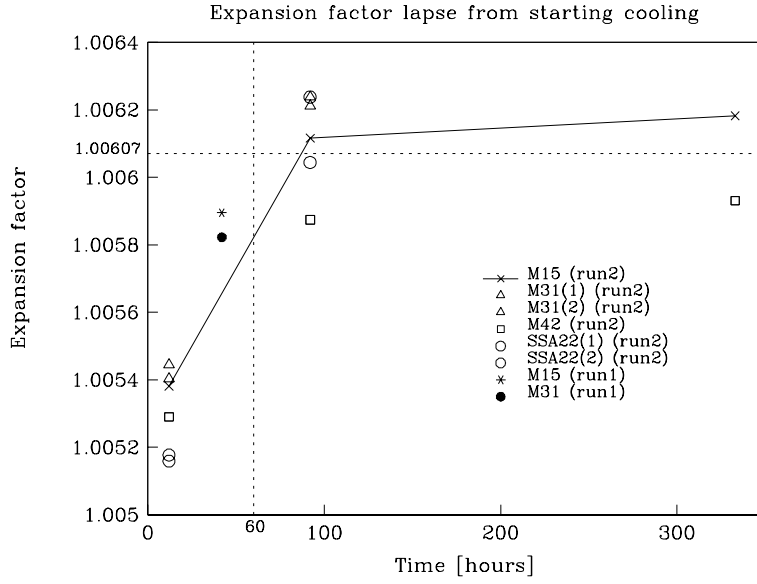


Figure 3.10: The variation of the contraction factor with time after cooling the mask dewar. It approaches to the constant in about 60 hours from starting cooling the mask dewar.

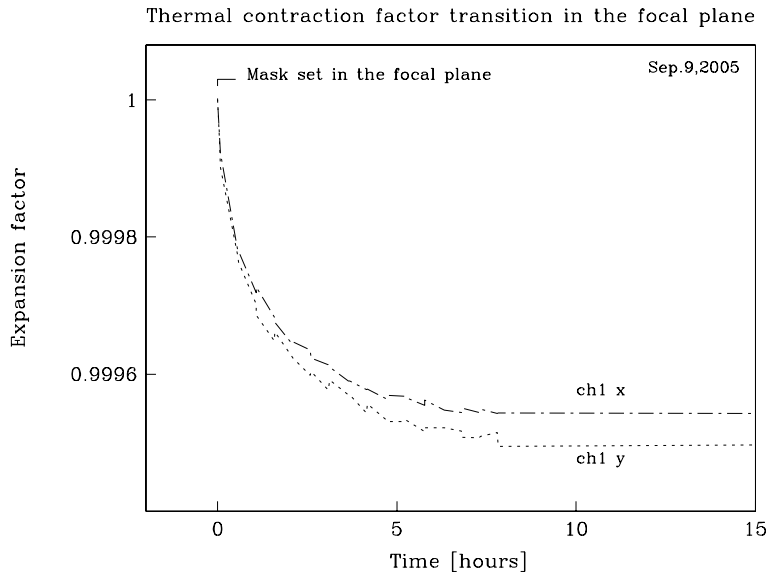


Figure 3.11: The decrease of the contraction factor with time after the mask is set at the focal plane. It decreases about 0.04 % (corresponding to 1.6 pixel ( $0''.2$ )) for the first 3 hours.

### 3.2.3 Slit Design

In order to design slit masks, we use the Mask Design Program (MDP) for FOCAS. Before starting mask design with MDP, we prepare a pre-image which matches the plate scale and the direction of the FOCAS images. The procedure is as follows;

- 1 Preparing pre-images.  
(Images of MOIRCS, FOCAS, Suprime-Cam are applicable.)
- 2 Distortion correction and mosaicing.  
(flattening, subtracting, stacking ... if necessary)
- 3 Flip image against Y axis for MOIRCS and Suprime-Cam images
- 4 Magnify images to match plate scale of  $0.''1038 \text{ pixel}^{-1}$

The details of the distortion correction and mosaicing is discussed in Suzuki (2006). It should be noted that the distortion pattern at the detector is changed with changing position of the detector to adjust the camera focus (z-direction movement). Therefore, we have to measure the distortion pattern whenever the detector position is changed. The distortion pattern can be measured with images of stars at the fields where FOCAS or Suprime-Cam images are also available. It should be noted that, the images taken by MOIRCS and Suprime-Cam is 'look up sky' image while the laser cutting is done based on 'look down from sky' image. Therefore we need to flip the images for MOIRCS and Suprime-Cam cases.

- 6 Set the center coordinate of the mask.  
(We can change the mask center position later.)
- 7 Design of alignment holes.  
(We need three - five stars for each detectors... for the moment.)
- 8 Design of slits.  
(One slit per one dispersion direction for zJ500 and HK500 grisms.)
- 9 Save the slits positions to \*.mdp file (x,y pixel).
- 10 Transform [x pix,y pix] to [x mm, y mm] with \*.sbr file.  
(\*.sbr file is used for laser slit cutting.)

The thermal contraction factor (1.0061) discussed in the previous section is applied to the "sbr" file as follows;

- 11 Multiply [x mm, y mm] of \*.sbr by the contraction factor.
- 12 Multiply the width of the slits by the laser machining factor.  
(The details about the laser machining factor are described just after this.)
- 13 Start mask cutting. (It takes 2-4 hours per mask to be cut.)

The width of the slit made by the laser cutter is slightly different from the input values. We examine the relation between the original parameters and measured widths. We made several slits with various widths and measured the fabricated width with microscope. The results are shown in Figure 3.12 and summarized in Table 3.7. The difference should be considered in the mask design. The minimum slit width is about  $145 \mu\text{m}$ , which corresponds to  $0.''3$  at the Subaru focal plane. The minimum width is limited by the size of the laser spot.

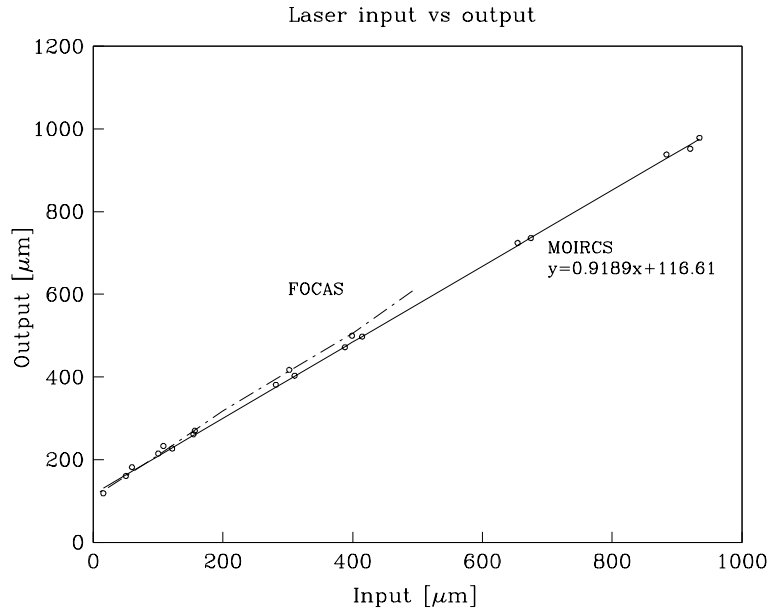


Figure 3.12: The fabricated slit width by the laser cutter vs. their original parameters. The relation depends on the distance from the focal plane of a laser beam.

### 3.2.4 Slit Cutting

Slits are cut with the YAG laser cutter, which is used for FOCAS mask cutting. More than 50 slits can be placed on a slit mask at once. The effect of the thermal contraction during the cutting and optical distortion of the laser system is corrected by software.

The maximum power of the laser is achieved at the focal plane of the laser beam. Therefore, if the height position of the mask is shifted a few ten  $\mu\text{m}$ , the power of the laser become faint and the width of the beam become wider.

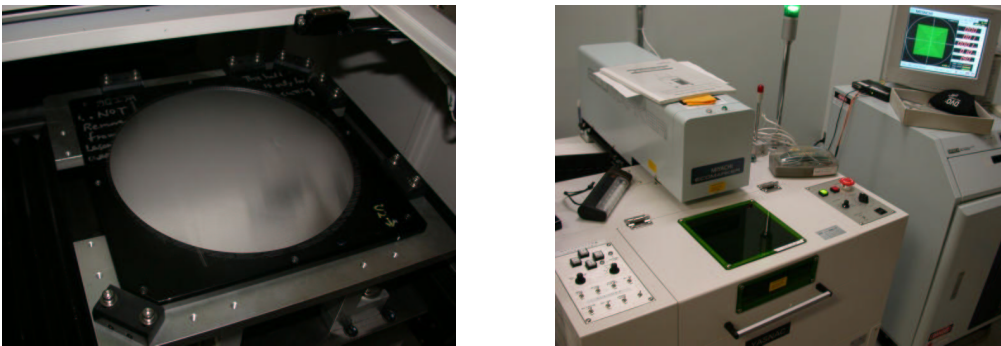


Figure 3.13: Laser cutting.

Table 3.7: Input value for the laser cutter. The effective scale at the Cassegrain focal plane is 2.06218 arcsec  $\text{mm}^{-1}$ .

Slit width [arcsec]	Cass scale (2'.06218/mm) [mm]	Contraction factor $\times 1.006070$	<b>Input to laser</b> (out)=0.9189*(in)+116.61 [mm]
0.3	0.145477	0.146350	0.032365
0.5	0.242462	0.243917	0.138542
0.7	0.339447	0.341483	0.244720
0.8	0.387939	0.390267	0.297809
1.0	0.484924	0.487833	0.403987
1.2	0.581908	0.585400	0.510164
1.5	0.727386	0.731750	0.669431
2.0	0.969847	0.975667	0.934875

### 3.2.5 Mask Installation

The aluminum foil mask is set in the maskframe and stored in the carousel. The maskframe is shown in Figure 3.14. Setting the masks onto the maskframe should be done carefully for the direction. Iron plates at the edges can be used to determine the direction. The masks are set into the frame before the laser cutting. The maskframe is hold by a laser cutting frame and set to the laser cutting machine.

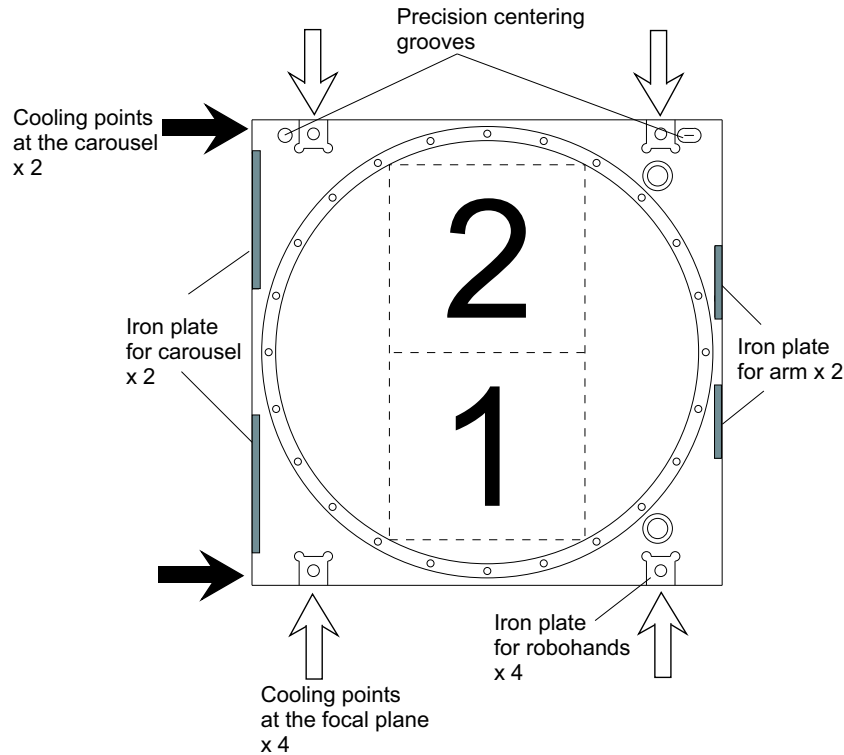


Figure 3.14: Mask frame layout. Several iron plates are screwed at the edges. The magnets set in the robohands and the arm pull the iron plate and prevent the mask from dropping on the optics below.

Replacement of masks is hands-on work at the telescope dome.

- (1) Check if the current pressure and temperature inside the mask dewar.  
Pressure > 760 torr. Temperature > 280 K.
- (2) Check if the gate valve CLOSE.
- (3) Prepare the mask replacing tool software **MaskInstall.vi**
- (4) Open the small door in the mask dewar.
- (5) Take the old masks and put the new ones.  
Direction as shown Figure3.15.
- (6) Reconfirm the masks to be in correct slots.
- (7) Close the door.
- (8) Start pumping the mask dewar.
- (9) Start cooling if the pressure becomes <  $10^{-4}$  torr.  
(It takes 30-60 min to reach.)

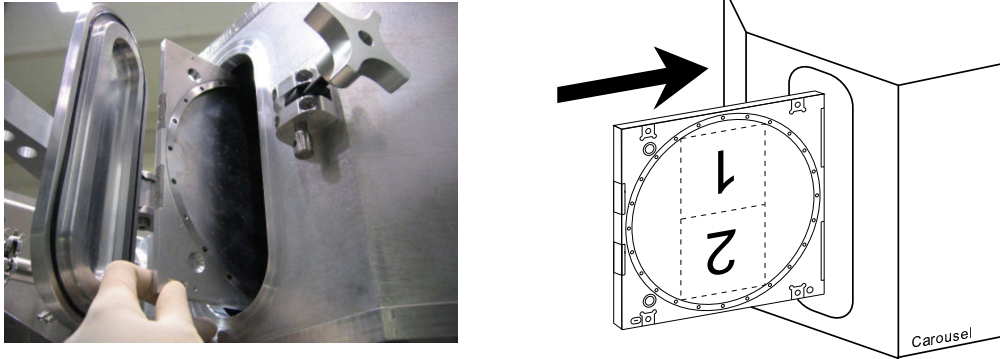


Figure 3.15: The mask replacement. Insert a mask with utmost care for its direction.

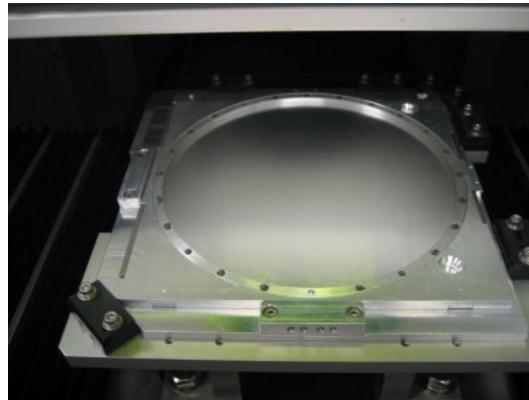


Figure 3.16: The laser cutting frame for MOIRCS own in preparation. The masks will be preset in the maskframe before laser cutting.

For replacing the masks, we need 2 days at this moment. The time is dominated by the time required to warming-up and cooling-down the masks. The typical time for each procedure is as follows.

Preimage acquisition	properly
Warm-up the masks	7 hours
Mask design	1-2 hours/mask
Mask cutting	4 hours/mask
Open the mask dewar and install the masks	0.5 hour
Pumping the mask dewar	0.5-1 hours
Cooling masks	at least 60 hours

## Chapter 4

# MOS Observation

The fundamental idea of the acquisition of target objects is to iterate taking sky images through alignment holes on mask until positional difference between acquisition alignment stars and the guiding holes become small enough.

### 4.1 MOS Pointing

#### 4.1.1 Pointing Sequence

The MOS pointing sequence for the MOIRCS is the same in general as for the optical MOS instrument. The sequence is shown in Figure 4.1. At the start, we move the telescope to the target field, start guiding, and take the image of the field without a slit mask. Next, we install a mask and take a image of the mask. The position of the alignment stars and the guide holes on the masks are measured from the images. Based on the difference, the telescope is moved to the proper position. The alignment stars will be caught in the guiding holes. The star positions are measured again in the guiding holes. According to the offset of the stars in the guiding holes, the telescope is moved again and/or MOIRCS is rotated, so that the stars come to the hole center. The iteration continues until the stars are centered at the holes with a certain accuracy.

Typical magnitudes of the alignment stars are supposed to be  $K < 18$  mag. In fields at high galactic latitudes, the number of bright stars is usually limited, and only faint alignment stars are available. Because the detection limit of near-infrared observations is generally shallower than optical observations due to high background noise, we need to take two images with dithering to detect the faint alignment stars. For example, we take two images A and B slightly different position, and subtract A from B. The subtracted image is used to find the faint stars for the pointing. The detailed pointing sequence in a typical high galactic latitude field is shown in Table 4.1. Currently about 30 min is required to finish the pointing sequence.

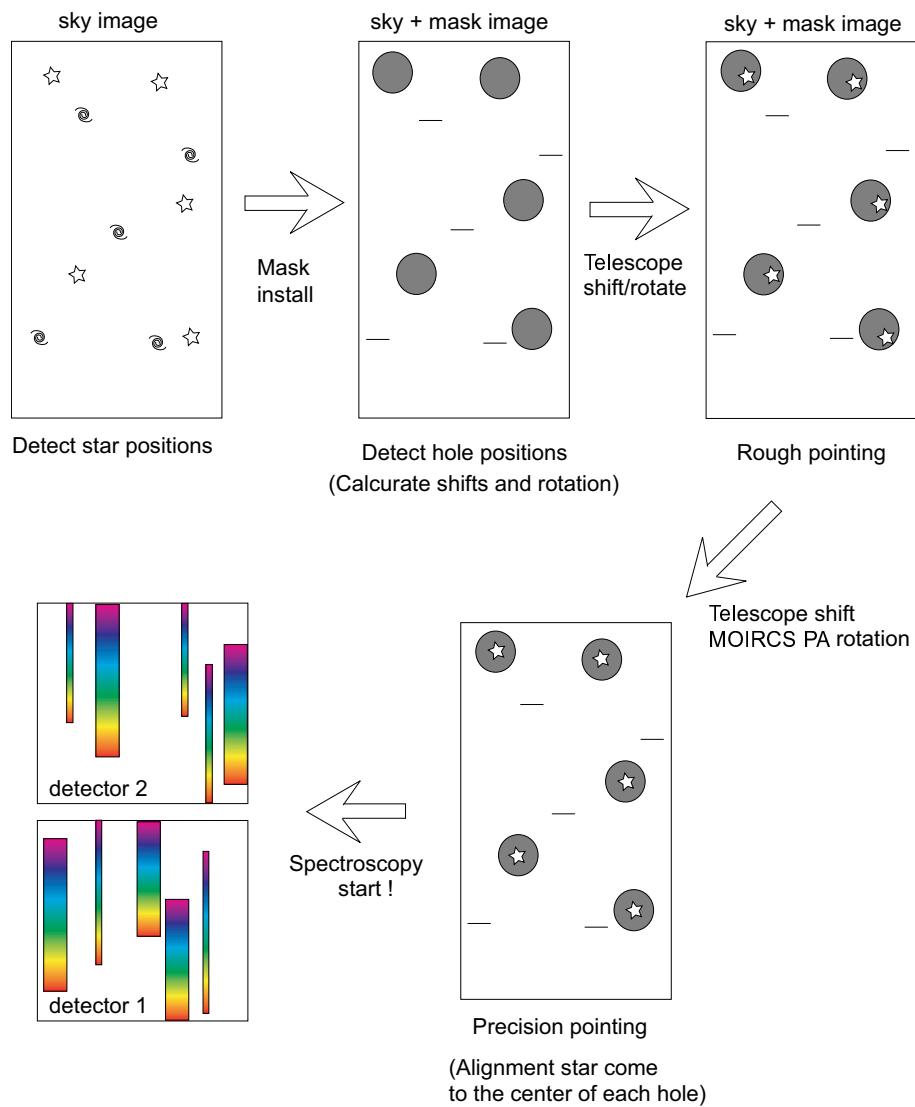


Figure 4.1: The sequence of the MOS pointing.



Table 4.1: Pointing sequences tested at the test observations on Oct. 12-13, 2005.

Step	Action	Time
1	SetupField	$\sim 5.0$ min
2	Exposure sky image (sky1.fits and sky2.fits with dithering)	4.4 min
3	SetupMOS:	(3.0 min)
	Mask install	5.0 min
	Distortion correction and mosaicing	(3.4 min)
	Subtraction (sky1.fits - sky2.fits)	(0.1 min)
	Detection of alignment stars	(0.7 min)
4	Re-setupfield	$\sim 3$ min
5	Exposure mask image (mask1.fits)	2.0 min
6	Distortion correction and mosaicing	1.7 min
7	Detection of hole positions	0.7 min
8	Combine data	0.1 min
9	GEOMAP fitting	0.1 min
10	Calculation of shift and rotation	0.1 min
11	Correction of rotation (Instrument PA)	0.5 min
12	Correction of shift (Telescope Offset)	0.5 min
13	Exposure mask image (mask2.fits)	2.0 min
14	Distortion correction and mosaicing	1.7 min
15	Subtraction (mask2.fits - mask1.fits)	0.1 min
16	Detect alignment stars inside alignment holes	0.7 min
17	GEOMAP fitting	0.1 min
18	Calculation of shift and rotation	0.1 min
19	Correction of rotation (PA)	0.5 min
20	Correction of shift	0.5 min
21	Exposure mask image (mask3.fits)	2.0 min
22	Distortion correction and mosaicing	1.7 min
23	Subtraction (mask3.fits - mask1.fits)	0.1 min
24	Detect alignment stars inside alignment holes	0.7 min
25	GEOMAP fitting	0.1 min
26	Calculation of shift and rotation	0.1 min
27	Check the residual of positions between stars and holes	0.1 min
28	If residual small enough, start spectroscopy	-
	If residual large, repeat step (19)-(26)	(5.0 min $\times\alpha$ )
total		34.0 min

### 4.1.2 Pointing Results

Thanks to the good pointing accuracy of the telescope, currently only a few iterations are required to reach a required accuracy ( $\sim 0.''1$ ), which is much smaller than the typical slit width for MOS observation,  $0.''8$ . The results of the 6 pointing sequences in various fields are shown in Table 4.2. The data were taken in Oct. 2005 and Dec. 2005. The fields cover various types of regions: bright globular cluster, M15, faint star cluster, M31, deep survey region, and Subaru/XMM-Newton Deep Field (SXDF).

The first line for each field represents the residual just after the telescope pointing and the mask installation. In the first iteration, the rotation of the mask is also corrected with changing the position angle (PA) of the instrument. The PA is changed without losing the telescope guiding. (The sequence is developed by Tomohiro Yoshikawa.) The residual usually reduced to less than  $1''$  after the first iteration. After two or three subsequent iterations, the residuals reach the required accuracy ( $\sim 0.''1$ ) then the spectroscopic observation is started. The residuals after the final iteration are shown in “x rms residual” and “y rms residual”. These values only represent systematic residual after the iterations. The random residuals are not included in the value. They are discussed in the next section.

Table 4.2: The pointing results. In most cases, at least three iterations were done until the fitting residual is smaller than 0.1 arcsec.

Iteration	Rotation [degree]	x shift [arcsec]	y shift [arcsec]	x rms residual [arcsec]	y rms residual [arcsec]
M15 Oct.12,2005					
1	0.6159	3.710	-1.9519	—	—
2	-0.0046	0.3274	0.3550	—	—
3	-0.0002	-0.08796	0.108523	0.1094	0.0702
M31 Oct.12,2005					
1	0.1157	4.2771	-4.4372	—	—
2	0.0158	-0.28178	-0.052	—	—
3	0.02647	0.0806	0.1104	0.1104	0.0396
SXDF Oct.12,2005					
1	0.7060	15.5898	0.6070	—	—
2	-0.0354	0.4875	-0.7045	—	—
3	0.0015	-0.1012	0.0304	—	—
4	0.0066	0.0126	0.0366	0.0619	0.0918
SXDF Oct.13,2005					
1	0.6523	13.932	0.291	—	—
2	-0.0022	-0.463	-0.531	—	—
3	-0.0099	-0.031	-0.031	0.0998	0.0845
M42 Dec.10,2005					
1	1.4787	6.730	-0.809	—	—
2	0.0046	0.091	-0.001	—	—
3	0.0119	0.045	0.254	0.0304	0.1012
SXDF Dec.11,2005					
1	-0.1213	16.934	-3.817	—	—
2	0.0110	-0.234	-0.674	—	—
3	0.0039	-0.065	-0.042	0.1291	0.1152

### 4.1.3 Random Residual

Even after the final iteration, there are not only the systematic residuals explained by shift, rotation, and magnification, but also random residuals. The random residuals come from various reasons; e.g. non-uniformity of the thermal contraction of the masks, uncertainty of the distortion correction for the mask-design image, error of the slit position due to the mask cutting system, etc. In order to examine the amount of the random residual, we compare the pinhole masks and the target sky field. The pinhole masks with no slits were used. The same method in Figure 3.9 is applied. We calculate a fitting residuals with sky images and cooled mask images. The actual star positions of the sky image and the pinhole positions of the cooled mask images are fitted with using **geomap** task of the IRAF package. In the fitting, only shift, rotation, and magnification are considered. The geomap computes the transformation from the input coordinate system to the reference coordinate system. The residual of the fitting in the three test fields are shown in Table 4.3 and the residual distribution of the pinhole positions after fitting are shown in Figure 4.2. The field images were obtained on Aug. 11-13, 2005 and the pinhole mask images were taken on Sep. 26, 2005. The RMS residuals are about 0.03-0.04 arcsec in one directions and 0.05 arcsec in both direction. The random residuals are sufficiently small. Note that the residuals do not depend on the number of holes, which means that the number of pinholes does not affect the uniformity of the thermal contraction of the masks.

Table 4.3: The residual of the fitting in the three test fields. The random residuals are sufficiently small. The residuals do not depend on the number of holes.

Object	Number of pinholes	Magnification	Residual(x) [arcsec]	Residual(y) [arcsec]
M15	40	1.006116	0.0338	0.0400
M42	28	1.005874	0.0322	0.0411
M31	32	1.006212	0.0431	0.0430

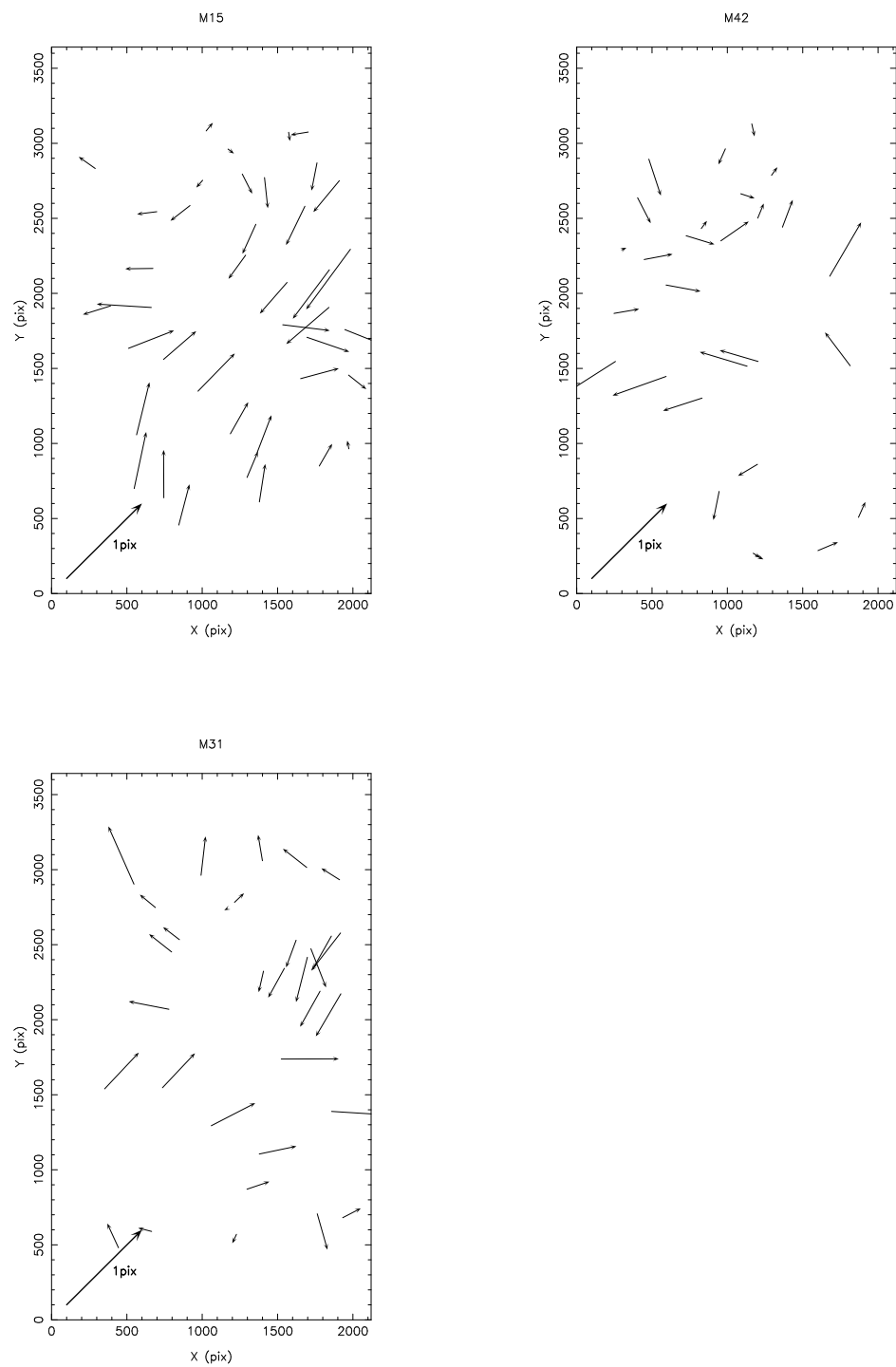


Figure 4.2: The residual of pinhole positions after correcting shift, rotation, and magnification in the three test fields. 1 pix is corresponding to  $0''.117$ .

## 4.2 Spectroscopic Capability

### 4.2.1 Resolution

MOIRCS has two pairs of gratings for spectroscopic observations; “zJ500” grism optimized for the  $z$  and  $J$ -band and “HK500” grism optimized for the  $H$  and  $K$ -bands observations. Both of the gratings are designed to have the spectral resolution of  $R \sim 500$  in the first order. The spectral efficiency of the gratings provided by Richardson Gratings are shown in Figure 4.3.

The spectral resolution of the gratings are measured with a long-slit spectroscopic observation of night sky emission lines with  $0.''3$  slits. The data were obtained with 600s integration on December 10 and 11, 2005. The spectral resolutions were measured with isolated night sky emission lines selected from the OH-emission line atlas Rousselot et al. (2000). The resulting Full-Width at Half Maximums (FWHMs) are shown in Figure 4.4. The average spectral resolutions with  $0.''3$  slit are  $11.9\text{\AA}$  and  $13.8\text{\AA}$  for zJ and HK gratings, respectively.

Using the same data set, the spectral dispersion of the gratings are measured. At first, the night sky emission lines in the data are identified with the OH-emission lines in Rousselot et al. (2000). The results are shown in Figure 4.6 and 4.7, for zJ500 and HK500 respectively. For the zJ500 observation, no filter was used, and for the HK500 observation,  $1.3\mu\text{m}$  order-cut filter (OC1.3) was used. The wavelengths and the pixel coordinates are fitted with polynomial function using **identify** task in IRAF. The wavelengths are well fitted with 3rd order polynomial for both of the gratings with the rms residual of 0.5 pixel. The fitting results are shown in Figure 4.5. Wavelength  $\lambda(\text{\AA})$  of pixel position  $x(\text{pixel})$  is described with  $\lambda = 9 \times 10^{-8}x^3 - 0.0001x^2 - 5.57x + 17216$  (zJ500) and  $\lambda = 1 \times 10^{-7}x^3 - 0.0003x^2 - 7.72x + 27710$  (HK500). The results indicate that the dispersions are  $5.57 \text{ \AA pixel}^{-1}$  for the zJ500 grism and  $7.72 \text{ \AA pixels}^{-1}$  for the HK500 grism in the first order. It should be noted that the zJ500 grism can cover the  $H$ -band though the efficiency will be lower than the HK500 grism in the  $H$ -band.

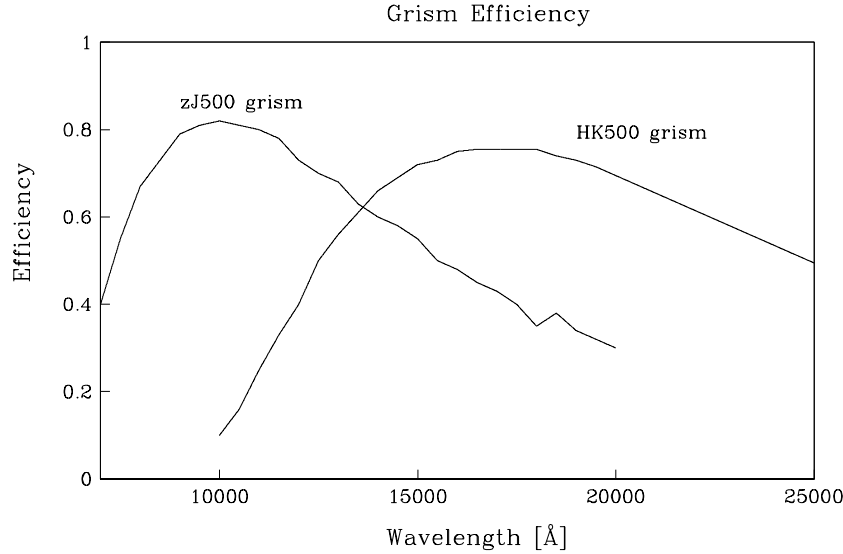


Figure 4.3: The efficiencies of zJ500 and HK500 gratings.

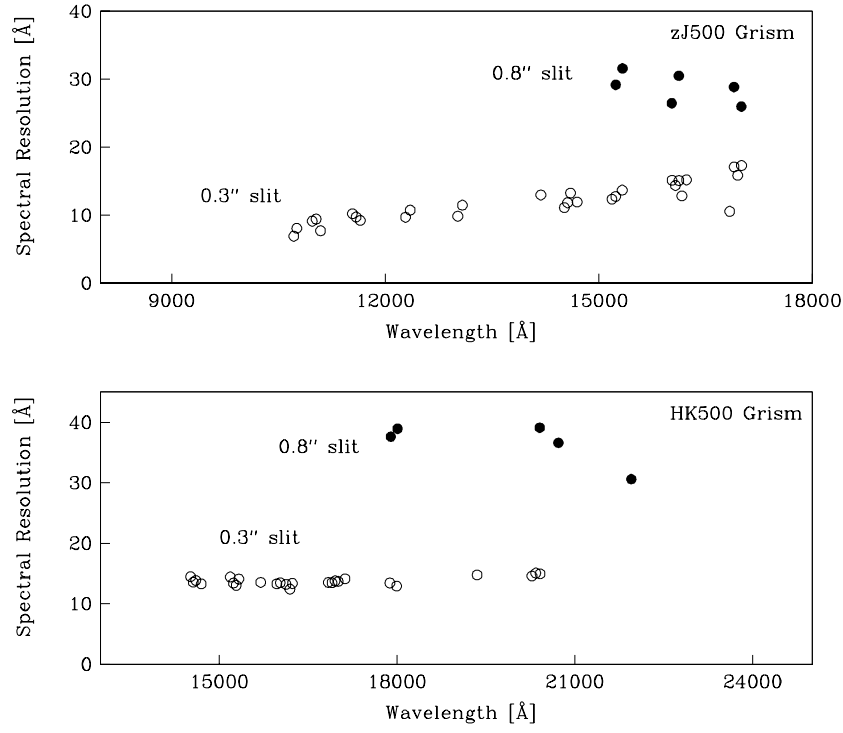


Figure 4.4: The spectral resolutions of zJ500 and HK500 grisms. The isolated night-sky emission line widths were measured.

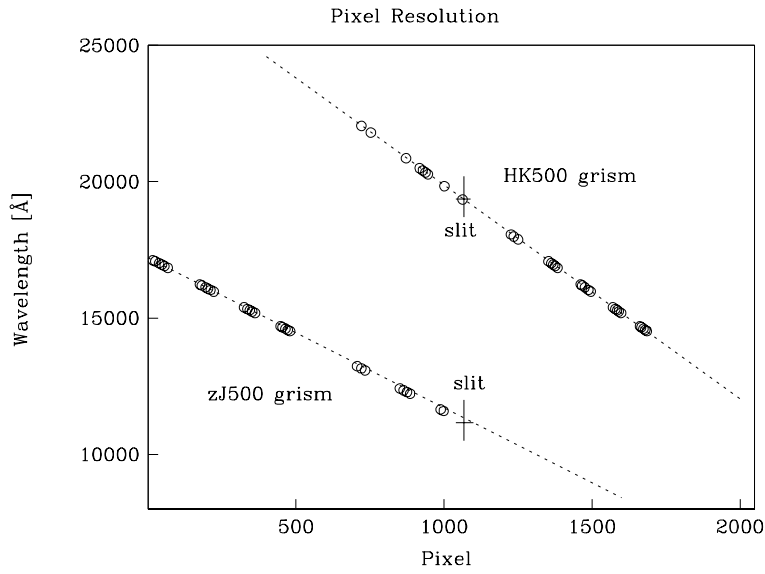


Figure 4.5: The fitting results of the wavelength and the pixel coordinates. The wavelengths are well fitted with 3rd order polynomial for both grisms.

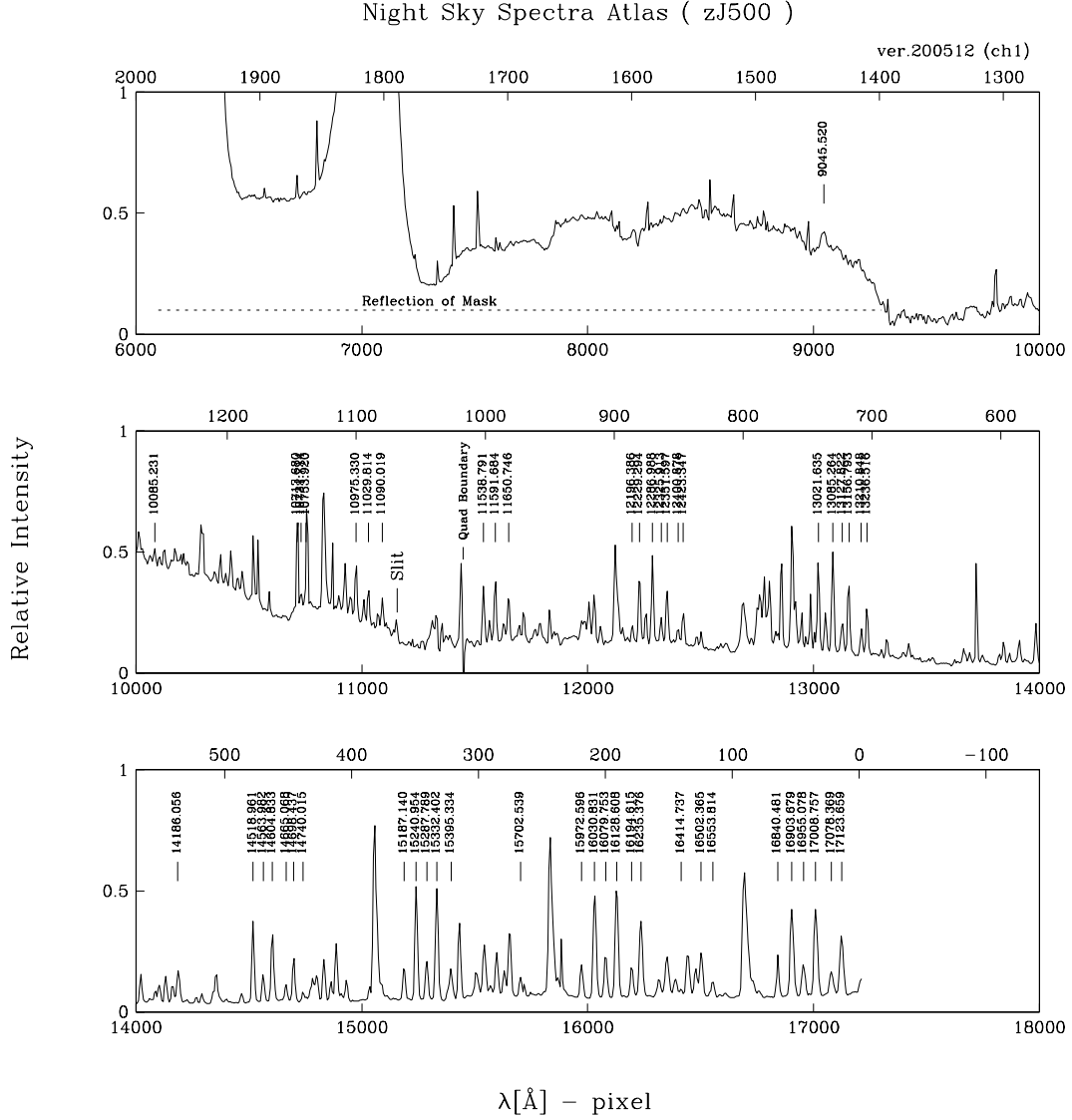


Figure 4.6: OH Night-sky spectra for  $zJ$ -band. The slit is at  $11807 \text{ \AA}$  (1067 pixel). The  $zJ$ -band spectroscopy was used without filters. The stray light is reflected at the wavelength range shorter than  $10000 \text{ \AA}$ .



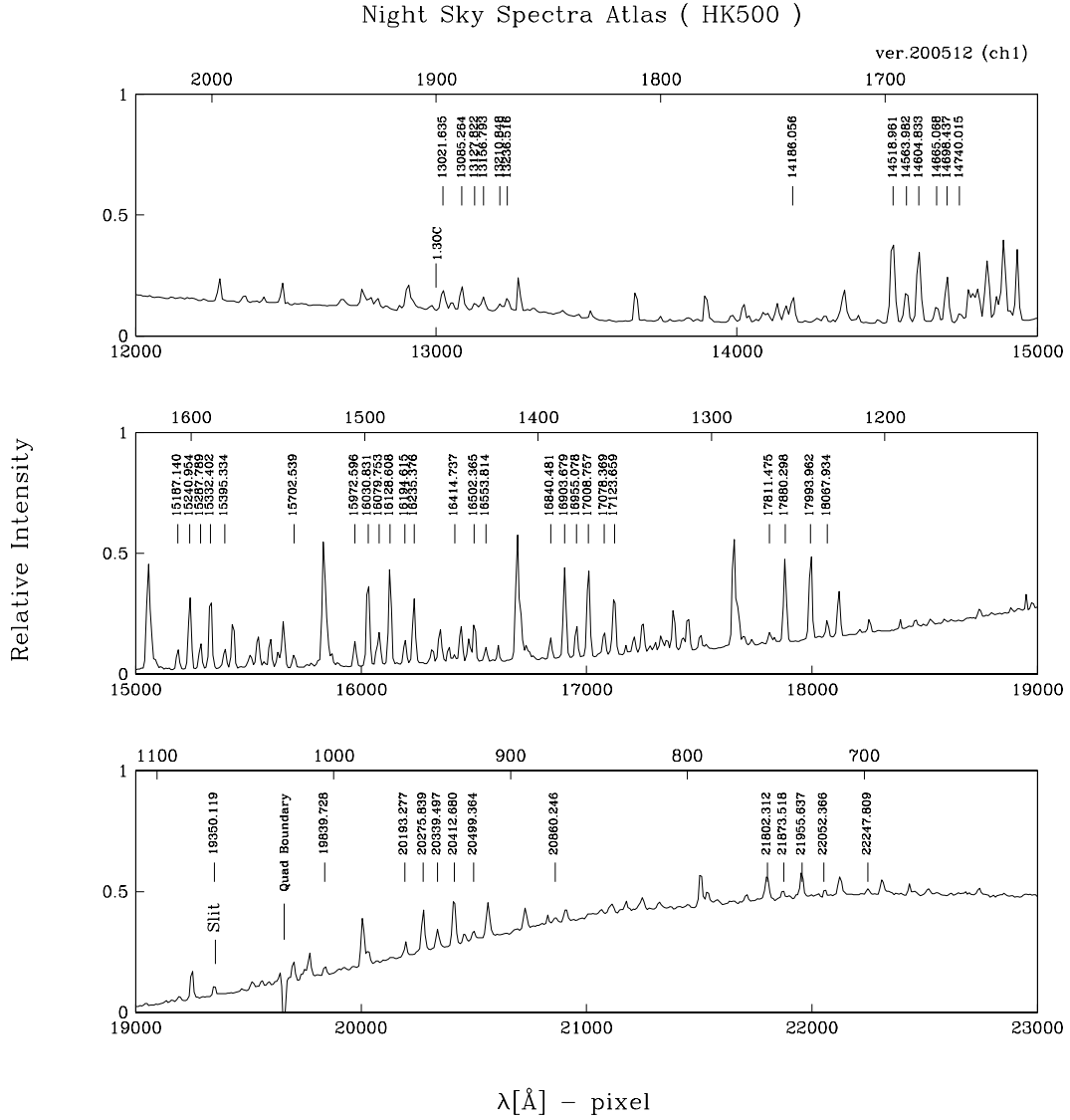


Figure 4.7: OH Night-sky spectra for *HK*-band. The slit is at 20074 Å (1067 pixel). The *HK*-band spectroscopy was obtained with the 1.3  $\mu\text{m}$  order-cut filters and 0.3'' slit. The significant stray light is not shown in *HK*-band wavelength.

### 4.2.2 Efficiency

In order to measure the spectroscopic efficiency of the MOIRCS, we did spectroscopic observation of a A1V star with known magnitude, M112215 (J=8.818mag, H=8.806mag, K=8.745mag), on August 11, 2005. The zJ500 and HK500 grisms are used with 2''0 slit. Since the typical stellar image size during the observations was 0''3, almost all of the flux from the star is expected to fall in the slit. The data are taken at airmass between 1.1 and 1.2. No filter was used for the zJ500 grisms, and 1.3  $\mu\text{m}$  order-cut filter was used for the HK500 grism. The total integration time was 30 sec for each grism.

The spectral images were flat-fielded with a normalized dome flat spectra, which have average of 1 at each wavelength. One dimensional spectral data were extracted from the flat-fielded data. The observed spectra are converted into photon flux (photons/s/ $\text{\AA}$ ) considering the gain of the detector ( $2.44 e \text{ ADU}^{-1}$ ), the integration time, and the spectral dispersion. The resulting observed spectra are shown in the middle panels of Figure 4.8 and 4.9.

The observed spectral data are compared with a model spectrum of A1V star. The model spectrum was made with SPECTRUM code (R.O. Gray). The model spectrum is converted to photon flux with the aperture of the Subaru telescope and the magnitude of the observed star. The spectral resolution of the model spectrum is adjusted to reproduce the observed resolution of the Hydrogen absorption lines. The resulting model spectrum is shown in the middle panels of Figure 4.8 and 4.9 with "model". After that, atmospheric transmission and the reflective efficiency of the telescope mirror coatings are applied to the model spectrum. The efficiency of the instrument was determined dividing the observed spectrum with the model spectrum.

The resulting efficiencies are shown in the upper panels of Figure 4.8 and 4.9 with solid curves. The efficiency include the MOIRCS optics, the grisms, and the detector. The dashed lines indicate expected efficiencies estimated by multiplying the efficiency measured in the imaging observation with the grism efficiency. The observed efficiencies are higher than those expected from the imaging observations. These efficiency was measured with the detector 1 (ch1). Note that a nature of the detector 1 was not so good, and the detector 1 was replaced another detector on December 2005.

### 4.2.3 Flat field images

For the spectroscopic data, there are two types of flat light sources are available, one is a traditional dome flat lamp illuminating a dome flat sheet attached to the ceiling of the dome and the other is a slit illumination halogen lamp which is just above the slit and illuminate the slit through a flat mirror.

It should be noted that the illuminated area of the halogen lamp is limited, thus we need to sweep the lamp over the F.O.V. of MOIRCS. The images of the halogen lamp crossing the F.O.V. with increments of 25 mm is shown in Figure 4.10. It took about seven minutes for one sweep sequence.

We have also tested the flat images taken with a dome flat lamp. The spectra image of the halogen lamp and the dome flat are shown in Figure 4.11 and 4.12 respectively. The absorption feature was dominant in the dome flat spectra and they are not suitable for the flat image.

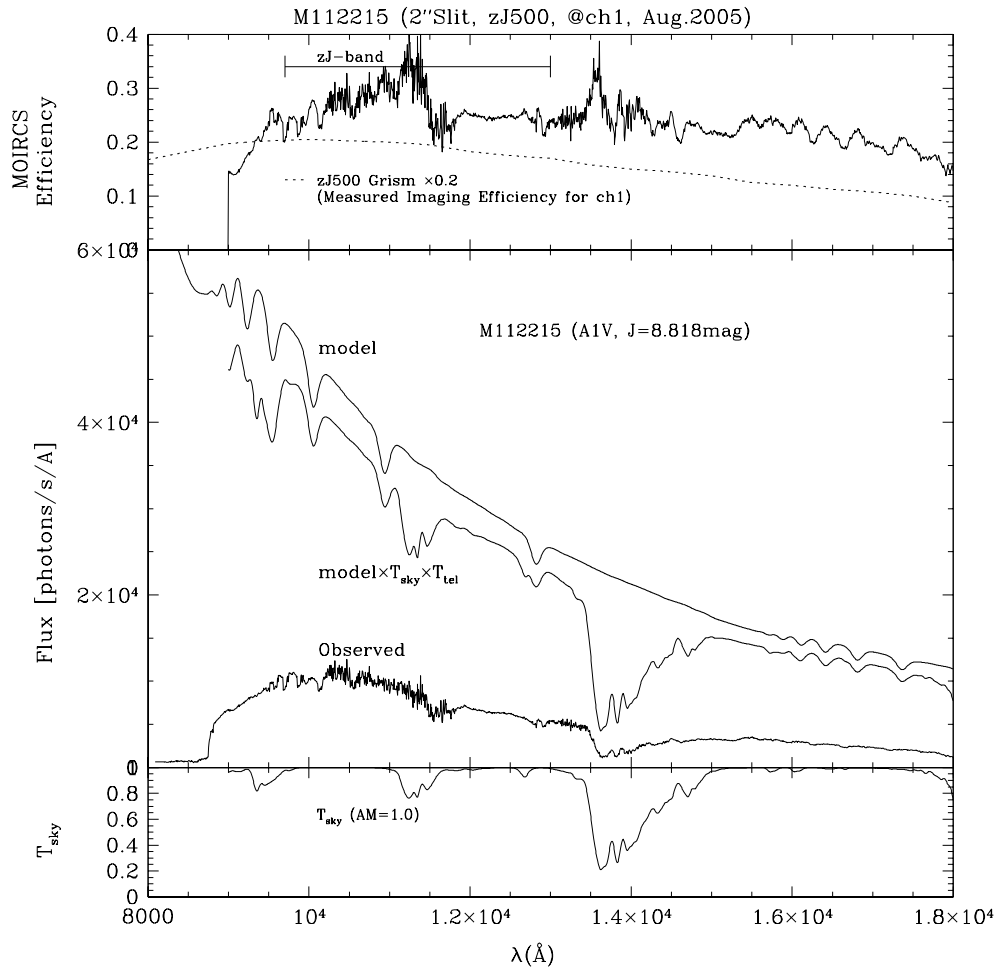


Figure 4.8: Spectroscopic Efficiency with zJ500 grism. The solid line in the upper panel is the resulting efficiencies.

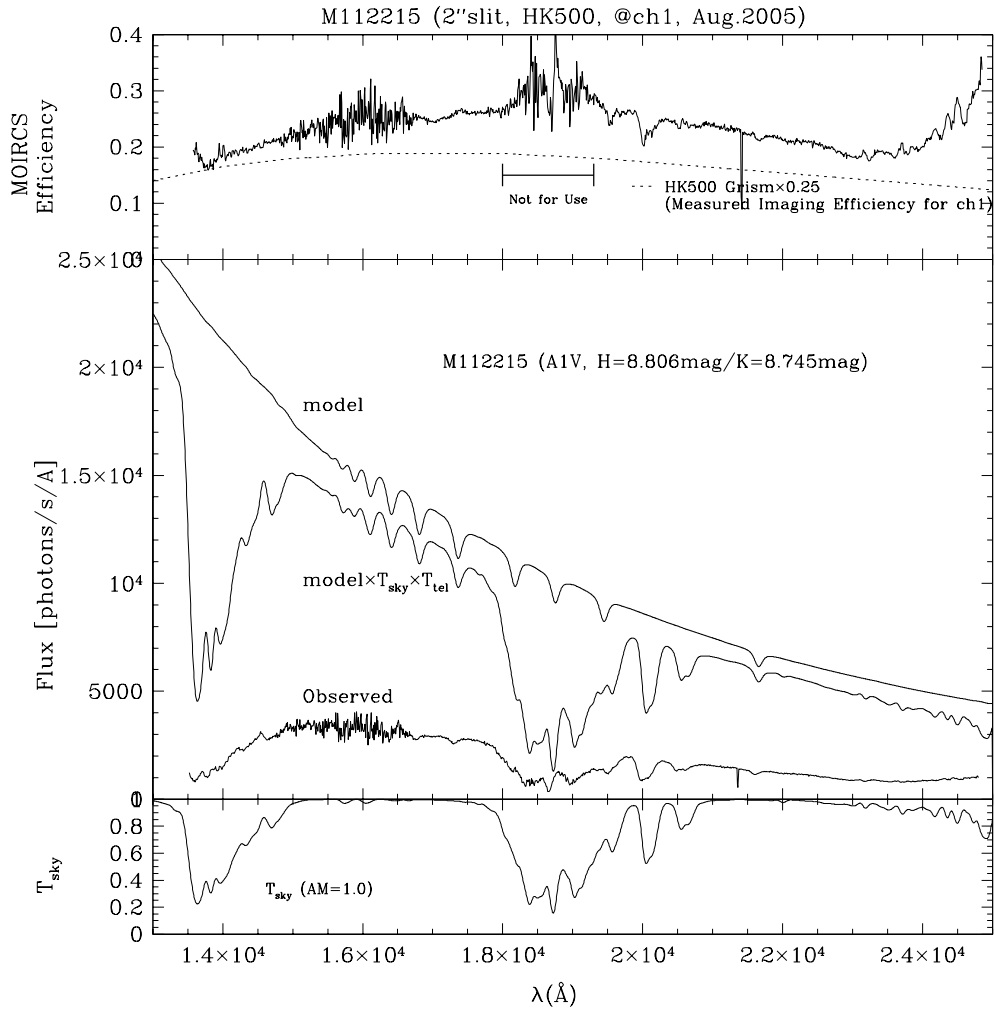


Figure 4.9: Spectroscopic Efficiency with HK500 grism. The solid line in the upper panel is the resulting efficiencies.

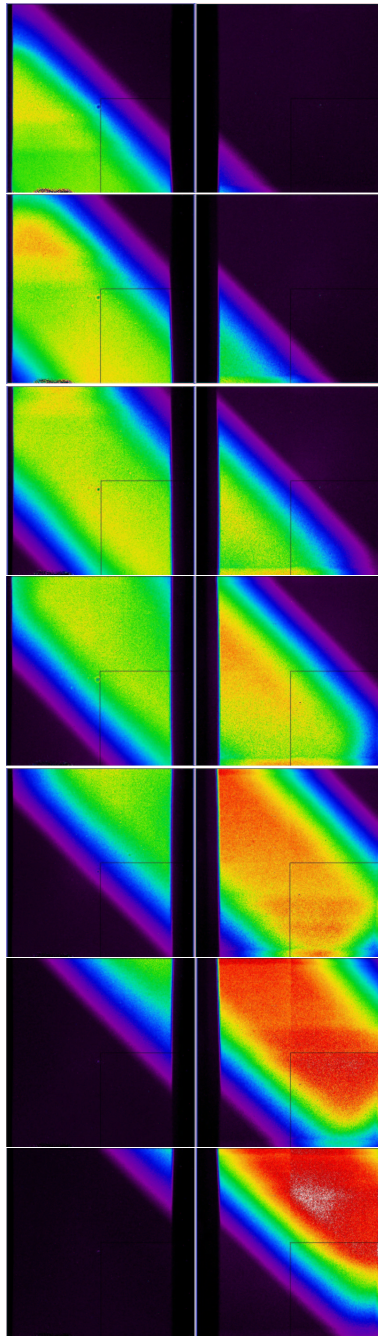


Figure 4.10: The halogen lamp image taken with a increments of 25 mm.

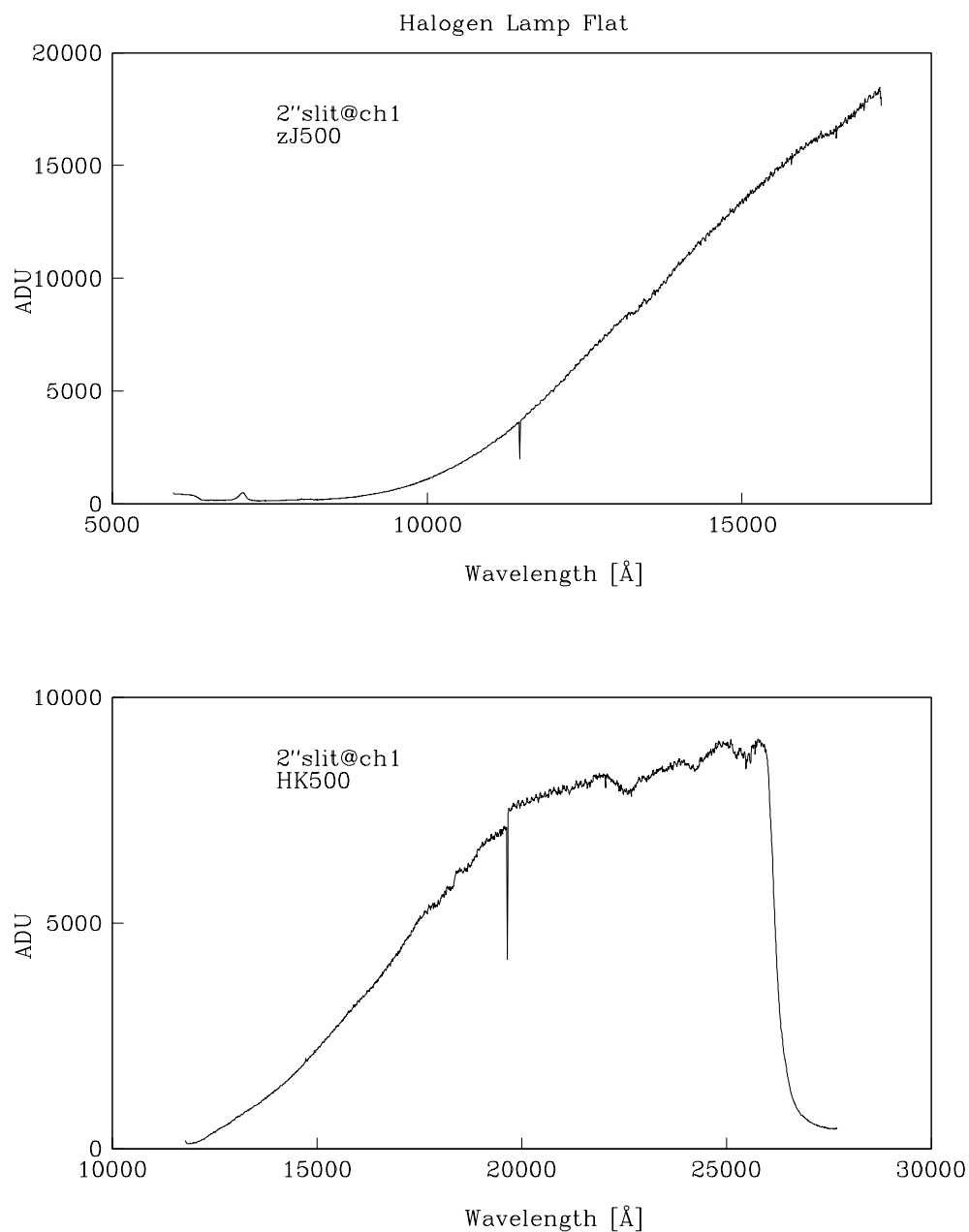


Figure 4.11: Spectral flat image by the halogen lamp.

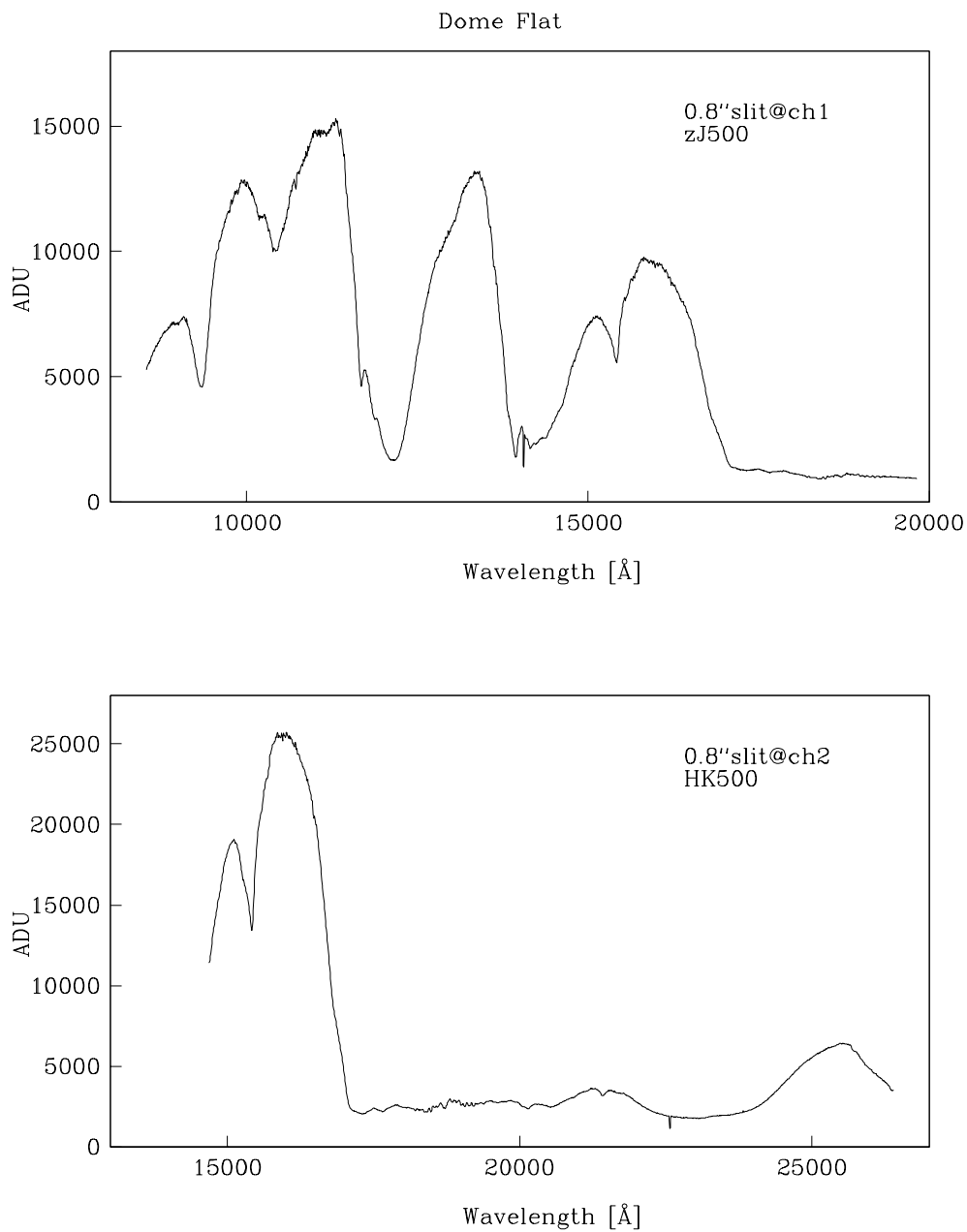


Figure 4.12: Spectral flat image by the dome flat.

#### 4.2.4 Flexure of the Instrument and Effect on Long Integration

After a long integration, due to the flexure of the instrument, the relative position between the telescope and the mask, and between the mask and the detector can be changed. Target objects can be lost from the slit due to the first effect. The position of the spectra on the detector can be shifted because of the second effect.

Flexure tests of the instrument were done in the Cassegrain simulator in Hilo. The shift of detector of maximum  $\pm 2$ pix against the fixed light source is observed. The origin of the flexure is unknown. Details of the flexure test are described in Suzuki (2006).

Such flexure can affect the long integration of the spectroscopic observation. Actually during the engineering observation in the SXDF, the shift of the position were measured (Table 4.2.4). The first column shows the displacement between the guiding holes and star positions at the different airmass. The second column shows the difference of holes of the same mask at the different airmass. The third column shows the difference of the star positions at the different airmass. Since the amount of displacement between the guiding holes and star positions along with airmass are not so small, we need to check the differences once every hour. We take the grism off and take a sky and mask image for the check. If the stars are out of the holes, we need to pull the mask out of the focal plane to perform the pointing sequence.

Table 4.4: Measured flexure of the instrument. Data were obtained during SXDF observations on Dec. 11, 2005.

secz	Hole - Star			Hole - Hole			Star - Star		
	rot	x	y	rot	x	y	rot	x	y
	degree	arcsec	arcsec	degree	arcsec	arcsec	degree	arcsec	arcsec
1.10	0.0039	-0.065	-0.042	-	-	-	-	-	-
1.21	-0.0185	-0.011	0.198	-0.0129	0.010	-0.075	-0.0318	0.044	0.124
1.99	-0.0076	0.092	0.732	-0.0081	0.012	-0.132	-0.0318	0.044	0.124

#### 4.2.5 Atmospheric Effect

Because the telescope does not have the atmospheric dispersion corrector (ADC) in the NIR wavelength, the differential atmospheric refraction inside MOIRCS F.O.V. and the atmospheric dispersion can affect the target acquisition. The amount of the atmospheric refraction is calculated using the atmospheric refraction index provided in Roe et al. (2002). For the atmospheric condition parameters, typical Mauna Kea values are assumed: the pressure of 603 millibar, temperature of 5°C, and the partial pressure of water vapor of 1.34 millibar. The atmospheric refraction calculated with these parameters are shown in Table 4.5.

If the acquisition is conducted in a band different from the spectroscopic observation, for example acquisition in the *J*-band and observation in the *K*-band, there can be a shift of targets due to the atmospheric dispersion. The amount of shift of the image in the *H* and *K*-bands against the *J*-band is shown in Table 4.6. The shift is negligible at zenith distance less than 45°, but need to be considered when the MOS acquisition is done at zenith distance as large as 60° in the *J*-band and observed in the *K*-band.

The atmospheric dispersion also affect the observation with long integration time. The auto-guiding of the telescope is done in the 730nm, the atmospheric dispersion between the observing wavelength and the guiding wavelength results in the shift of the target against the MOS mask. The atmospheric dispersion is summarized in Table 4.7. For example, if the MOS acquisition is done at the ZD of 0°, the targets can be shifted 0."19 at the ZD of 30° in the *K*-band. If the observation continues down to ZD of



$60^\circ$ , the amount of the shift reach  $0''.57$ . The effect is differential, thus if the acquisition is done at ZD of  $45^\circ$ , the shift will be  $0''.57 - 0''.33 = 0''.24$  at ZD= $60^\circ$  in the  $K$ -band.

Finally, the atmospheric effect also affect the mask design. In Table 4.8, the differential atmospheric refraction in the MOIRCS F.O.V. ( $7'$ ) is shown. For example, if a pre-image is obtained at ZD= $60^\circ$  and the MOS observation for the field is conducted at ZD= $0^\circ$ , there will be  $0''.28 - 0''.07 = 0''.21$  difference in the distance between the stars at the both edges of the F.O.V. The amounts of the differential atmospheric refraction are almost same in all of the three bands.

Table 4.5: The amount of atmospheric refraction in  $J$ ,  $H$ ,  $K$  bands

ZD	Shift (arcsec)			
	730 nm	1270 nm	1800 nm	2200 nm
0	0.0	0.0	0.0	0.0
30	20.2	20.1	20.0	20.0
45	35.0	34.7	34.7	34.7
60	60.6	60.1	60.0	60.0

Table 4.6: The shift of a image relative to that in the  $J$ -band

ZD	Shift (arcsec)	
	1800 nm	2200 nm
0	0.0	0.0
30	-0.04	-0.05
45	-0.06	-0.08
60	-0.11	-0.14

Table 4.7: The shift of a image relative to that in the  $730nm$

ZD	Shift (arcsec)		
	$J$	$H$	$K$
0	0.00	0.00	0.00
30	-0.15	-0.18	-0.05
45	-0.25	-0.31	-0.33
60	-0.43	-0.54	-0.57

Table 4.8: Amount of differential atmospheric dispersion in the MOIRCS F.O.V.

ZD	Shift (arcsec)		
	$J$	$H$	$K$
0	-0.07	-0.07	-0.07
30	-0.09	-0.09	-0.09
45	-0.14	-0.14	-0.14
60	-0.28	-0.28	-0.28

## Chapter 5

# Spectroscopic Observations of Distant Galaxies

The Data reduction is the same in general as for the single slit infrared spectroscopy. We successfully conducted Multi-Object Slit observations of the faint distant galaxies for the first time.

### 5.1 Target selection and mask design

In order to examine the MOS capability of the MOIRCS for the observation of distant galaxies, we performed long-integration observation of galaxies with known redshifts in the Subaru XMM-Newton Deep Field (SXDF). The target objects were selected from deep  $K$ - and  $J$ -band images obtained with MOIRCS. There are many galaxies with known redshift from spectroscopic survey observations with FOCAS (private communication with Masayuki Akiyama). Basically, the targets are selected from the objects. There are three sub-mm sources detected by the SCUBA (the Submillimeter Common-User Bolometer Array) on the J.C.Maxwell telescope (private communication with Kazuhiro Sekiguchi). The candidates of the counterparts of the sources are also selected as the targets. The selected objects are listed in Table 5.1. The MOIRCS image of the field and the selected objects are shown in Figure 5.1.

Slit width of  $0''.8$  was used. The typical slit length is 15 arcsec, which allow 5 arcsec dithering with at least 5 arcsec night sky region for the both side of the target.

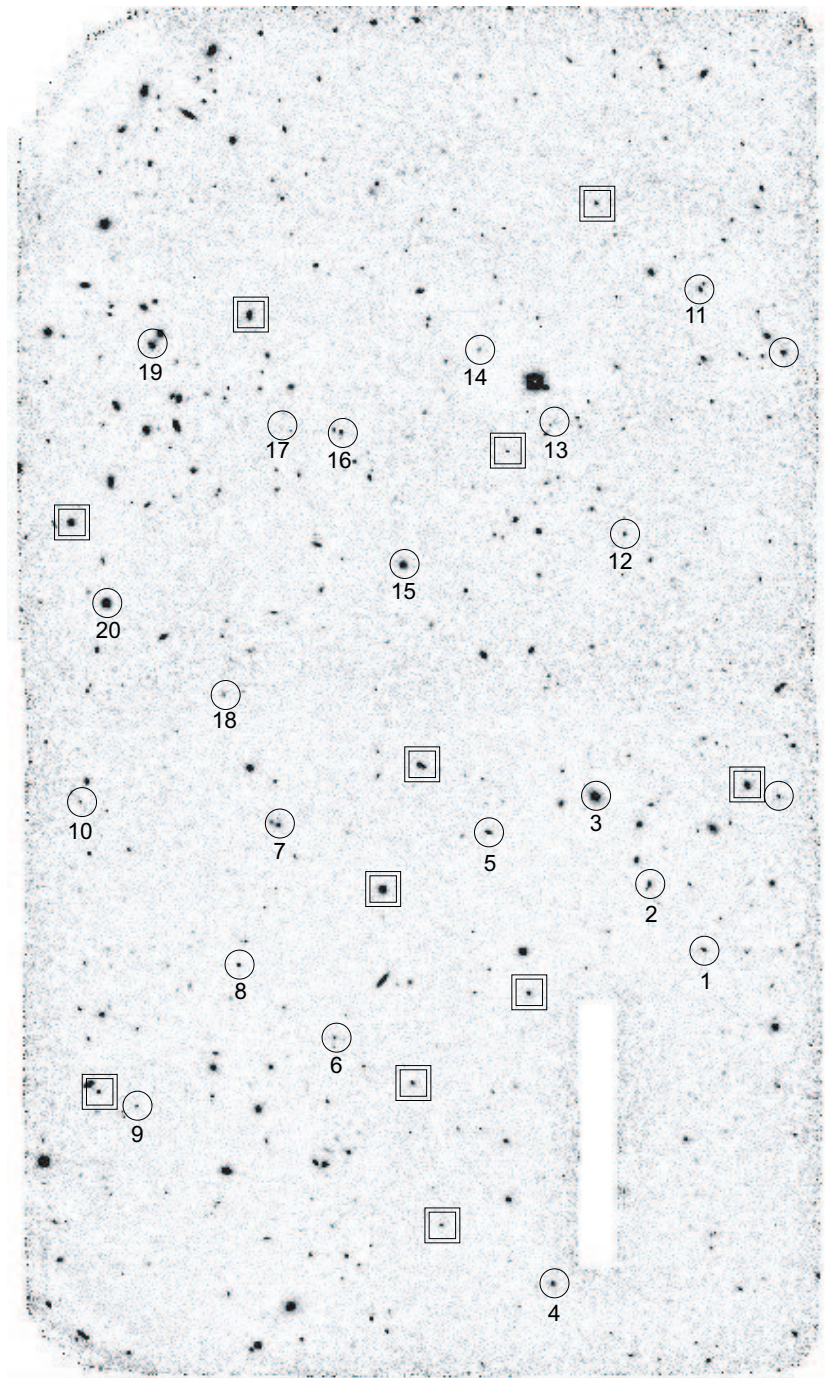


Figure 5.1: SXDF  $K_s$ -band preimage by MOIRCS obtained on Aug. 2005. Exposure was 2400s. The single circle and double squares represent the target objects and the alignment holes respectively.

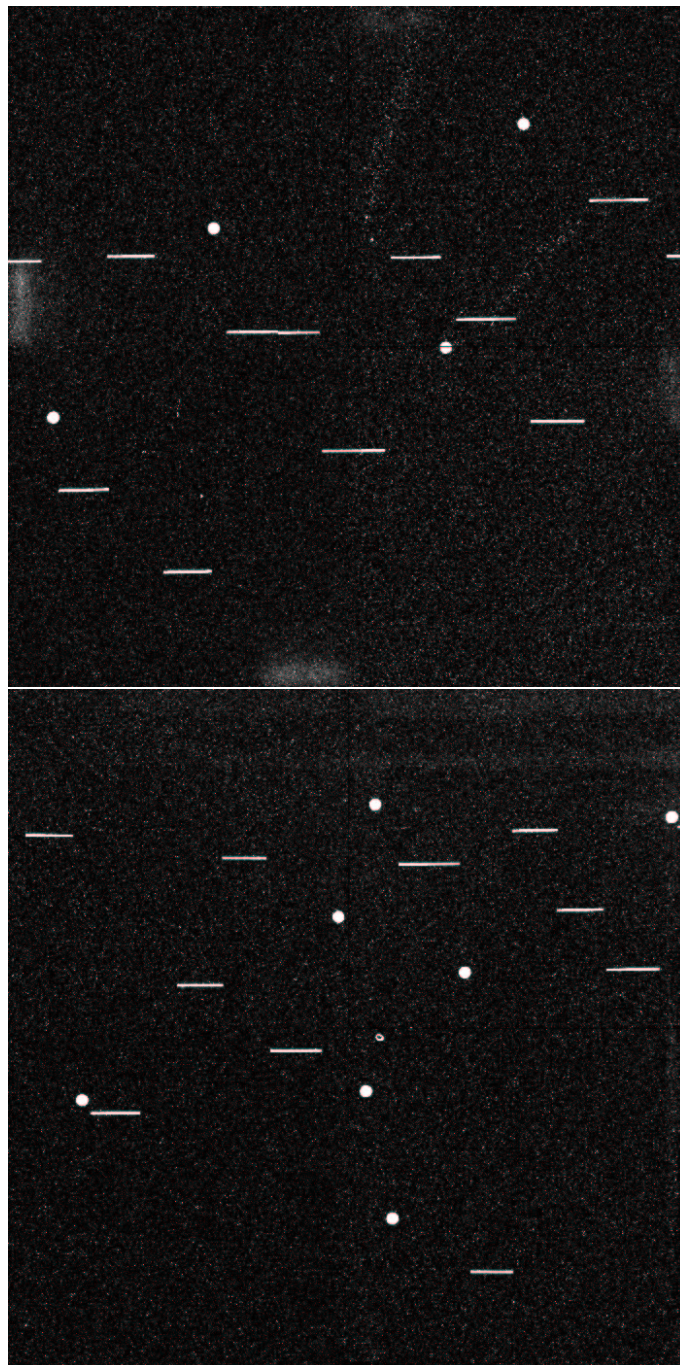


Figure 5.2: MOS mask images for SXDF. Images are displayed with the same direction as Figure5.1. The upper image is detector2 (ch2) and the lower one is detector1 (ch1).

Table 5.1: The object list for the SXDF region. Object 1-10 are onto the detector 1 (ch1) , 11-20 are onto the detector 2 (ch2).

Slit	Name	$z_{opt}$	$mag_K$	$K < 19.5$ $1.8 < J-K < 2.0$	$K > 20$ $2 > J-K$
1		-	18.63		○
2		0.286	18.51		○
3		NID	18.99		
4		0.586	18.01		
5	SCUBA_850.53	-	18.06		
6	SDS0_0065	2.123	19.38		
7		0.800	18.36		
8		0.787	18.98		
9		-	19.91	○	
10		0.857	20.39		
11		1.051	18.09		○
12		2.530	19.01		
13	SCUBA_850.11	-	19.20		
14		-	19.93	○	
15		0.621	17.35		
16		-	18.60	○	
17	SCUBA_850.1	-	18.60		
18		0.858	20.51		
19		0.432	16.96		
20	SDS0_0120	0.553	16.71		

## 5.2 Observation

The spectroscopic observations of the mask are conducted on October 11 and 12, 2005 and December 10 and 11, 2005. The observations were carried out as a part of the engineering observation of the MOIRCS. The number of exposures and integration time are listed in Table 5.2. The total exposures are 2.5 hours and 2.3 hours in zJ500 and HK500 grisms, respectively. The sky was clear during these observations. The typical stellar image size during the observations are 0.6-0.8 arcsec in the  $K_s$  band. We obtained the data with dithering  $5''$ .

Table 5.2: Observation log for SXDS. “OC1.3” filter means  $1.3 \mu\text{m}$  ordercut filter.

Date	Grism	Filter	Exposure
October 11, 2005	zJ500	None	180 s $\times$ 4
			360 s $\times$ 2
October 12, 2005	zJ500	None	540 s $\times$ 2
			180 s $\times$ 2
			360 s $\times$ 4
October 12, 2005	HK500	OC1.3	540 s $\times$ 2
			300 s $\times$ 2
			600 s $\times$ 8
December 10, 2005	zJ500	None	300 s $\times$ 2
			600 s $\times$ 6
December 11, 2005	zJ500	None	600 s $\times$ 4
			300 s $\times$ 2
			600 s $\times$ 8

## 5.3 Data Reduction

The procedure of reduction is shown in Fig 5.5.

### 5.3.1 Spectra Cut-out

At first, distortion correction was done, then a spectrum for each slit was cut out from the distortion corrected data. After that the each spectrum was reduced following the usual manner for single slit NIR spectroscopic data.

### 5.3.2 Sky subtraction

From each set of position A and B combinations, the position B image was subtracted from the position A image. Figure 5.6 shows the resultant image after the subtraction. Most of the night sky emission lines were removed with the subtraction, but there are residuals at the strongest night-sky emission lines.

### 5.3.3 Wavelength Calibration

The wavelength calibration of the spectrum is done with the raw spectrum before the sky subtraction. I used isolated night sky lines referring the night sky atlas shown in Figure 4.6 and 4.7. The curvature of the spectra in the spatial direction due to the camera optics distortion is also corrected in the process. The resulting spectrum has constant dispersion along the x-direction and the wavelength is constant along the y-direction (constant x position).



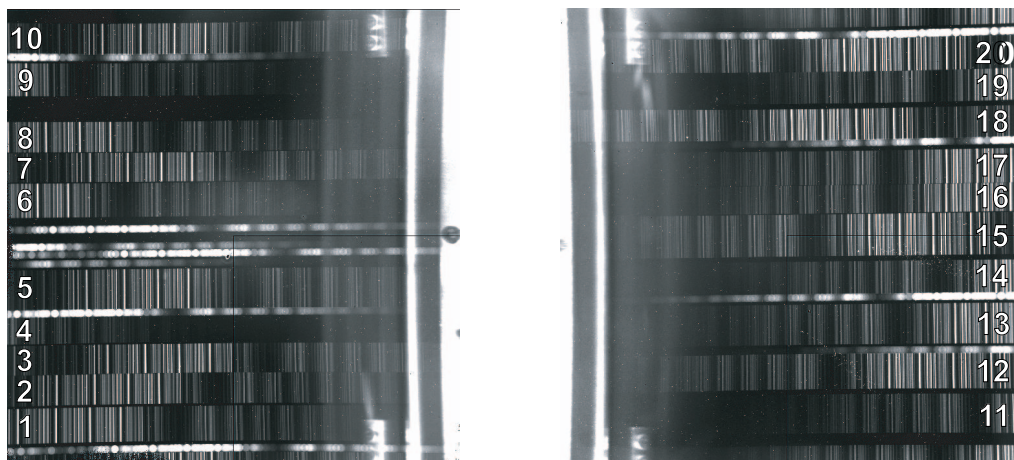


Figure 5.3: Raw data of zJ500 spectra, 600 s exposure.

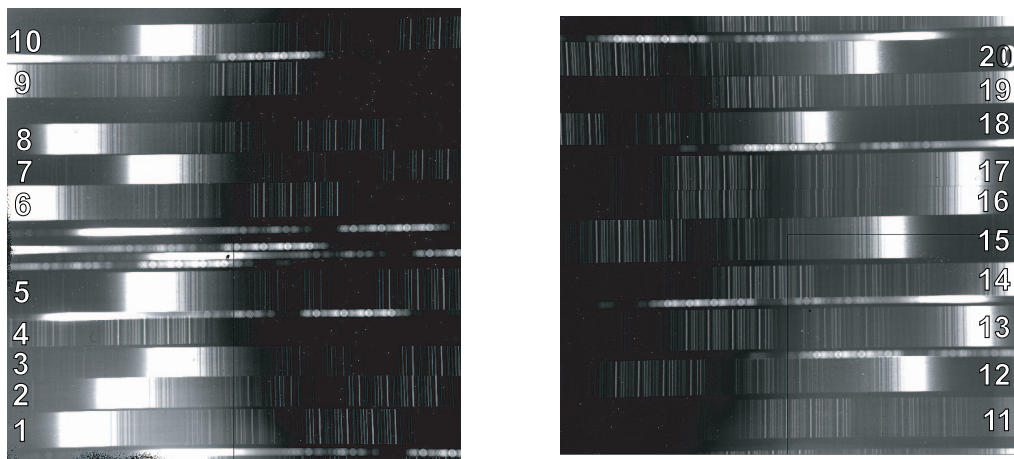
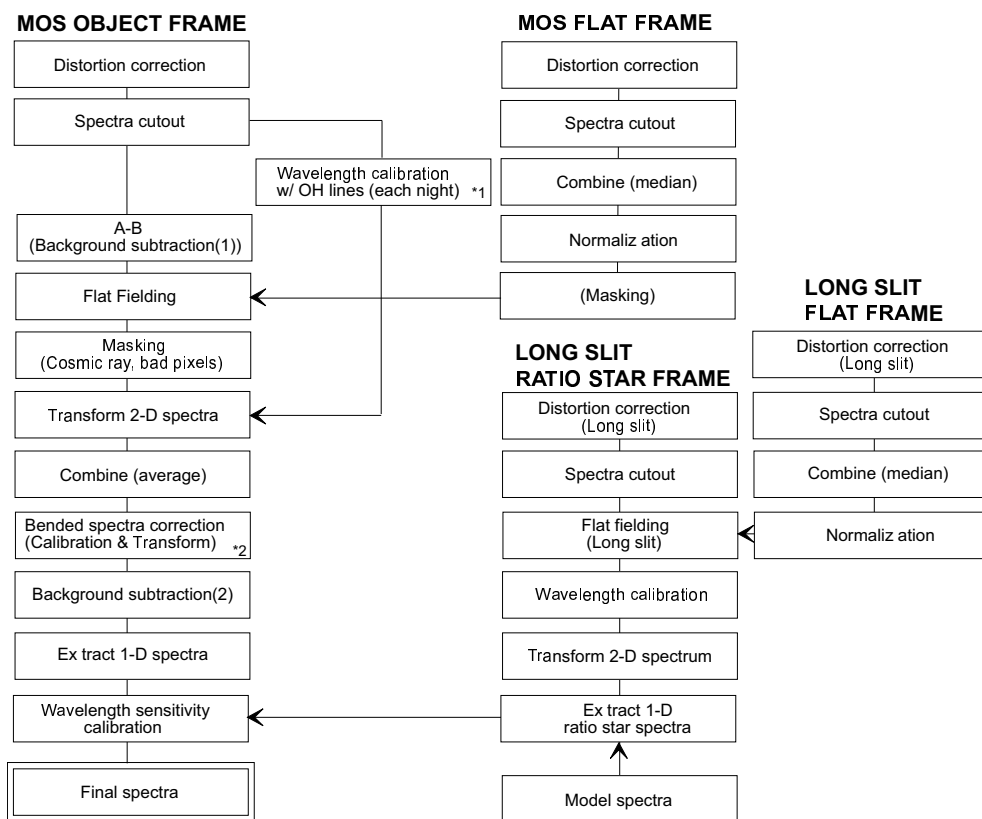


Figure 5.4: Raw data of HK500 spectra, 600 s exposure.





\*1) If object spectrum is not seen on a single A (or B) image, spectrum should be transformed with only wavelength direction.

\*2) Transformed with spatial direction.

Figure 5.5:

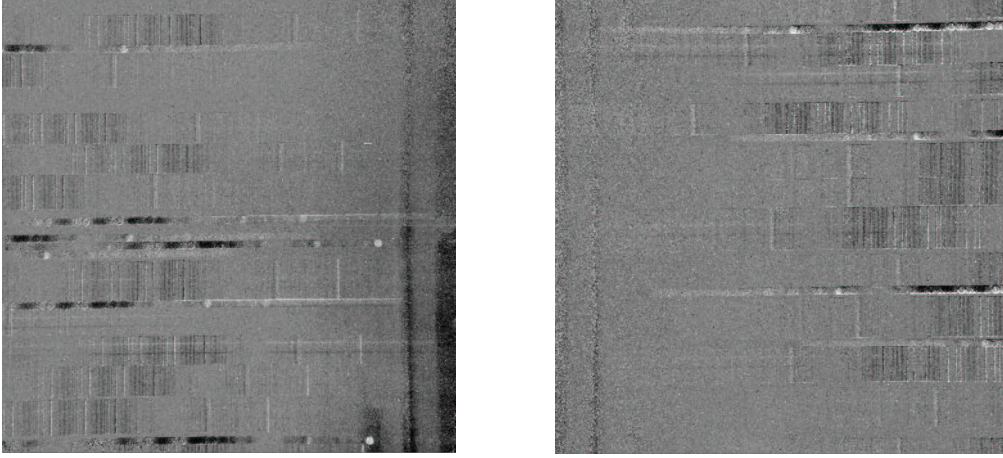


Figure 5.6: Subtracted zJ500 spectra. (MCSA00014965.fits-MCSA00014967.fits.) 60 s exposure. Most of the stray image can be also subtracted.

#### 5.3.4 Flat-fielding

Flat-fielding data were taken with a slit-illumination lamp (halogen lamp). Flat spectra should be also picked-out with the same dimension of the object spectra. After that, all transformed A - B images were flat-fielded with a transformed flat image. At this point, bad pixels and boundary of the detectors must be masked.

#### 5.3.5 Rationing Star

Wavelength sensitivity calibration was done with the long slit spectra of the rationing star (infrared spectroscopic standard stars). The long slit spectrum is used for all the spectra of one MOS field.

### 5.3.6 Results

- **Slit6**  $z=2.123$

For the object in the slit 6, we find four emission lines in  $J$  and  $H$ -band with zJ500 grism, and two emission lines in  $H$  and  $K$ -band with HK500 grism. This object is known to be at  $z=2.123$  and most distant object in this MOS observation. The emission lines, reproduced in Figure 5.7, are identical to [OII]  $\lambda 3237\text{\AA}$  at  $11639\text{\AA}$ , H $\beta$   $4863\text{\AA}$  at  $15187\text{\AA}$ , second [OIII]  $\lambda 5007\text{\AA}$  at  $15637\text{\AA}$ , and H $\alpha$   $6563\text{\AA}$  at  $20496\text{\AA}$ . The vertical lines at both sides of the emission lines are residuals left from the subtraction of strong OH sky lines.

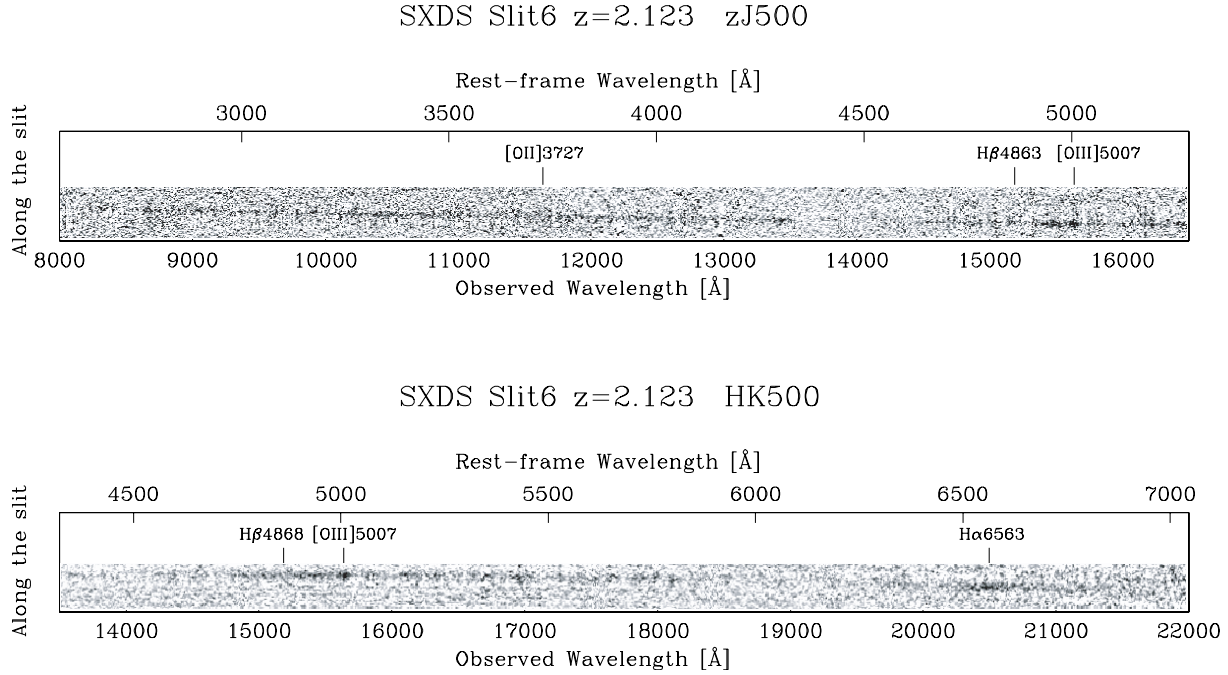


Figure 5.7: 2D spectra of the slit 6. The figure shows the portion of the final, stacked two-dimensional image obtained with an integration time of 2400 s for zJ500 and 2.3 hours for HK500.

- **Slit12**  $z=1.27$

For the object in the slit 12, a strong emission line of  $H\alpha$  is detected at 14867 Å at the edge of  $H$ -band both zJ500 and HK500 spectra. In the zJ500 spectra, a continuum was shown clearly.

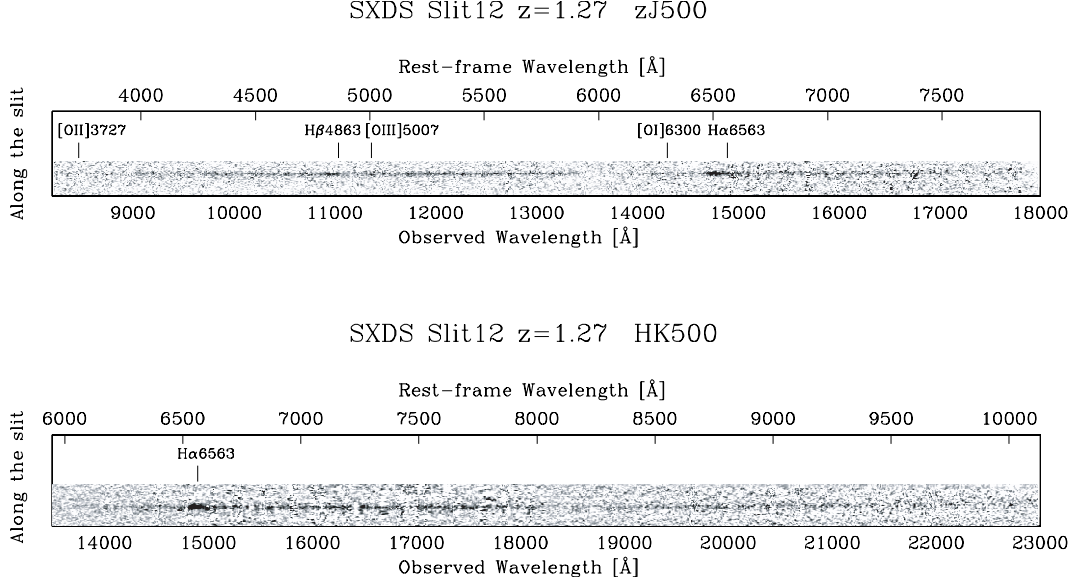


Figure 5.8: 2D spectra of the slit 12. The figure shows the portion of the final, stacked two-dimensional image obtained with an integration time of 2.2 hours for zJ500 and 2.3 hours for HK500.

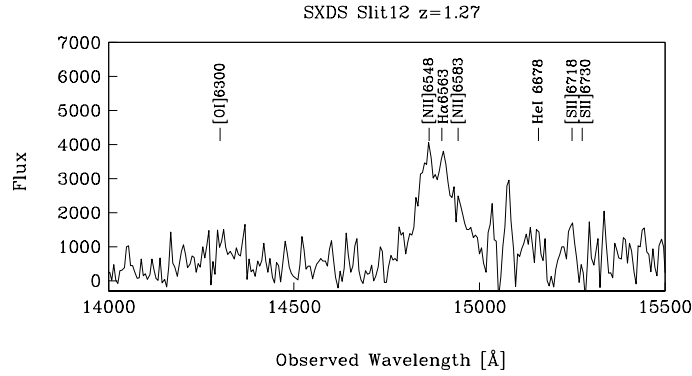


Figure 5.9: Example of MOIRCS  $JH$ -band spectra of SXDS slit 12 shows relative flux of  $H\alpha$  line. The zJ500 grism and 0.''8 slit was used. The exposure time was 2.3 hours.

- **Slit2**  $z=0.826$

For the object in the slit 2, which is spectroscopically-identified at redshift 0.826,  $H\alpha$  emission line is detected at  $J$ -band.

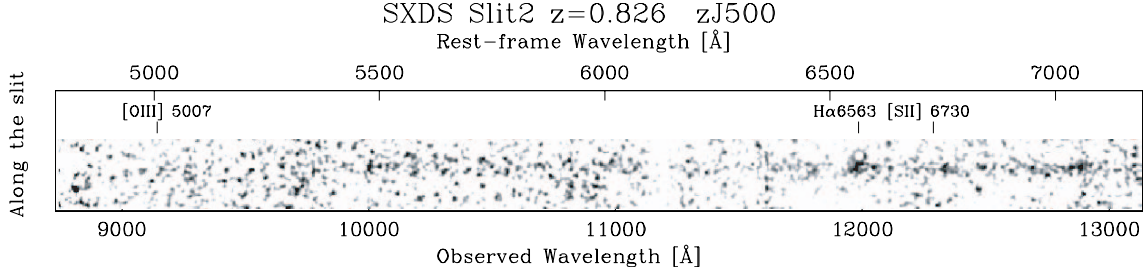


Figure 5.10: 2D spectra of the slit2. The figure shows the portion of the final, stacked two-dimensional image obtained with an integration time of 6600 s for zJ500.

## 5.4 Conclusion

We successfully conducted MOS observations of the faint distant galaxies for the first time with MOIRCS. The result with long integration time indicates that the MOIRCS is capable to detect not only the emission lines but also the continuum for the objects as faint as  $K=19$  mag with integration times of a couple of hours.

# Acknowledgement

I would like to express my special thanks to Prof. Takashi Ichikawa and Prof. Tetsuo Nishimura. They are the supervisors indispensable for my research. I received many invaluable advice and comments from them. I am very happy to meet the opportunity to engage the MOIRCS project.

I would like to greatly thank Mr. Ryuji Suzuki, he is a talented and tough but sometimes schlemiel... anyway he was the best partner to challenge this instrument together.

I would also like to greatly thank all of members of MOIRCS team. Especially, I thank Mr. Koji Omata for his great affair based on his plentiful experiences of engineering. Mr. Masahiro Konishi and Mr. Tomohiro Yoshikawa infused energies into the MOIRCS with their abilities in software. Dr. Ichi Tanaka and Dr. Yuka Katsuno Uchimoto performed quick data reduction and gave much feedback to the team. Mr. Kerry Martin from the Specialized Tool & Machine molded my ideas into the real things. Dr. Toru Yamada has always encouraged me and my research from the viewpoint of science. I would also like to greatly thank Dr. Masayuki Akiyama for his great contribute to the hands-on MOS observations. The research would not be finished without their efforts and encouragements.

I appreciate a great effort and hospitality of members of the Subaru Telescope. The daycrews, the night operators, and the laboratory technicians gave us a generous great help and cheerful smile anytime. Especially I would like to thank Mr. Brian Elms for his great machining work and helping with my drawings. MOIRCS would not perform its firstlight without their long-range support. I also thank Dr. Tetsuharu Fuse and Dr. Cathy Ishida for giving me the many chances to feedback my research to the public.

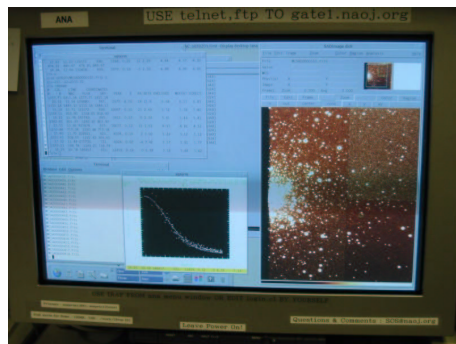
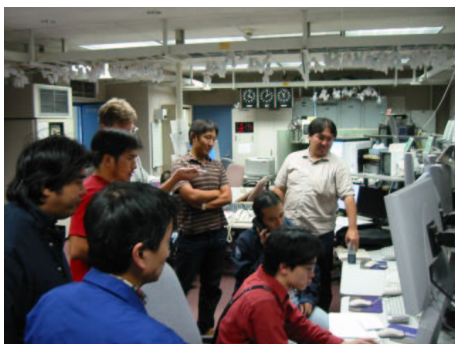
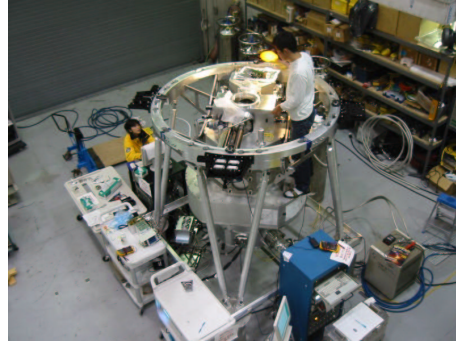
I am greatly indebted to the great experts, Dr. Naoto Kobayashi, Dr. Hiroshi Terada, Dr. Kentaro Motohara, and Dr. Yoichi Ohyama. They gave me uncountable information about the infrared and MOS instrumentation. I also express my special appreciation to the seniors at Tohoku University, especially Mr. Ken'ichiro Asai, Dr. Hiroshi Akitaya, and Dr. Yuji Ikeda, for valuable discussions and their personal friendships. Their sincere stances for astronomy and astronomical engineering had great influences on my research.

I acknowledge the support from the National Astronomical Observatory of Japan for research life in Hawaii.

Finally, I would like to give supreme thanks to my family, grandmothers, and Masayuki for hearty supporting and encouraging my research life.

## ACKNOWLEDGEMENT

82



# Reference

- The Handbook of Cryogenic Engineering, Cryogenic Association of Japan, 1990, Uchida Rokakuho Publishing
- Heat Transfer Textbook, Masahiro S., 1995, University of Tokyo Press
- Erb, D. K., Shapley, A. E., Steidel, C. C., Pettini, M., Adelberger, K. L., Hunt, M. P., Moorwood, A. F. M., Cuby, J. -G., 2003, ApJ, 591, 101
- Erb, Dawn K., Steidel, Charles C., Shapley, Alice E., Pettini, Max, Adelberger, Kurt L., 2004, ApJ, 612, 122
- Kashikawa, N., Aoki, K., Asai, R., Ebizuka, N., Inata, M., Iye, M., Kawabata, K. S., Kosugi, G., Ohyama, Y., Okita, K., Ozawa, T., Saito, Y., Sasaki, T., Sekiguchi, K., Shimizu, Y., Taguchi, H., Takata, T., Yadoumaru, Y., Yoshida1, M., 2002, PASJ, 54, 819
- Astrophysics of Gaseous Nebulae and Active Galactic Nuclei Osterbrock, Donald E., & Ferland, Gary J. 1989,
- Rousselot, P., Lidman, C., Cuby J. G., Moreels, G., Monnet, G., 2000., A & A, 354, 1134
- Pettini, M., Kellogg, M., Steidel, C. C., Dickinson, M., Adelberger, K. L., Giavalisco, M., 1998, ApJ, 508, 539
- Pettini, M., Shapley, A. E., Steidel, C. C., Cuby, J. -G., Dickinson, M., Moorwood, A. F. M., Adelberger, K. L., Giavalisco, M., 2001, ApJ, 554, 981
- Roe, Henry. G., 2002, PASP, 114, 450
- Shapley, Alice E., Erb, Dawn K., Pettini, Max, Steidel, Charles C., Adelberger, Kurt L., 2004, ApJ, 612, 108
- Steidel, C. C., Shapley, A. E., Pettini, M., Adelberger, Kurt L., Erb, D. K., Reddy, N. A., Hunt, M. P., ApJ, 604, 534
- Suzuki, R. Doctoral dissertation (2006)
- Suzuki, R., Tokoku, C., Ichikawa, T., Nishimura, T., 2003, SPIE, 100, 100
- Tokoku, C., Ichikawa, T., Suzuki, T., Asai, K., Katsuno Y., Omata, K., Yamada, T., Tsuda, T., Chiba, T., Sasaki A., Nishimura, T., 2003, SPIE, 4841, 1625
- Yan, L., McCarthy, P. J., Freudling, W., Teplitz, H. I., Malumuth, E. M., Weymann, R. J., Malkan, M. A., 1999, ApJL, 519, L47



# Appendix A

## MLI Fabrication

### A.1 Materials

The materials we used is as follows.

- Kaneka -Thermal control film  
Polyester with aluminized both side ( $t=9\text{ }\mu\text{m}$ )
- Kaneka - Netting Spacer  
Polyester ( $t=200\text{ }\mu\text{m}$ )
- ORCON -AN-90W Reinforced spacecraft film  
Mylar with aluminized one side and reinforced with 100 denier Nome

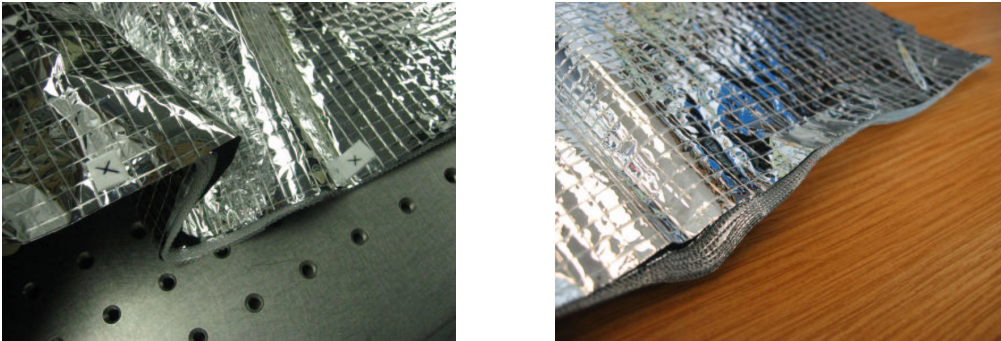


Figure A.1: The enlarged view of the edge of MLI.

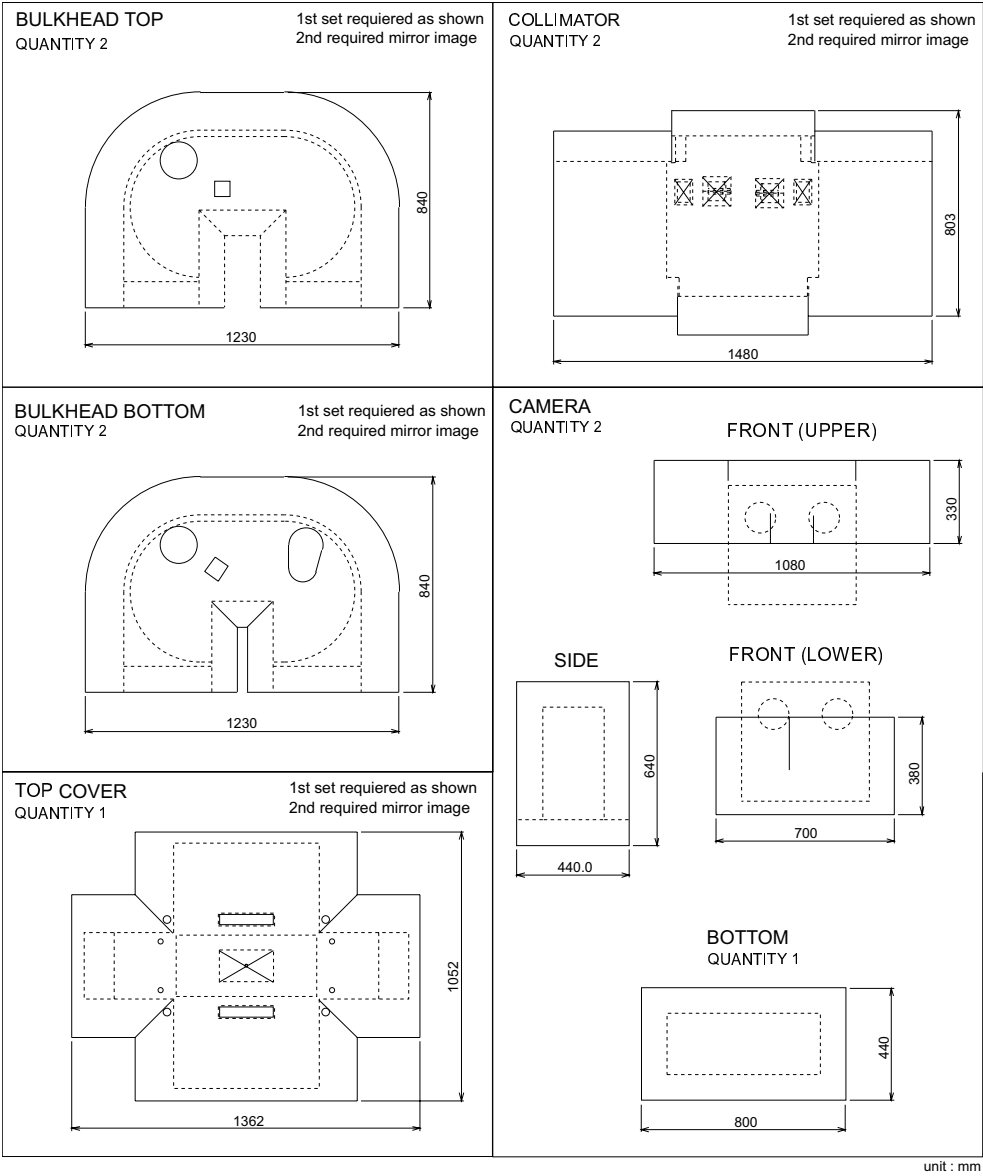


Figure A.2: The pattern for MLI.

## Appendix B

# Liquid Nitrogen

### B.1 Properties of LN<sub>2</sub>

Boiling Point	77.35K @1atm 76.67K @Tucson 73.00K @Mauna Kea
Density of liquid	0.808 kg/L @77K
Specific Heat of liquid	2.042 J/gK @77K
Specific Heat of Vapor	1.072 J/gK @100K 1.046 J/gK @200K 1.041 J/gK @300K
Latent Heat	199.1 kJ/kg 233.8 kJ/kg
Consumption for cooling metal	Use only latent heat Alumium 1.0 L/kg Stainless 0.53 L/kg Cupper 0.46 L/kg Use latent heat Alumium 0.63 L/kg Stainless 0.33 L/kg Cupper 0.28 L/kg
Energy	437 J/kg
	$\text{Log}(P) = 6.49594 - 255.821 / (T - 66.600)$
Thermal Conductivities	Vapor $24 \times 10^{-3}$ W/mK Dolid $7.5 \times 10^{-3}$ W/mK Liquid $139.8 \times 10^{-3}$ W/mK
Cost in Hawaii	2 dollar /L